Controlling Microstructure of Nanocrystalline Thermoelectrics through Powder Processing

by

Samuel A. Humphry-Baker

M.Eng., Materials Science
University of Oxford, 2009

SUBMITTED TO THE DEPARTMENT OF MATERIALS SCIENCE & ENGINEERING
IN PARTIAL FULFILMENT OF THE REQUIREMENT FOR THE DEGREE OF

DOCTOR OF PHILOSOPHY IN MATERIALS SCIENCE AND ENGINEERING
AT THE
MASSACHUSETTS INSTITUTE OF TECHNOLOGY

JUNE 2014

Signature redacted

Signature of Author: _____
Department of Materials Science and Engineering
May 23, 2014

Signature redacted

Certified by: _____
Christopher A. Schuh
Department Head, and Danae and Vasilis Salapatas Professor of Metallurgy
Thesis Supervisor

Signature redacted

Accepted by: _____
Gerbrand Ceder
R.P. Simmons Professor of Materials Science and Engineering
Chairman, Departmental Committee on Graduate Students

Controlling Microstructure of Nanocrystalline Thermoelectrics through Powder Processing

by

Samuel A. Humphry-Baker

Submitted to the Department of Materials Science and Engineering
on May 23, 2014, in partial fulfilment of the requirements
for the degree of Doctor of Philosophy in
Materials Science and Engineering

ABSTRACT

Bismuth Telluride and its solid solutions are currently front running thermoelectric materials because of their high figure of merit. When processed via mechanical alloying to obtain nanocrystalline structures, their efficiency is increased dramatically, due to enhanced phonon scattering at grain boundaries. However, the excess free energy of these interfaces renders them inherently susceptible to grain growth, therefore there is a need for materials with enhanced thermal stability. Despite this, little is known about the relevant processing science of these materials with respect to mechanical alloying and powder consolidation. This shortcoming is addressed here via systematic study of the processing-structure relationships that govern these processing operations. Firstly, during mechanical alloying, the primary mechanism of mixing between elemental constituents is revealed, as well as the limitations to subsequent grain refinement. The resultant behaviour is unique in the literature on mechanical alloying, due to the unusual thermal and thermodynamic properties of the compound and its elements, rendering deformation-induced heating effects especially prevalent. Next, during sintering operations of the powders, the kinetics of grain growth and porosity evolution were studied. By quantifying these processes, a thermal budget map for the nanocrystalline compound is constructed, to allow predictive powder and guidance of both processing and device operation at elevated temperatures. Finally, based on the improved understanding in processing science and thermal stability of these materials, a new class of thermally stable composites is engineered, with improved thermal stability, and hence enhanced thermoelectric properties.

Thesis Supervisor: Christopher A. Schuh

Title: Department Head, Danae and Vasilis Salapatas Professor of Metallurgy

Acknowledgments

First and foremost I would like to thank my advisor Professor Chris Schuh, for his continual guidance, inspiration, and support over the years. In the time I have had the privilege to work with Chris, his mentorship has instilled in me a sense of what it means to do great science, and he will always remain a role model for me.

I would also like to thank the members of my thesis committee, Professor Fitzgerald and Professor Allen, for their time and dedication to this thesis. While I have relished so many interactions with other members of this department, I thank in particular Mike Tarkanian for teaching me how to make real things, and Dr Andreas Wankerl for mentoring me as an innovator.

Thanks to the members of the Schuh group; I am honored to have had the opportunity to work with such a brilliant group of researchers, and people. Special thanks to the members of the unceremonious basement contingent – Zack Cordero, Mike Gibson, Alan Lai and Stian Ueland – for making those Sundays at the lab fun, and for the countless hours of mutual guidance. Thanks also to my brilliant summer students Mark Holdstock and Casey Sanchez.

I gratefully acknowledge financial support of the Solid State Solar Thermal Energy Center (S3TEC) funded by the US Department of Energy. In addition, many members of the S3TEC have given invaluable feedback to this work, and I thank specifically the "TE materials group" for their invaluable contributions.

Finally, I am forever grateful to my friends and family. Thanks to my parents Guy and Hilary, for their constant love and support. Thanks to all my friends, in particular members of the Martha household, for making a special home-from-home, and creating an environment where I look forward to the end of the day. Finally though, I owe most gratitude to Katy for inspiring me to be a better person, and for sticking by me no matter what through our trans-Atlantic separation.

Table of Contents

List of Figures

List of Tables

Chapter 1: Introduction

1.1 Bulk nanostructured thermoelectrics

Thermoelectric materials are able to convert heat into electricity and vice versa. The thermoelectric effect can be exploited in a thermoelectric generator (TEG), which consist of alternate n- and p-type semiconductor thermoelements connected electrically in series [schematised in Fig.1(a)]. These devices can generate electrical power when subjected to a temperature gradient. Conversely when operated in reverse by passing electric current through the thermoelements, the device operates as a refrigerator – also known as a Peltier cooler [Fig.1(b)]. These devices offer reliable, simple, and quiet device alternatives to conventional technologies for cooling and electricity-generation, owing to their lack of moving parts. These advantages have meant they are widely used in space applications, remote service monitoring and temperature measurement [1]. In addition, due to their environmentally benign operation, there has been a great interest to use these materials for waste heat recovery, air conditioning, and solar-thermal energy conversion. However, these applications have been held back due to the relatively inefficient nature of available thermoelectric materials; despite much research in this field, bulk materials performance has advanced little since the 1960s.

Thermoelectric performance can be characterised by a dimensionless figure of merit, ZT, which limits the maximum efficiency of a device:

$$ZT = S^2 T\sigma/\kappa \qquad [1.1]$$

where S, T, σ, and κ are the seebeck coefficient, temperature, electrical conductivity, thermal conductivity respectively. Despite the use of thermoelectric materials in engineering applications for several decades, the maximum ZT of existing bulk scale materials remains at around 1. Therefore existing thermoelectric are limited to an efficiency of about 1/6 the maximum possible Carnot efficiency, which is a factor of 4 or 5 lower than conventional power generation technologies [2].

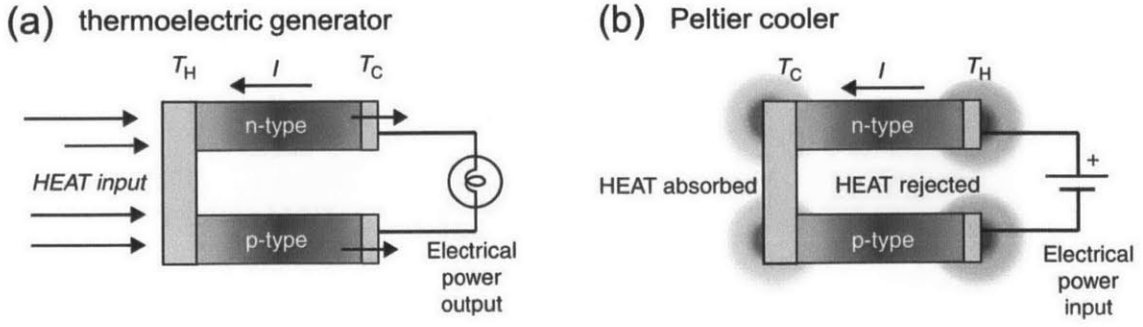

Fig. 1.1 Operating principle of thermoelectric generation and Peltier cooling (adapted from [3]).

Improvements in ZT are made difficult by the inter-relation of transport properties. Due to the coupling of heat and charge flow, increases in σ are usually accompanied by increases in κ, which usually cancels out any overall benefit in Eq. (1.1). The challenge of materials design is therefore to prevent excessive phonon transport, thus reducing κ, without simultaneously disrupting electron transport, thus lowering σ. This idea has been termed in the thermoelectric community: "phonon-glass electron-crystal". One strategy that can address this tension is grain refinement. Grain boundaries are effective phonon scattering sties, but as long as the grain size remains above the electron mean free path, they will not affect σ [4]. A secondary advantage is that grain boundaries are well known to strengthen a material [5], whilst simultaneously offering increased toughness.

Performance enhancement via interfacial control can be achieved in a number of ways, such as: control of crystallographic texture, lamellar structures, embedded nanoinclusions, or interfacial nanocoatings [6]. Severe grain size reduction has attracted much interest due to large demonstrated performance improvements in a number of systems – such as Si-Ge [7] Co-Sb [8], and Bi-Te [9]. Fig. 1.2 shows a recent study of a nanocrystalline Bi_2Te_3 alloy [9], displaying marked improvement in ZT [Fig. 1.2(a)] when compared to a coarse-grained ingot of the same chemistry. The material contained a mixture of nanocrystalline [Fig. 1.2(c)] and macrocrystalline grains [Fig. 1.2(b)].

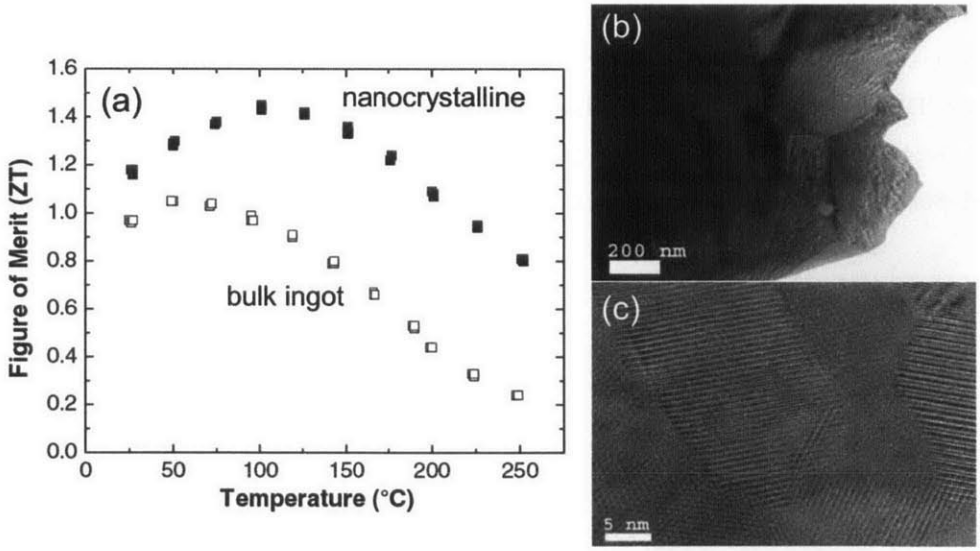

Fig. 1.2 (a) Enhanced ZT for a Bi_2Te_3 alloy after mechanical milling. The grain structure showed a mixture of large grains (b) and nanoscale grains (c) (adapted from [9]).

The use of bulk nanostructured materials presents many processing science challenges. The main obstacle is thermodynamic instability, due to the large driving force for grain growth at fine length scales. This unavoidable coarsening of the microstructure is experienced during consolidation of nc-powders when sintered into bulk pieces. In addition, these materials are exposed to relatively high in-service temperatures – lasting up to tens of years – and hence these extreme temperatures can cause

further degradation of the microstructure and properties. Greater control over the microstructure in bulk nanostructured thermoelectric materials is therefore critical to creating advanced materials with higher ZT. Such control is reliant on basic understanding of microstructural evolution, as well as engineering strategies to improve thermal stability. Despite this, little is currently understood about the processing-structure relationships during mechanical alloying in these materials, how they evolve at elevated temperatures, and methods available to prevent grain growth. In the following section we review the current understanding in the material system of interest – Bi_2Te_3 – as well as the general literature trends in nanocrystalline materials. Based on the major gaps in knowledge identified, we formulate some opportunities for research.

1.2 Bismuth Telluride

Bi_2Te_3 and its solid solutions are state of art thermoelectric materials at low temperatures. Materials with the highest experimentally determined ZT values are shown in Fig. 1.3(a), where Bi_2Te_3 alloys exhibit the highest ZT in the range 0-250°C. Bi_2Te_3 is a congruently melting line compound, with a narrow composition range. The maximum on the liquidus is slightly rich in Bi, meaning that as the compound solidifies from the melt, it will deviate from its nominal stoichiometry to be slightly Te deficient [10]. To accommodate this imbalance, Bi_{Te} antisite defects form, which act as electron acceptors. Density functional theory calculations have shown that these antisites are energetically favored over Te vacancies [11]. Consequently, these materials normally have p-type conduction, whilst doping with Te can lower the carrier concentration.

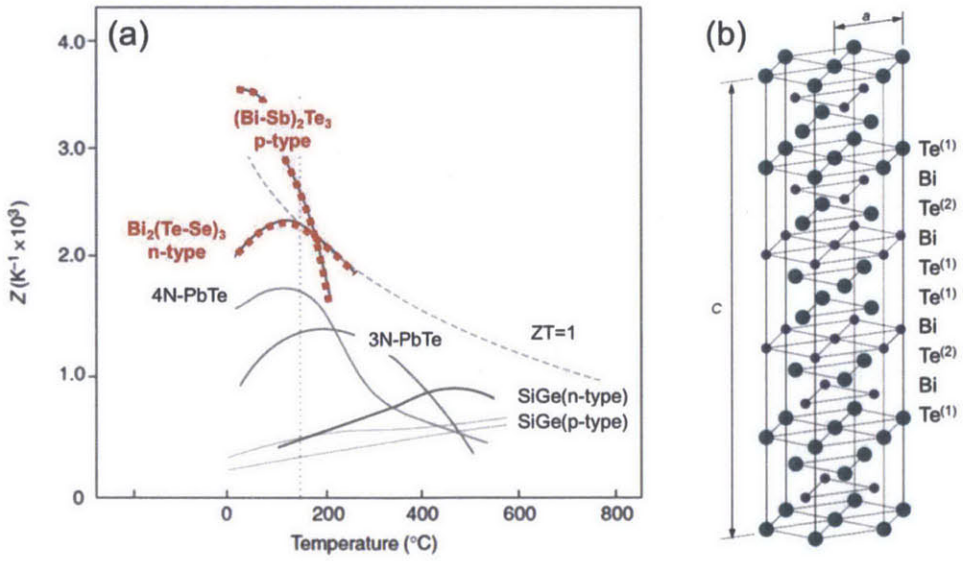

Fig. 1.3 (a) Bi_2Te_3 and its solid solution exhibit the highest ZT at low temperatures (adapted from [3]). (b) Crystal structure of Bi_2Te_3, with repeating pattern of basal plane atoms labeled.

The compound is thermodynamically unstable at high temperatures. Above 700 K, the compound decomposes into a vapour phase, due to the relatively high vapour pressure of Te [12]. The structure has a point group R-3m and a rhombohedral unit cell containing 5 atoms [13]. However, it can be more conveniently visualized using a hexagonal cell with 3 repeating quintets of basal plane atoms [see Fig 1.3(b)]:

$$—Te^{(1)}—Bi—Te^{(2)}—Bi—Te^{(1)}—$$

Layers of covalently bonded atoms are stacked according to this pattern, with relatively weak bonding of Van-der-Waals character between $Te^{(1)}$ layers [14]. Hence Bi_2Te_3 has highly anisotropic properties [15] and will cleave easily perpendicularly to the c-axis.

The ZT of Bi_2Te_3 can be improved by alloying with isomorphous compounds, due to the enhanced point-defect scattering of phonons. State of the art materials are often alloyed with Bismuth Selenide (Bi_2Se_3) or Antimony Telluride (Sb_2Te_3). P-type materials are optimized around $(Sb_2Te_3)_{75}$ $(Bi_2Te_3)_{25}$, and n-type around $(Bi_2Te_3)_{95}$ $(Bi_2Se_3)_5$ [16]. For the remainder of the thesis we focus on the binary compound Bi_2Te_3.

1.3 Nanomaterials via severe plastic deformation

Bulk nanocrystalline materials generally require non-equilibrium processing. As such, energetic processes such as melt spinning, sputtering, and vacuum arc plasma evaporation are often employed [17]. Severe plastic deformation in the form of mechanical alloying (MA) however offers a low cost alternative, as demonstrated by industrial scale manufacture of advanced Ni, Fe, and Al-based materials via mechanical alloying [18].

MA is a powder route process, where material is subjected to repeated cold welding and fracture during collisions between milling tools. At each collision event, since the trapped material is small compared to the tool size, large plastic strains on the order of several hundred percent can be delivered within a collision time of about 10 μs [19], corresponding to extremely high strain rates ($\approx 10^4$-10^5 s^{-1}). The combination of high-deformation rates and low processing temperature permits highly non-equilibrium structures: solid solutions far beyond equilibrium solid solubility limits, grain sizes on the order of 10 nm, and amorphous structures are among the examples. The processing of intermetallic alloys by mechanical alloying and milling has been studied intensively since the development of ODS Ni-based alloys about 50 years ago by Benjamin et al [20]. Around the same time, thermoelectric alloys were being fabricated via ball milling route [21]. However, there is still much unknown about how these materials behave under mechanical alloying and milling. In the following section we describe progress in the field in terms of (i) mechanical alloying of constituent elements to form the compound, and (ii) grain refinement of the single phase.

1.3.1 Mechanical alloying from elements

Mechanical alloying from elemental constituents is of interest because it uses minimal processing steps. By comparison, pre-fabrication of ingots via melting techniques and subsequent mechanical milling requires increased processing time and energy, and is hence more costly. Despite widespread application of mechanical alloying to fabricate nanocrystalline alloys from their elemental constituents, much remains unknown about the mechanisms of chemical mixing. Bi_2Te_3 lies in a relatively unstudied region of the mechanical alloying literature, in that it has a low melting point, a strongly negative heat of formation, and low thermal conductivity. Hence some unusual behaviour could be expected due to thermal effects, although a mechanistic study in this material system has not been performed. This is not the case for conventional metal-metal couples, where mixing is believed to be governed by athermal processes, such as ballistic transport [22,23]. As such, local thermal effects are believed to play only a minor role [24,25]. In highly exothermic systems, thermal effects can play a role such as Self-propagating High-Temperature Synthesis (SHS) [26]. A discussion of the various types of mechanical alloying behaviour is therefore needed.

Mechanical alloying of miscible elements can be classified according to the kinetics of chemical conversion. In the mechanical alloying literature, three distinct kinetic behaviors can be identified. The type of alloying behaviour a particular materials system will display depends mainly on the properties of the parent phases, but also the processing conditions. For example, Fig. 1.4(a) displays a representative collision showing the dominant characteristics of a collision. The impacted material experiences a complex thermo-mechanical treatment during a collision, which is still poorly understood. However a few salient processes seem to dominate – namely intense cold welding and fracturing of particles, highly localized plastic deformation within the particles via shear bands, correspondingly large localized temperature rises, and well as frictional surface forces between powder and milling tools.

The properties of the powder are vital in determining the kinetics of a phase transformation. Thermodynamics of mixing, mechanical properties, and thermal properties can all be influential. Nevertheless, grouping all behaviors into three characteristic kinetic curves is shown in Fig. 1.4(b-d). We discuss each case only briefly here, indicating the material properties that generally account for such behavior in each case.

Sigmoidal (diffusive) transformation

This type pf transformation is typical of metal-metal couples, characterised by a slow and gradual onset of chemical mixing. This mechanism can be described according to three stages: (i) initial formation of a layered composite structure; (ii) refinement of the composite length scale, along with accumulation of deformation-related defects; (ii) gradual intermixing, which is accelerated by increasing density heterophase interfaces and other microstructural defects. These systems are usually

dominated by mechanically aided interdiffusion of elements, and the therefore rate of conversion is chiefly dependent on the size of chemical domains. Hence conversion cannot occur until significant refinement of the microstructure is achieved. In these systems, thermal effects are believed not to play a large role. Examples of this type of system are Ag-Cu and Co-Cu {see Fig. 1.4(b) [27]}.

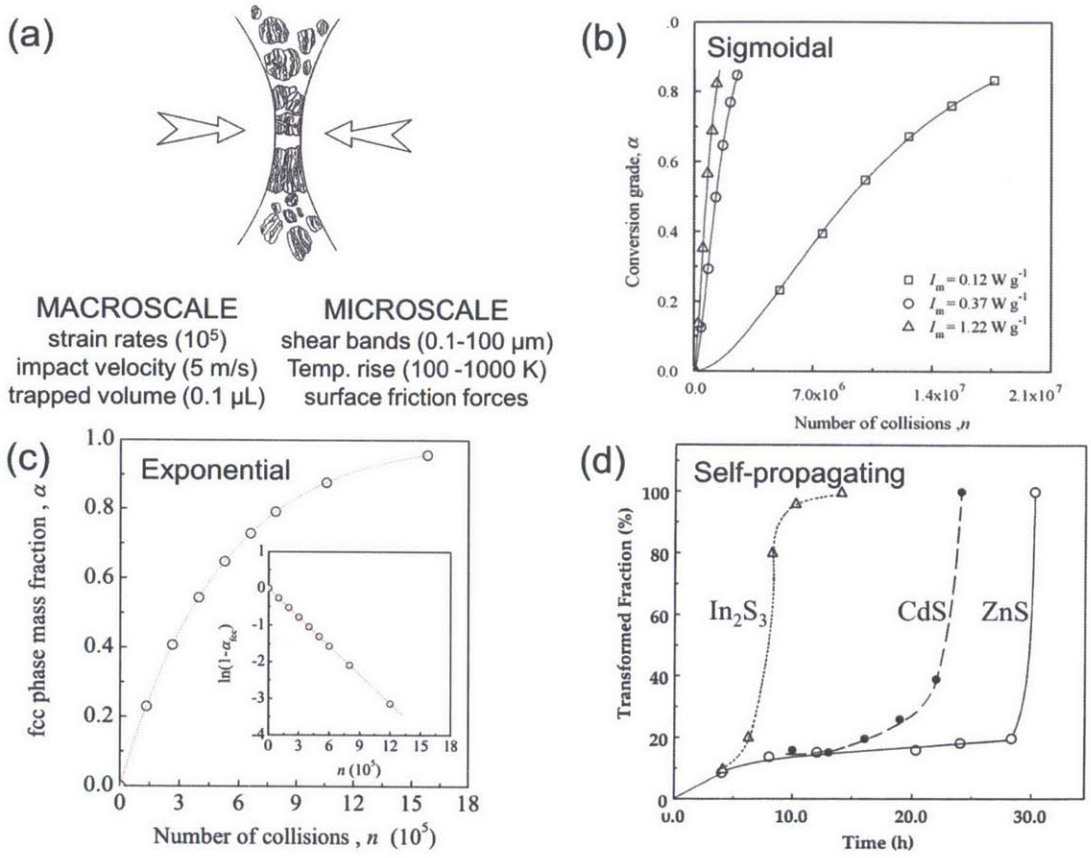

Fig. 1.4(a) Mechanical alloying involves a number of complex processes, operating on different length scales (adapted from [28]). The specifics of the process and can result in different trends for phase conversion: (b) sigmoidal kinetics, as in Ag-Cu [27], or (c) exponential kinetics, as in Co allotropic phase transformation [29], or (d) a self-propagating reaction, as in metal-chalcogens [26].

Exponential (mechanochemical) transformation

This type of transformation is characterised by formation of the product phase mechanochemically and instantaneously at the collision zone. Hence chemical conversion occurs right from the first collision, and the rate decreases monotonically as product is formed and thus no longer contributes. This is different from a sigmoidal transformation, where the rate of transformation is slow at the beginning, and increases, as the microstructure is refined. Examples of this type of system include the amorphization of intermetallic compounds [30], as well as allotropic phase transformations in pure elements – such as Co HCP-FCC {see Fig. 1.4(c) [29]}.

Self-propagating reactions

These transformations are characterised by strongly reactive components that react exothermically during a collision event, subsequently propagating further reaction outside the collision zone. The kinetics of transformation are characterized by a preliminary period of milling, during which the microstructure is refined but little product is formed, followed by an ignition stage where the heat of compound formation drives a self-propagating reaction that consumes the entire powder charge [26]. Metal-metal couples with strongly negative heat of formation [31], some metal-metalloid couples [32], as well as metal-chalcogen couples {see Fig. 1.4(d) [33]}, can exhibit this type of behavior.

The unusually low melting point and thermal conductivity of Bi compared to other metal-chalcogenide systems that have been studied [33] suggests it could display unique alloying behavior. Despite the large number of reports on the synthesis of Bi_2Te_3 via mechanical alloying, none have furnished quantitative or mechanistic understanding. Most studies focus primarily on the measurement of thermoelectric properties of the resultant product [34–40]. The kinetics of structural change during MA in planetary [35] and attrition [36] mills has been studied by X-ray diffraction for the binary Bi_2Te_3 system. Reported alloying times vary from 20 minutes to 8 hours depending on milling conditions. Solid solutions of Bi_2Te_3 and Sb_2Te_3 have also been synthesized [35–37], where the kinetics of alloying are observed to be slower, sometimes requiring up to 60 hours for full homogenization. While these results provide some initial empirical guidelines for the MA production of nanostructured bismuth telluride (n-Bi_2Te_3) compounds, the results are not broadly consistent; this may be because the mechanism of alloying and structural refinement remains unexplored, and without a mechanistic understanding it is difficult to unify the various experimental data points from different studies. A systematic and quantitative study of the phase transformation process is therefore needed. Such a study can facilitate process optimization of thermoelectric materials based on Bi_2Te_3, but more widely inform the field of mechanical alloying in general.

1.3.2 Grain size refinement

Control of grain size and related defects is critical to enhancing thermoelectric performance. Although during the consolidation phase, much grain growth occurs, many deformation-induced defects are still retained, and hence knowledge of processing-structure relationships is important. Despite this, detailed studies of nanostructure formation during milling of tellurides are relatively rare, not usually quantitative, and often not readily comparable with one another [34][9]. The general understanding of deformation-induced defects in Bi_2Te_3 is advancing [41], and may help to understand the conditions that prevail during mechanical milling. Some examples include studies of the atomistic structure of symmetric boundaries [42], the role of deformation-induced point defects in determining the carrier concentration [43], the effect of different levels of deformation on resulting thermoelectric properties

[44], and the energetics of the possible vacancy and antisite defects [11]. What is missing, however, is a quantitative understanding of how these defects evolve during mechanical milling.

The structural evolution of metals and intermetallics in general during mechanical milling has been reviewed by many authors [18,45–48], and Bi_2Te_3 might be nominally expected to follow literature trends. For example, grain size tends to decrease monotonically with milling time towards a steady-state grain size (d_{ss}) [49,50] after prolonged milling, as shown in Fig. 1.5(a). A phenomenological model of grain refinement has been proposed by to occur via three stages: (i) the formation of shear bands or regions of localized high dislocation density, which is supported by TEM evidence on the AlRu system [Fig. 1.5(b)]; (ii) the rearrangement of dislocations within these regions to form subgrains or low-angle grain boundaries; (iii) rotation of subgrain boundaries via further deformation to form high angle grain boundaries. The steady state grain size reached is characteristic of the material [51,52]. This minimum is usually accompanied by saturation in stored enthalpy. Reduction in grain size is – in most but not all cases [50]– concomitant with a monotonic increase in lattice strain [53]. In addition, high point defect concentrations form through non-equilibrium vacancies [54] and antisites [55] in the case of ordered materials. Cumulatively, these defects contribute to a stored enthalpy that can approach 30-40% of the enthalpy of fusion [50]. The microstructural steady state is controlled by the processing parameters, the most influential of which are vial temperature, media velocity, and media size. Lowering milling temperature is a known technique for lowering d_{ss} [56–65] by favoring hardening over defect recovery [51] , as is increasing the milling intensity – either by increasing media velocity or media size [57,65–69].

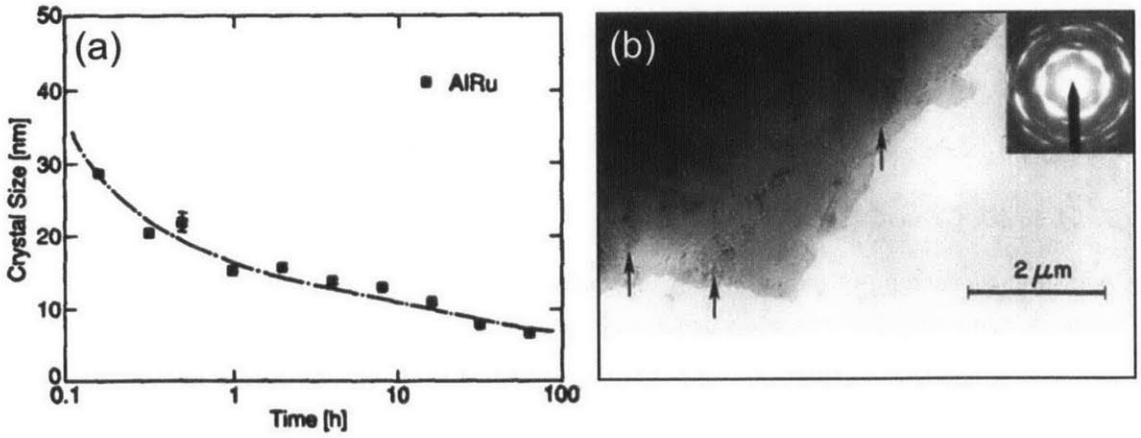

Fig. 1.5(a) In Al-Ru the steady state grain size is reached after several hours of milling [50]. (b) Highly deformed regions of shear banding are observed after 10 minutes of milling.

However, none of the above studies are specific to thermoelectric compounds, or to tellurides in particular, so there remains a need for systematic study in order to understand and control interfaces

and mechanically induced defects in nc-Bi_2Te_3 based materials. Some single data point studies exist in the literature, but these have been inconsistent. Bi_2Te_3 was reported to be milled to a grain size of 10 nm in a planetary mill [40] and 16 nm by different authors under undisclosed conditions [39]. For the ternary alloy $(Sb_2Te_3)_{75}$ $(Bi_2Te_3)_{25}$, the reports from the same laboratory indicate an average grain size of 10 nm from compound ingot [9] and 20 nm from elemental powders [34]. Poor agreement indicates high variability in the structure with process conditions. A detailed study of the processing-structure relationships would be an excellent starting point for establishing best practices for the processing of nanocrystalline Bi_2Te_3.

1.4 Nanocrystalline Thermal stability

Regardless of the production method, single-phase nanocrystalline materials experience unavoidable grain growth during consolidation. Coarsening of the microstructure will reduce the effectiveness of boundary scattering; therefore a quantitative understanding of grain growth in these materials is crucial. In addition to detrimental grain growth, nanoscale phase separation [70], and solid state porosity evolution [71] are known to occur in nanocrystalline telluride compounds. Induced porosities of up to 30% have been recorded in some telluride materials [72]. These processes are generally mitigated during the processing of nanocrystalline thermoelectric materials by the hot-press method [73,74]. This technique combines very rapid heating profiles with compressive stress in order to mitigate detrimental structural evolution; however degradation can still occur during the service life of devices, which must withstand elevated temperatures lasting many years. In the following we section we review the general understanding of the deleterious phenomena of grain growth and foaming, and as a result suggest opportunities for research.

1.4.1 Grain Growth

A firm understanding of the grain growth process is needed in order to design materials resistant to grain growth [75]. As these enhanced materials emerge, grain growth studies can also provide benchmark data for comparison – providing quantitative evidence of stability improvements. Such microstructural understanding can also offer predictive power when designing consolidation strategies that minimise grain growth, such as spark plasma sintering [73], and shock wave consolidation [76]. Once consolidated for thermoelectric generator use, nc-Bi_2Te_3 will be subjected to extreme thermal excursions lasting many years, and therefore the ability to predict microstructural evolution is needed to provide engineering limitations for these devices.

Although growth of coarse-grained materials is reasonably understood [77], in nc-materials new phenomena have been suggested to emerge [78]. As such, thermal stability in nc materials has been

the subject of a number of more recent review articles [75,79,80]. Perhaps the most obvious characteristic of nc-materials is their high specific boundary area, which enhances the driving force for grain growth. Fig. 1.6(a) shows the dramatic increase in grain boundary atoms – corresponding to an increase in free energy – as the grain size approaches nanocrystalline (<100 nm) dimensions. This marked departure from equilibrium can lead to depression in the grain growth onset temperatures – below 0.3 T_m in the case of Fe, Cu, Pd [81] and Ni [82], and even below room temperature for low melting point materials such as Sn, Pb, Al and Mg [81]. Fig 1.6(b) shows the degree of grain growth that has been determined experimentally for some nanocrystalline metals and compounds, with initial grain size typically 10-30 nm. As shown, significant grain growth is exhibited below 0.4 T_m – the typical homologous temperature for grain growth in coarse-grained materials.

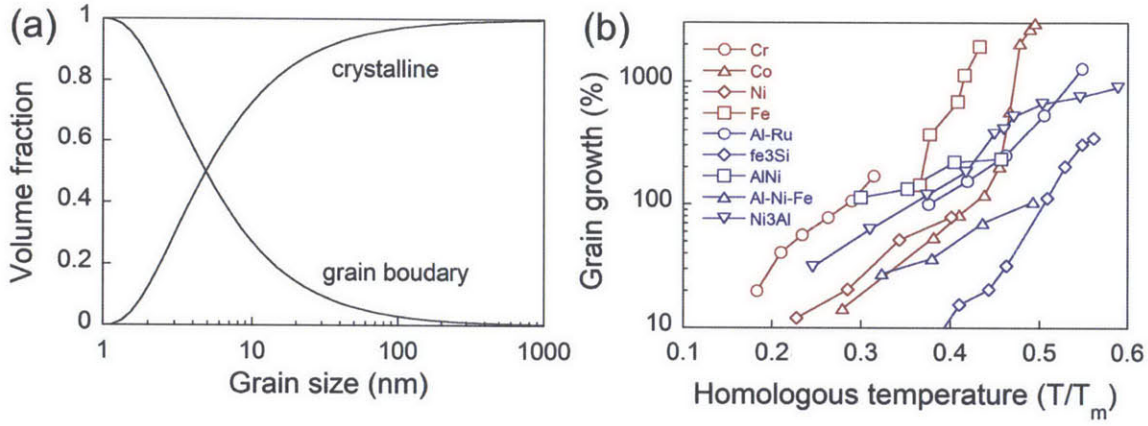

Fig. 1.6 A high driving force for grain growth exists in nanocrystalline materials, due to the large volume fraction of grain boundary atoms (a). As such, grain growth occurs at very low homologous temperatures, as shown in (b) for a number of metals and intermetallic compounds (Data taken from [82–89]).

Despite the increased susceptibility to grain growth, recrystallization in nc-materials is supressed due by the large fraction of stored enthalpy in the grain boundaries. In addition, the rate limiting process of grain growth can change due to abnormally high defect concentrations; such as vacancy supersaturation [90], triple junction drag [91,92], or dislocation drag [93,94]. As a result, the activation energy for grain growth in the nc regime often deviates from that for grain boundary diffusion [82,86,89,95,96], which is the typical rate limiting process for coarse grained-materials [77].

Mechanical milling, a popular method of attaining nanocrystalline grain sizes, introduces further complications. Issues include milling media contamination, porosity, artificially narrow grain-size distributions [78]. Plastic deformation also introduces and highly non-equilibrium grain boundaries, and excess free volume [97]. Relaxation of these high energy boundaries typically occurs prior to grain growth [98–100], sometimes releasing a significant fraction of the total stored enthalpy – e.g. as much as 50% in the case of inert gas condensed Pt [100]. In ordered compounds such as Bi_2Te_3, the picture becomes further convoluted still. Whereas the majority of defect enthalpy is stored in the grain

boundaries for unordered materials, in compounds, anti-site defects can store a comparable contribution. This results in typically greater cumulative stored enthalpy, which is reflected by lower recrystallization temperatures for ordered compounds than disordered ones [101]. Despite generally higher driving forces in these materials, grain growth kinetics are typically hindered due to ordering constraints [102], therefore typically higher onset temperatures for significant coarsening are observed for nc-intermetallics, approaching 0.5 T_m [86,88].

The complex interplay of phenomena highlighted above is expected to be relevant to the specific case of grain growth in nc-Bi_2Te_3 thermoelectric compounds, which speaks to the need for a systematic investigation.

1.4.2 Solid state foaming

As well as being susceptible to grain growth, nanostructured metal-chalcogenides tend to undergo phase separation and spontaneous foaming, after severe plastic deformation. If these processes are controlled precisely – to form a fine array of nanopores and nanoprecitates – in some cases a benefit in ZT is possible [103]. However in most cases significant porosity is deleterious to both thermoelectric [74] and mechanical [104] properties and therefore must be predicted and/or mitigated via detailed understanding of porosity evolution.

Pores are reported to evolve during powder processing of metal-chalcogenide compounds via hot pressing [105,106], or cold press and sinter route [107,108]. Alternatively, pores can evolve after the processing stage during subsequent annealing treatments, for example in flash-evaporated of thin films [109], or hot-pressed compounds [71,72]. What is common in all these preparation methods is a high-degree of microstructural disorder, which induces porosity at elevated temperatures. Porosity will therefore likely be a problem in all compounds synthesised via non-equilibrium methods.

Full density can be achieved by applying high pressures during the consolidation stage [74]. However hot-pressing may not always eliminate the problem; pores can still evolve within these materials when employed in a TEG, due to the relatively high temperatures experienced at the hot-side of the thermoelements, and their long service lifetimes. This can incur unwanted shape change, thus inducing mechanical stresses or even cracking. Additionally, calculation in some materials indicate that porosity will degrade thermoelectric properties from the lowering of electrical conductivity preferentially over the thermal conductivity [110]. Finally, decomposition of the intermetallic leads to precipitation of secondary phases, which will affect thermoelectric performance as compared to a single-phase Bi_2Te_3 structure. Device efficiency therefore, will likely decrease with increasing porosity.

Reports of thermally-induced porosity in telluride-based thermoelectric materials have been presented in both p-type $(Bi\text{-}Sb)_2Te_3$ [107,109], and n-type $Bi_2(Te\text{-}Se)_3$ [108], however still no systematic study of foaming has been performed, and the nature of its formation remains unknown. In order to predict porosity evolution, and mitigate its effects, a detailed study of the foaming process is needed.

1.5 Strategies for improved nanocrystalline thermal stability

As discussed in section 1.3, grain growth presents intrinsic difficulties in processing bulk nanostructures via the powder-processing route, but also in retaining a fine grain size during the lifetime of a thermoelectric device, which must endure extreme operating temperatures. To mitigate grain growth – and thus maximise thermoelectric performance – there exists a need to engineer materials with a stable nanocrystalline grain size. Retardation of grain growth can be achieved by two basic means: (i) reducing the driving force (thermodynamic), in which the grain boundary energy is lowered by chemical additions; or (ii) reducing the boundary mobility (kinetic), where obstacles to boundary motion are engineered into the structure.

Thermodynamic grain growth inhibition is usually achieved by adding a strongly segregating solute atom. As a general rule, the tendency for segregation increases as the matrix solubility decreases [111], but more rigorous models for the segregation enthalpy consider 3 main contributions [112]: the surface energy driving force, the regular solution constant (interatomic interactions), and the elastic energy (size misfit) contribution. The latter always contributes to segregation; however the sign of the two chemical terms can vary. Weissmuller [113] was the first to suggest that a meta-stable nanocrystalline grain size could be obtained, an idea that has been modelled analytically by others [114]. More general analytical models have been developed to predict nanocrystalline stabilization tendency given the thermodynamics of the system in question are known [115]. However experimental reports of grain boundary stabilization for nc-intermetallic compounds are rare. In Fe_3Si, a substitution of 10% Fe atoms with Mn was found to retard grain growth kinetics [116].

Selection of a fortuitously stabilizing solute species in thermoelectric compounds based on Bi_2Te_3 is difficult for 3 reasons: (i) according to the Gibbs adsorption equation [113], nc-materials require high concentrations of solute for stabilization, due to the large amount of grain boundary area; (ii) impurity atoms become charged in the host lattice, in a way not always predictable [117], hence favourable grain size stabilizers will not always impart advantageous transport properties; (iii) while generalized models for the prediction of grain boundary stabilizers are improving for binary alloys [118], in ternary alloys become complicated; hence alloy development will be largely empirical and thus prohibitively time intensive.

Alternatively, kinetic boundary stabilization can be achieved by various paths, such as porosity additions, solute drag, or second phase drag [75]. Solute drag is ruled out from the above discussion,

and as discussed in section 1.3.2 porosity is deleterious to thermoelectric properties, therefore second phase drag is probably the most favourable strategy. The added advantage of second phase particles is that they are well known to provide enhanced creep strength [119]. To provide maximum stability, a second phase particle must be highly thermally stable; therefore inclusions tend to be made of an oxide phase. Fig. 1.7(a) shows some experimental grain size reports in the range 10-500 nm for some metallic materials with oxide nanoinclusions. The Zener limit [120] is shown, alongside the alternative Gladman model [121] for comparison, showing good fit. For example, Fig. 1.7(b) shows the microstructure of a TiAl intermetallic with Y_2O_3 nanoinclusions pinning the grain boundaries, thus retaining a fine grain structure up to 1423 K [122].

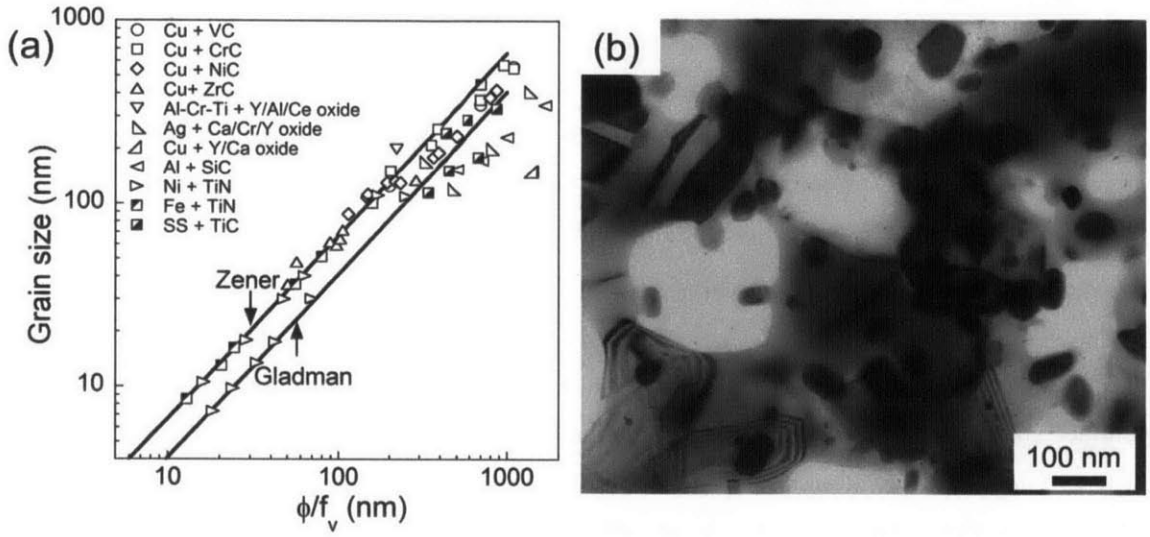

Fig. 1.7 Second phase particles can mitigate grain growth into nanoscale regime according to Zener theory, as shown for in part (a), where grain size decreases with increasing volume fraction:particle size ratio (data from [122–127]). Part (b) shows a dispersion of Y_2O_3 particles in a TiAl matrix [122].

In order to stabilize a fine grain size, the correct inclusion size, shape, volume fraction and chemistry must be selected. Inclusion engineering must therefore be guided by a quantitative understanding of microstructural evolution in thermoelectric materials. Although this strategy has been highly profitable in making fine grained Ni, Fe and Al alloys, it has not yet been explored adequately in thermoelectric alloys. The thermoelectric properties of alloys with second phase additions such as the compound $FeSi_2$ [128] have been studied, however no detailed study of microstructural evolution during heat treatment has been reported in a Bi_2Te_3 alloy or indeed any thermoelectric compound.

1.6 Thesis outline:

The particular deficiencies in understanding outlined above suggest some opportunities for research in nanocrystalline thermoelectric compounds. Clearly a more thorough investigation of microstructural evolution during powder processing operations is needed. An improved understanding of these operations is crucial in guiding processing strategies and the limits to service life, as well as the design of materials with enhanced properties. The fundamental approach of thesis is therefore to tackle this deficiency in three areas: (i) to study the underlying mechanisms and structure property relations governing the mechanical alloying of nanocrystalline tellurides from elemental species; (ii) to study the high temperature consolidation and thermal budget of these materials; and (iii) with the knowledge gained propose strategies for the design of new materials with enhanced thermal stability. The material Bi_2Te_3 is selected as the state of the art compound for low temperature thermoelectric devices. The remainder of the work is split into five chapters:

- In chapter 2, the mechanism of mechanically alloying elemental Bi and Te is explored, which results in abnormally fast alloying behaviour compared to other material systems. The reaction mechanism is explored in detail, revealing a novel mechanical alloying reaction not previously reported in the literature.
- Next, the subsequent grain refinement of the intermetallic is studied in chapter 3. An anomalous trend between milling energy and the steady state grain size is explored, which is analysed via increased heat retention at the impact sites, thus favouring annealing and recovery rather that refinement and defect accumulation.
- The grain growth behavior of nanocrystalline Bi_2Te_3 is presented in chapter 4, revealing two distinct regimes of grain growth; a low temperature region dominated by grain boundary relaxation, and a high temperature region governed by long-range diffusion.
- The solid state foaming reaction in the Bi-Te system is explored in chapter 5. The mechanism of foaming is shown to be driven by decomposition of the compound, which is accelerated by the high diffusivity of the nanocrystalline state.
- Finally in chapter 6, a class of nanocomposite materials with an inert second phase are developed. These materials exhibit stabilized nanocrystalline state to near melting point, with added stability against solid-state foaming. Finally, transport measurements on these composite materials show that the thermoelectric properties of materials employing this strategy can be enhanced.

Chapter 2: Mechanical alloying occurs by a Particle-wise combustion[1]

2.1 Introduction

In chapter 1, we reviewed the literature on mechanical alloying of intermetallics, revealing a gap in the understanding for the Bi_2Te_3. In contrast to many studies on most metal-chalcogenides systems – which mix according to a mechanically induced self-propagating reaction – reports on Bi_2Te_3 tend to indicate a gradual, but rapid, alloying. This anomaly is supported by the fact that Bi lies in a relatively unstudied region of the mechanical alloying literature, in that it has a low melting point, and very low thermal conductivity. A better understanding of the mechanism of chemical conversion would be helpful to unify the understanding of literature reports in the system, but also provide guidelines for the production of these compounds.

It is the goal of this chapter to reveal the primary structure evolution mechanism during the MA of binary Bi_2Te_3. We firstly investigate the kinetics of structural evolution via measurements of the chemical conversion in the global powder charge. Secondly, a technique is developed for measuring both the extent and morphology of chemical conversion on the scale of individual impact collision. We show that during high energy milling of elemental powders, the formation of n-Bi_2Te_3 occurs by a process of particle-wise self-propagating reaction, which is ignited in the presence of liquid Bi. Finally, based on an analysis of the temperature rise at an individual collision, we investigate in what other material systems the presence of molten phase is predicted during mechanical alloying operations.

2.2 Experimental methods

Mechanical alloying

High-energy ball milling experiments were performed beginning with Bi and Te powders of 99.5% purity (from Alpha Aesar, see Appendix A for chemical analysis) and maximum particle diameters of 45 and 75 microns, respectively, weighed according to the stoichiometry Bi_2Te_3. In all experiments the mass of the media was kept to about 50 g and the mass of powders to about 10 g. Mechanical milling was performed with chrome steel balls in a flat-ended hardened steel vial, which was loaded into a SPEX 8000 shaker mill operating inside a high-purity argon atmosphere in a glove box.

[1] The contents of this chapter have been published previously in reference [129]

To compare milling experiments conducted at different times and frequencies, we employ the "specific milling dose", which is a measure of the mechanical energy input to the powder [130,131]:

$$D_m(J/g) = NEt/m_p \quad [2.1]$$

where N, t, and m_p are the milling frequency, the milling time, and the mass of powder respectively. The term E represents the impact energy of a collision, and in general is dependent on the milling vial geometry, dynamics of the milling balls, thermomechanical properties of the materials involved and hence is not known a priori [131]. However for a given experimental configuration the impact energy can be empirically measured [30]. We performed such a measurement using the calorimetric method [130] under different milling frequencies, the details of which are given in Appendix B. The essential result of this analysis is that E is linearly related to N^2 over the range of experimental conditions used. This allows a more functional form for the specific milling dose in terms of experimentally varied parameters, N and t:

$$D_m(J/g) = D_0 N^3 t \quad [2.2]$$

where D_0 is a constant, and was found to be 50 ± 2 $\mu J\text{-}s^2\text{-}g^{-1}$ under the conditions of this study.

Powder characterisation

Samples of powder were characterized by x-ray diffraction (XRD), using a PANalytical X'Pert powder with a Cu Kα radiation source operated at 45 kV and 40 mA. All patterns were collected at a scan rate of 2^o min^{-1} over a scan range of 10-80 degrees 2θ. The patterns were analysed using the Rietveld method, employing a Pseudo Voigt profile function [132], under the assumption of isotropic size and strain. The Bi, Te, and Bi_2Te_3 crystal structures were modelled using literature values for atomic positions [133]. During the Rietveld procedure, pure elemental powder diffraction patterns were first independently refined for in order to obtain the relevant scale factors and lattice parameters. Following this, the mechanically alloyed powders were refined for, allowing the volume fractions of each phase to be determined.

Scanning electron microscopy on as-milled powders was performed using a JEOL 5910 scanning electron microscope (SEM) in backscattered electron mode. Specimens were prepared via cross sectioning and also via direct observation. Powder cross sections were prepared by mounting in epoxy, and grinding with SiC paper 1200-4000 followed by polishing with colloidal silica suspension (0.05μm). For direct impact observation, the milling vial was loaded directly into the SEM without any prior surface preparation. Differential scanning calorimetry was performed on powders using a Mettler Toledo TGA/DSC 1. Samples were heated to 500° C at 5° per minute under flowing argon.

2.3 Global reaction kinetics

Fig. 2.1 shows a series of XRD patterns depicting the structural evolution during the first 30 minutes of milling. The reaction kinetics are rapid, as shown by the disappearance of elemental diffraction peaks after only 15 minutes, or a specific milling dose of around 2kJ/g as estimated from measured ball-vial dynamics in the SPEX mill (see Eq. 2.2). The peaks remaining after this time are all indexed as belonging to Bi_2Te_3.

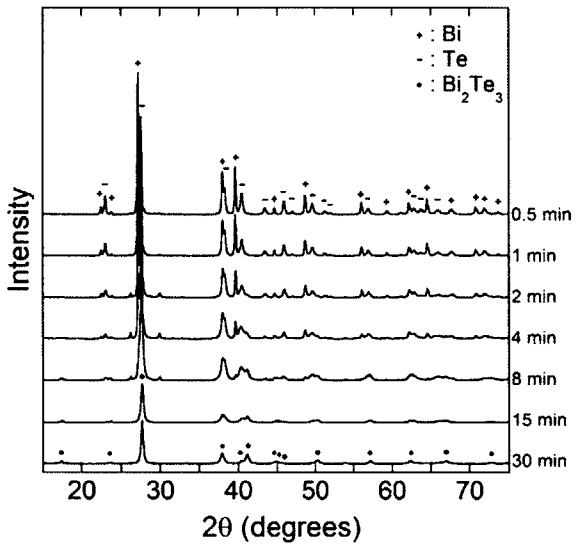

Fig. 2.1 X-ray diffraction patterns of powders taken at different milling intervals. After 15 minutes, all of the elemental diffraction peaks have disappeared, indicating completion of the structural transformation.

For a more quantitative picture, Fig. 2.2 shows a supporting quantitative phase analysis via the Rietveld method, along with stereological measurements on powder cross-sections using SEM. The inset of Fig. 2.2 displays some example micrographs, where Te appears dark, Bi light, and their compound phase grey. Quantitative energy dispersive spectroscopy was used to verify the three phase compositions as 0.98-Te, 0.97-Bi, and intermetallic Bi_2Te_3.

The phase evolution during MA is plotted based upon both XRD and SEM results in Fig 2.2, showing good agreement between the two methods. The results confirm that the reaction occurs gradually, but very rapidly; after only 15 minutes, the powders are single phase Bi_2Te_3. The small mechanical energy input required for transformation suggests that a purely diffusive or refinement-based transformation is unlikely, since such transformations in other alloy systems under similar MA conditions require an order of magnitude more mechanical energy [134]. On the other hand, a single mechanically induced self-propagating reaction [26] to form the intermetallic throughout the whole powder sample, as observed for PbTe [135] and many other metal-chalcogens [33], is also ruled out

by these data, since in this type of process, most of the transformation occurs instantaneously [136], after an initial period of a few seconds [137] to several hours [138] of milling.

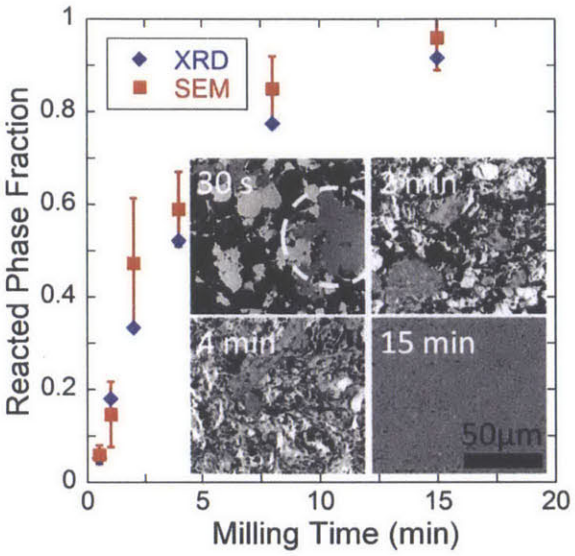

Fig. 2.2 Reacted phase fraction as a function of milling time, calculated using Rietveld phase analysis (XRD) and quantitative metallography (SEM). Agreement between the two methods is good. Inset: SEM back-scattered electron micrographs of powder cross-sections show Bi as white, Te as black, and reacted phase as grey. A fully reacted particle is encircled in one of the micrographs, taken from a powder batch after 30 s of milling.

The powder microstructures during MA give clues to the nature of the structural transformation (Fig. 2.2 inset). After 30 seconds, as expected, we observe mostly an agglomeration of elemental powder particles. However, we also observe large regions, typically 10-100 μm in diameter, which are completely alloyed into the intermetallic compound; an example is circled in the figure. The 6 ± 2 % Bi_2Te_3 measured by SEM in Fig 2.2 is thus not a local reaction product, e.g., formed only at interfaces between Bi and Te, but has fully developed in large, individual powder particles. Note that mechanical intermixing to form such a large region of intermetallic would require refinement of the entire structure to the nanoscale, while the characteristic structural scale is actually much larger at ~13 μm. What is more, at later times the gradual reaction proceeds by accumulating additional large reacted particles, always of the same size or larger than the characteristic structural scale.

The evidence above suggests that combustion reactions have occurred at the scale of individual particles, reacting them fully to form intermetallic Bi_2Te_3. Such a particle-by-particle combustion reaction has been suggested to occur during formation of NiAl [31] and $MoSi_2$ [139], both of which have highly negative heats of mixing. Likewise, exothermic reaction is expected for the present system, which has a negative heat of compound formation of 8 to 16 kJ/mol-at [140,141]; the key to having it occur over only a limited volume is that the heat released is modest relative to that required to inspire further mixing beyond the collision zone.

We performed differential scanning calorimetry measurements (Fig. 2.3) on batches of powders that had been milled for 30 seconds (i.e. microscopically homogenous but only partially reacted) and 15 minutes (fully reacted). Since the intermetallic has a high melting point, the 15 minute-milled sample was thermally stable over the temperature range. However the 30 second-milled sample shows a sharp exothermic peak at 271.5 °C immediately following melting of Bi at 267 °C. This peak can be attributed to a reaction between liquid Bi and solid Te at the Bi-Te interfaces, to produce a solid alloy phase. This observation highlights the reactive nature of the system and indicates that a sudden (explosive) reaction will occur during milling if the melting point of Bi is reached. However, integration of the peak area beneath the melting and compound-formation peaks reveals a net heat release of 2.2 kJ/mol-at, which is far smaller than the 8-16kJ/mol-at for the full reaction. Using the known heat of fusion of Bi as 11.3 kJ/mol-at, this heat release corresponds to a partial reaction in which between 54% (using a value of 8 kJ/mol-at) and 33% (using 16 kJ/mol-at) of the elements are converted into the compound. This experiment therefore also suggests that while some exothermic reaction can occur in these initially partially reacted powders, the heat release is insufficient to propagate it throughout the sample volume.

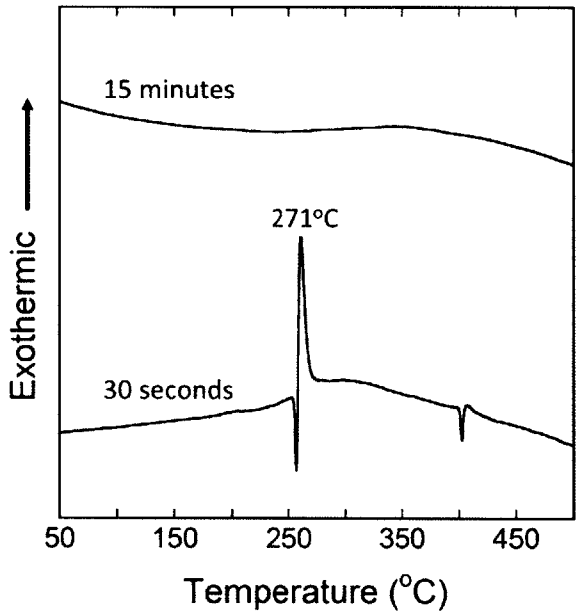

Fig. 2.3 DSC curves for Bi and Te powders that are initially partially reacted (30 s) and fully reacted (15 min). The 30 s sample reacts explosively after melting of Bi, consuming 40% of the powder charge.

To verify the expected reaction heat release during MA further, we performed an MA calorimetry experiment, with a differential aspect in order to permit quantitative differential MA calorimetry. A J-type thermocouple was attached to the milling vial, which was inserted into a low thermal-conductivity jacket made of granulated cork to ensure quasi-adiabatic conditions within. First, a 20 minute MA run was performed to ensure complete alloying (cf. Fig. 2.4, labelled MA). Second,

without unloading the mill, the system was allowed to cool to the same (ambient) starting temperature used in the first run, and a repeat run of 20 minute duration was made (labelled baseline). Again without unloading, a final third run was completed under exactly the same conditions (labelled repeat). Note that for the second and third runs, the powder in the vial was already completely alloyed.

Fig. 2.4 shows the heat signatures from these runs, both of which increase monotonically. The dominant contribution to this monotonic trend is the dissipation of kinetic energy from ball collisions. However, there is a secondary contribution from the heat released upon reaction to form Bi_2Te_3, and this is revealed by the differential heat signature (labelled "MA-baseline"), which is also positive, starts immediately after the milling commences, and is complete after 15 minutes. The differential temperature rise is 1.7± 0.2 ° C, equating to an enthalpy of formation of 12 kJ/mol-at. This value is centred within the range of formation enthalpy values for the Bi+Te → Bi_2Te_3 reaction measured experimentally by conventional calorimetry (i.e., 8 to 16 kJ/mol-at [140,141]). The reproducibility of this result is good; by performing a third run of the reacted powder and calculating the differential with respect to the second (labelled "repeat-baseline") we find a maximum of ± 0.2 ° C attributable to error over a 15 minute milling period. Heat loss measurements show approximately adiabatic conditions, since over 15 minutes the total heat input is 22 kJ and total loss is 2 kJ, i.e. less than 10%. The MA calorimetry experiment thus verifies that the reaction heat is released gradually over the expected duration of 15 minutes, and there are no large spikes of heat release as is seen when the reaction propagates throughout the entire powder [26,31,136–138].

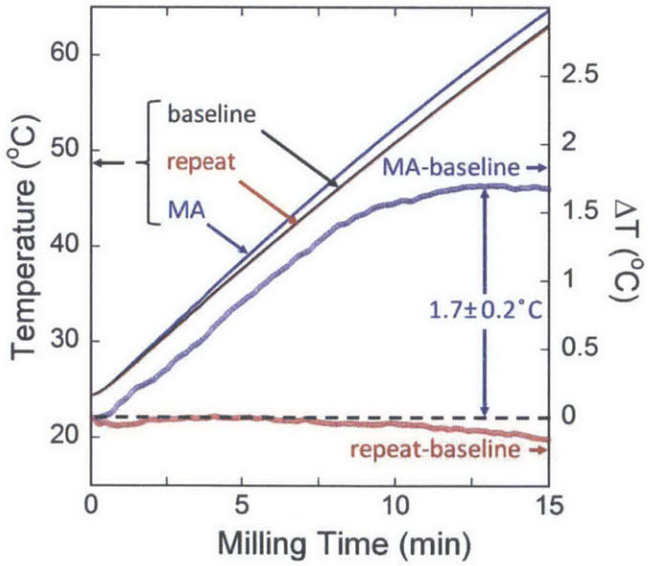

Fig. 2.4 In-situ thermocouple measurements of the milling vial during mechanical alloying (MA) and subsequent milling runs with already-reacted powders (repeat and baseline). A differential signature (MA-baseline) reveals the irreversible heat release from compound formation during MA, whilst there is negligible difference between subsequent runs (repeat-baseline), indicating good reproducibility.

Combining our MA calorimetry experiment with the result from our differential scanning calorimetry work, we infer that during MA, local melting of Bi must occasionally occur [142], triggering a reaction that is limited to local regions. Support for this can be provided by considering the adiabatic milling temperature, T_{ad}, which is the temperature that would be reached if the elemental constituents were to alloy under adiabatic conditions. Considering an upper bound value for the Bi_2Te_3 formation enthalpy of 16 kJ/mol-at [141], T_{ad} must be equal to the melting point of the compound (858 K); only about 12 kJ/mol-at is required to heat the compound to the melting point, and the remaining heat is only about a sixth of the heat of fusion. This value is well below the threshold temperature for self-propagating high temperature reaction at 1800 K [143], which supports the notion that a local ignition would not release enough heat to cause a widespread reaction throughout the powder. However, if there were a small local temperature rise between milling tools for a given instantaneous impact event (which does indeed occur, and has been estimated to be on the order of 400K [144]) it seems quite plausible that a local self-sustaining reaction could be triggered within an individual particle.

2.4 Individual impacts: critically deformed regions

With the above understanding of the global kinetics of mixing, we now investigate the reaction in more detail on the scale of individual impacts. This was achieved by developing an impact test that allowed isolation of a single collision. The impact test was performed inside the SPEX mill to allow direct comparison of chemical conversion on the scale of the total vial with that of individual impacts. Individual powder compacts that had undergone a single collision were analysed after cold welding event to the vial surface. Extensive cold-welding was encouraged by sandblasting the vial prior to each experiment. In addition, a single milling ball of 8 g mass was employed, to prevent ball-ball collisions and thus allow estimation of the impact energy. The mill was operated for approximately 8 seconds, which yielded about 100 collisions at each end of the vial. Fig. 2.5(a) shows the geometry of a representative collision. The resultant cold-welded compact typically had a diameter on the order of 1 mm, and a thickness of 0.1 mm.

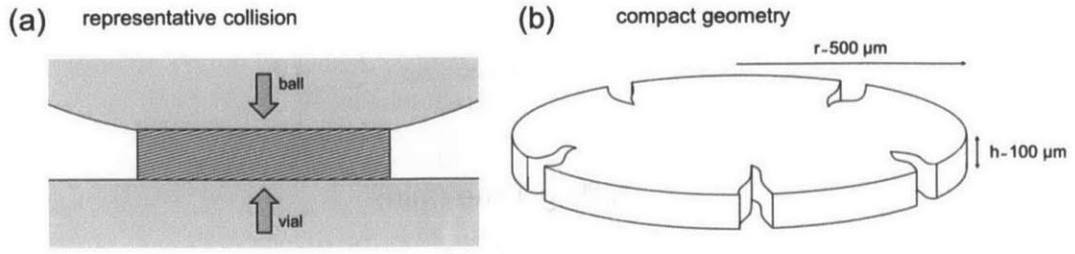

Fig. 2.5 Schematic of the collision impact test, displaying (a) the geometry of a representative collision, along with (b) the resultant cold-welded compact.

Examination of the compact surface was performed via SEM in backscattered imaging mode. As in Fig. 2.2 the intermetallics region appear grey, Bi white, and Te black. Fig. 2.6(a) shows a representative compact, revealing the salient nature of the mechanochemical transformation. Despite receiving a single collision from the milling tools, the powder particles are shown to have reacted on a considerable scale, forming approximately 25% of intermetallic phase. The reaction morphology displays a repeatable pattern, where alloyed regions are localized within streaks originating at the center of the compact and radiating outwards. These critically deformed regions (CDRs) are shown in more detail in Fig. 2.6(b) and (c), which shows an SEM image taken at higher magnification of a single CDR. Part (b) shows the center of the compact, revealing the origin of the CDR. Much like a river is composed of many tributaries, the CDR originates at smaller regions which themselves originate at gaps in Te particles. Part (c) shows the emergence of a CDR region at the edge of the compact, which results in an ejection of liquid Bi away from the compact. The presence of liquid phase is given conclusively by spherical droplets on the surface of the ejected region.

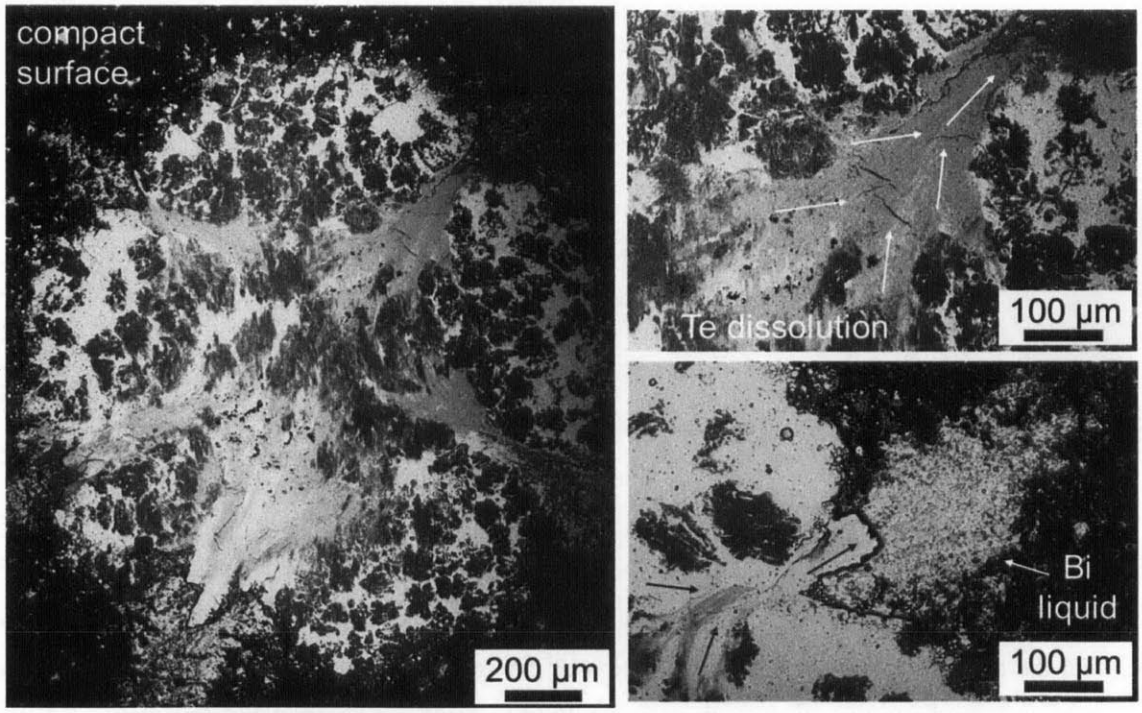

Fig. 2.6 SEM images of a typical impact showing (a) the highly reacted nature of a single collision, along with radial morphology of critically deformed regions, (b) the CDR origin at the compact center, showing tributary formation of intermetallic and (c) the CDR ending at the compact edge, showing ejected liquid Bi.

Based on these observations we propose that molten Bi phase is first formed at the compact center once a critical amount of deformation is reached. The localisation of reacted product can be explained on the basis of adiabatic shear; i.e. if the rate of strength loss due to heating exceeds the gain in strength due to defect production, run away localized deformation will occur, which eventually leads to melting. Such a phenomenon has been observed during deformation of bulk metallic glasses –

where high strain rate deformation conditions can lead to melting of Sn coatings [145]. Once molten Bi is formed, dissolution of Te particles in the molten Bi can occur rapidly, leading to the formation of the compound phase.

To estimate the degree of chemical conversion based on a single impact, a quantitative stereological analysis was performed of a total of 23 cold-welded compacts. For each compact, the area fraction was determined stereologically using the point counting method, via a regular 10x10 array of points. From the total number of intersections, a measure of the compact area was made. Fig. 2.7 shows a cumulative distribution of both the volume fraction of intermetallic phase present, and radius of the compacts. The average compact radius was 0.68 mm, and the average volume fraction of intermetallic was 0.14.

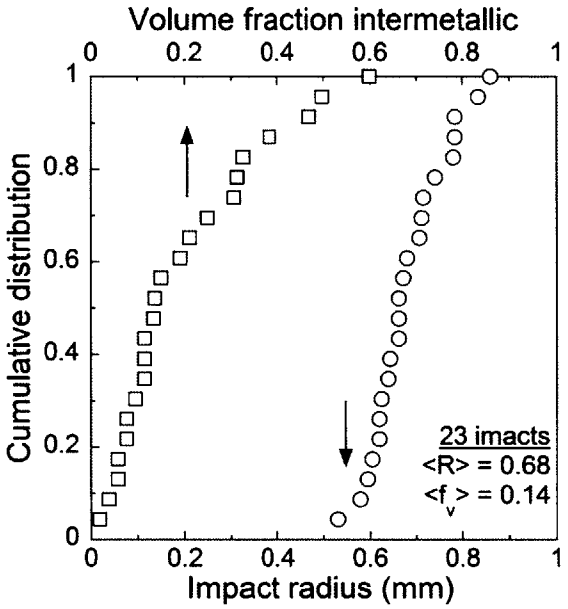

Fig. 2.7 Cumulative distributions for the impact radius and the volume fraction of intermetallic.

Using the average compact radius and fraction of converted, the average mass of intermetallic that will be converted during a single high-energy milling collision can be estimated. For a milling ball of 8 g this quantity is given by:

$$m_{converted} = f_v \pi r^2 h \rho = 0.16\, mg \qquad [2.1]$$

where f_v, *is* the volume fraction of intermetallic (taken to be 0.14), r is the compact radius (taken to be 0.68 mm), h is the compact height (taken to be 0.1 mm [28]), and ρ is the density of the compact (taken to be 7.86 g/cc). The estimated mass converted of 0.16 mg is thus about 10^{-5} times the overall mass of the powder charge, which was 10 g.

To compare this value for of converted mass based on a single collision to global milling kinetics measured in section 2.2, we employ the concept of a normalized rate constant, k, [30] which describes the fraction of the powder charge that will be converted during a single collision. For a continuously decelerating kinetic trend, such as we observe here, the conversion degree can be given by [146]:

$$\alpha = 1 - exp(-kn) \qquad [2.2]$$

where n is the number of collisions. Fig. 2.8 shows a plot of the number of collisions, n, vs $\ln(1-\alpha)$ – as calculated using the XRD-determined conversion degree data from Fig. 2.2. The data has been fitted with Eq. 2.2, with a line of best fit of gradient 3.1×10^{-6}.

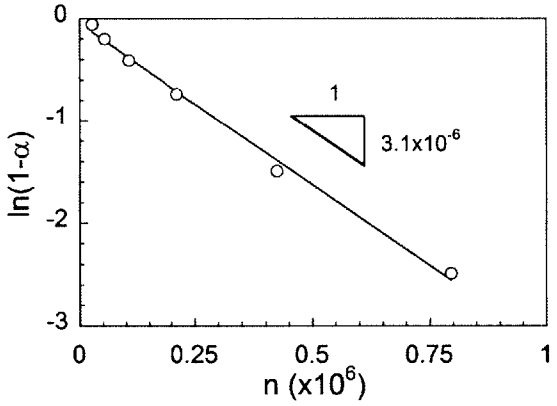

Fig. 2.8 The chemical conversion of Bi_2Te_3 as a function of number of collisions, n. The slope of the line of best fit reveals the apparent rate constant, k for the reaction.

According to the impact energy evaluation performed in section 2.1, for two mechanochemical experiments with different ball mass, m, the rate constants will be related according to:

$$\frac{k_1}{m_1} = \frac{k_2}{m_2} \qquad [2.3]$$

where subscripts 1 and 2 refer to the parameters corresponding to each milling experiment. Converting the kinetic constant observed in section 2.2 to the expected conditions used in the compact experiments of this section therefore yields:

$$m_{converted} = m_p k_2 = m_p k_1 \frac{m_2}{m_1} = 10 \times 3.1 \times 10^{-6} \times \left(\frac{8.35}{2}\right) = 0.13\ \mathrm{m}g \qquad [2.4]$$

The estimate of 0.13 mg is within reasonable experimental error of our estimate of 0.16 mg based on the impact observations given that were quantified in Fig. 2.7. The strong agreement indicates that the chemical conversion mechanism in the presence of liquid Bi that was observed in Fig. 2.6 is the

primary chemical conversion mechanism that operates during high-energy milling of Bi and Te powders.

2.5 Mechanical alloying induced by liquid phases

We have shown that a particle-wise combustion reaction occurs between Bi and Te powders in the presence of molten Bi. The mechanochemical conversion was quantified at the global scale (Fig. 2.8) as well as on the scale of an individual impact (Fig. 2.7). Since this is the first known report of such a reaction, here we compare quantitatively the chemical conversion kinetics with other well-studied mechanochemical processes. A number of other systems [personal communication, F. Delogu] are plotted alongside the results of this study in Fig. 2.9. The rate of mechanochemical transformation is unusually rapid; the energy dose for 50% transformation is about 1.5 kJ/g for Bi_2Te_3 but between 10 and 100 kJ/g for the formation of alloys such as intermetallics undergoing amorphization, and the formation solid solutions. The fastest alloying reaction in Fig. 2.9 besides Bi_2Te_3 is for an Ag_9Bi alloy, which could feasibly be accelerated by the presence of molten Bi. Interestingly, the Bi_2Te_3 reaction is even more rapid than the allotropic phase transformation between HCP and FCC Co, which requires no long-range chemical diffusion.

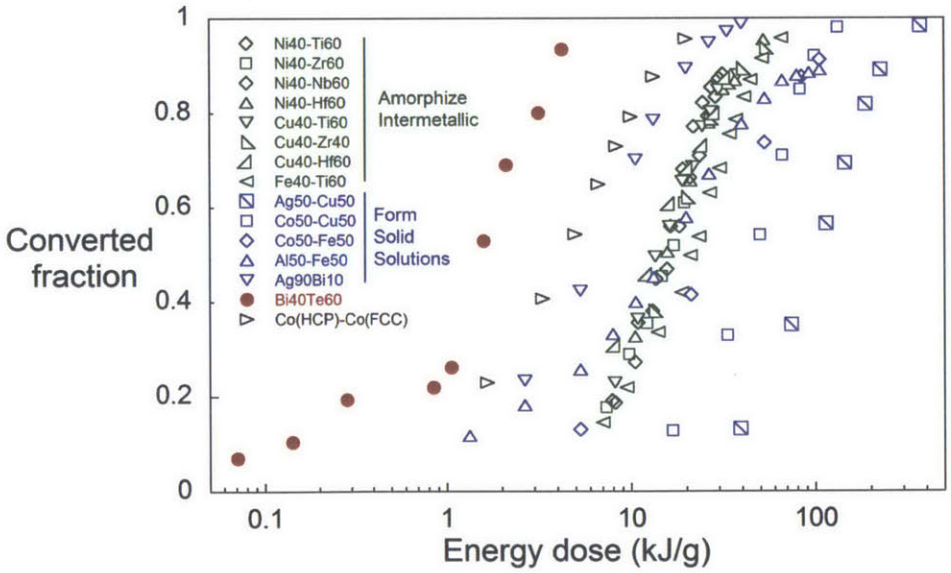

Fig. 2.9 The chemical conversion of Bi_2Te_3 is unusually rapid, as shown in a plot of converted fraction vs Energy dose for a number of other mechanochemical processes [personal communication, F. Delogu].

The abnormally rapid chemical conversion kinetics displayed in the present study, make it of interest to predict what other materials will melt under high energy milling. To achieve this, we consider the impact temperature at a collision site, $T_{imp} = T_{mill} + \Delta T$, where ΔT is the temperature rise. Many authors have modelled the impact temperature rise [28,147,148], and we adopt the form proposed by

Schwarz and Koch [148] who assumed that the maximum temperature rise at an impacted particle can be represented by the problem of a semi-infinite volume with a constant energy flux at its surface:

$$\Delta T = \rho_b v_r^2 \left(4Rv_s/\pi K\rho_p c_p\right)^{1/2} \qquad [2.5]$$

where ρ_b and v_s are material parameters of the ball – density and speed of sound respectively; and K, ρ_p and c_p are the materials parameters of the milled powder – thermal conductivity, density and specific heat capacity respectively. Introducing into Eq. [2.5] the definition of thermal effusivity, $e = \left(K\rho_p c_p\right)^{1/2}$, and the by replacing the temperature rise with: $\Delta T = T_{mill} - T_m$, and rearranging leads to the following expression:

$$\phi = e(T - T_m) \qquad [2.6]$$

where we have defined a new constant that contains parameters specific to the milling conditions, $\phi = \rho_b v_r^2 (4Rv_s/\pi)^{1/2}$. From the criterion of Eq. [2.6], it can be inferred that if $e(T\text{-}Tm)$ is below a critical value of φ set by the milling parameters, then melting will occur during the collision process. Inspection of φ shows that by increasing the milling media radius, impact velocity, or media Young's Modulus, will tend to increase φ and thus enhance the tendency of melting. Fig. 2.10 shows a plot of thermal effusivity vs $T\text{-}T_m$ for a range of metals and semimetals where data was available [149].

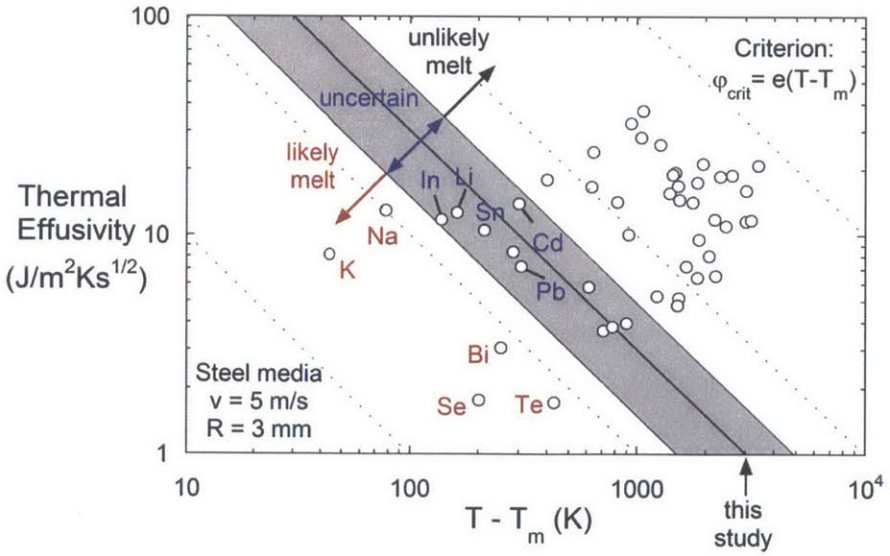

Fig. 2.10 The tendency of an element to melt under high energy milling is represented by the critical parameter, φ, which is the product of thermal effusivity and T-Tm. If φ is greater than approximately 10^5 melting will definitely not occur, while if it less than 10^5 melting is likely.

The plot shows a broad variation in φ values for different materials; almost 3 orders of magnitude exist between the most volatile elements, K, Sn, Bi, Se, Te and the most refractory elements such as W, Nb, Mo etc. Superimposed on the plot is a line for the conditions used in this study, $\varphi = 10^6$. Elements lying well to the left of this line, with $\varphi < 10^5$, are expected to exhibit melting during high energy milling, however for the elements to the right, melting will unlikely be observed. For elements near the line, with $\varphi \approx 10^6$, melting is possible, but will heavily depend on the particular processing conditions. In agreement with this study, Bi lies well to the left of the shaded region, however some other volatile elements – such as Sn, Se and Pb – which are common thermoelectric materials, also lie within a zone where it is feasible that melting could occur.

2.6 Conclusions

The mechanical alloying behaviour of Bi and Te powders has been studied in detail, elucidating a novel mechanochemical reaction involving a particle wise combustion in the presence of molten Bi. We have shown that a particle-wise combustion reaction occurs between Bi and Te powders in the presence of molten Bi. The mechanochemical conversion was quantified at the global scale as well as on the scale of an individual impact. Both techniques indicate that the alloying process occurs with a chemical conversion rate constant that is 1-2 orders of magnitude faster than other mechanochemical processes.

By estimating the temperature rise at an individual collision, the presence of a molten Bi phase can be explained on the basis of the unique thermal and thermodynamic properties of Bi; specifically its low melting point and low thermal effusivity. By extending this analysis to other metallic and semi-metallic elements, some other more volatile elements are predicted to display molten phases under mechanical attrition.

While some experimental reports have suggested the likelihood of melting, to our knowledge this is the first report of a particle-wise combustion reaction that is ignited in the presence of a molten phase. Understanding this mechanism is useful from the point of view of process design and control for the synthesis of nanostructured thermoelectric compounds, which in general have modest negative heats of mixing and can be produced by MA. The explicit documentation of particle-wise explosive reaction also presents an intriguing direction for the better understanding of MA studies in general, where it is far more common to observe either diffusive reaction or a single explosive reaction that propagates through an entire specimen.

Chapter 3: Grain refinement: anomalous energy trends[2]

3.1 Introduction

In chapter 1, we showed that understanding the grain refinement characteristics is interesting for two reasons. Firstly achieving a fine grain size is of interest in engineering terms because the finest grain size endows better thermoelectric properties, as well as enhanced strength and toughness. Secondly the unique thermophysical properties of the compound suggest that the grain refinement behaviour may be different to conventional systems, which offers a unique opportunity to study the physics of grain refinement. In chapter 2, we showed that the Bi2Te3 system exhibits unusual alloying characteristics during the initial stages of milling, where the 2Bi + 3Te → Bi2Te3 reaction occurs explosively, but only on the particle scale. In this chapter, we limit our scope to the deformation induced structural evolution that occurs after the intermetallic is formed. In particular, the evolution of the intermetallic grain structure to a dynamical steady state is our focus, including the effect of processing parameters on this steady state. On the basis of these observations we argue that what governs the steady-state structure is largely the impact temperature at an individual collision site. Bi-2Te3 is found to have uniquely sensitive processing-structure relations, which can be explained by the combination of low melting point and low thermal effusivity of the compound, the latter of which – besides making for a good thermoelectric material – prevents dissipation of the heat of plastic deformation, thus enhancing thermal recovery of mechanically induced defects.

3.2 Experimental methods

Mechanical milling

High-energy ball milling experiments were performed according to the experimental procedures used in chapter 2. However in order to investigate the effect of impact energy, milling experiments were performed at a range of oscillation frequencies, by retrofitting the SPEX mill with a 3-phase motor and a variable frequency drive. The frequency was calibrated independently using a light stroboscope. In some experiments where the milling had to be performed outside the glove box, the vial was initially sealed inside the box and subsequently transferred outside.

In order to monitor the milling temperature, a K-type thermocouple was attached to the exterior of the vial wall and the time-temperature profile was logged on a computer. The milling temperature was also actively varied to achieve three general temperature conditions:

[2] The contents of this chapter have been published previously in reference [150]

i) "T_{low}", below room temperature and generally about -90 ° C. To cool below room temperature (T_{low}) the exterior of the vial was intermittently flushed with liquid nitrogen between 10 minute milling intervals.

ii) "T_{med}", between room temperature and normal operating temperature and generally between 25 and 80 ° C. To vary T_{med}, cooling was applied to the vial surface using a multi-speed fan.

iii) "T_{high}", a higher than normal operating temperature, up to 170 ° C. T_{high} was achieved by insulating the vial in a jacket to allow heat to accumulate.

The previous chapter showed that complete reaction between Bi and Te to form Bi_2Te_3 occurs very swiftly during milling, within about 15-30 minutes, and this remains true for all of the conditions studied in this work. Accordingly, our focus in what follows is for time scales greater than 30 minutes, during which no reaction is occurring, but structural evolution of the intermetallic is taking place.

Powder characterization

Samples of powder were characterized by x-ray diffraction using the same method as chapter 2. However, the Rietveld analysis method was slightly different as all samples were single phase Bi_2Te_3. Here the instrumental broadening was corrected for using a NIST LaB_6 sample. During the Rietveld procedure, the unit cell constants, order dependent broadening (U) and order independent broadening (W) terms were all refined, allowing the volume-averaged grain size, d, microstrain, ε, and hexagonal lattice parameters, c and a to be determined.

Transmission electron microscopy (TEM) on as-milled powders was performed using a JEOL 2010 high resolution transmission electron microscope (HRTEM) operated at an accelerating voltage of 200 kV in bright field imaging mode. TEM specimens were prepared by mixing Bi_2Te_3 powders with a fine Cu powder (to prevent deformation in the Bi_2Te_3), followed by cold pressing into a foil. Ion milling was performed on a Fischione Model 1010 instrument with liquid N_2 cooling to less than 200 K to prevent sample damage [42]. For measurement of grain size, each identified grain was manually traced and measured.

3.3 Results

Fig. 3.1 shows a typical XRD scan of the as-milled powder, showing the difference between the experimental and Rietveld calculated intensities. The small deviation between the two intensities – as indicated by the difference plot in the lower panel – indicates a good quality of fit.

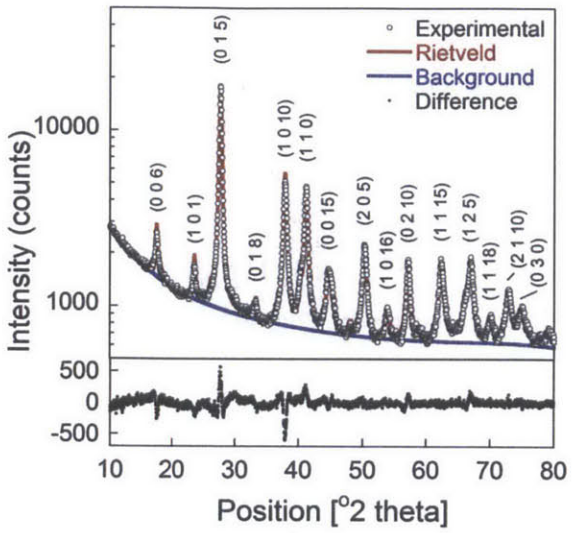

Fig. 3.1 Representative XRD scan on a logarithmic scale, with Rietveld simulation and fitted background overlaid. The difference plot in the lower section – plotted on a linear scale – indicates a good fit.

Fig. 3.2 shows the evolution in grain size of the intermetallic, along with the converted volume fraction of Bi_2Te_3 phase, during a typical milling run. Again we note that the first 15 minutes or so of milling cause the rapid reaction of Bi and Te to form the intermetallic Bi_2Te_3. Subsequent deformation results in a monotonic reduction in the grain size towards a steady state after prolonged milling.

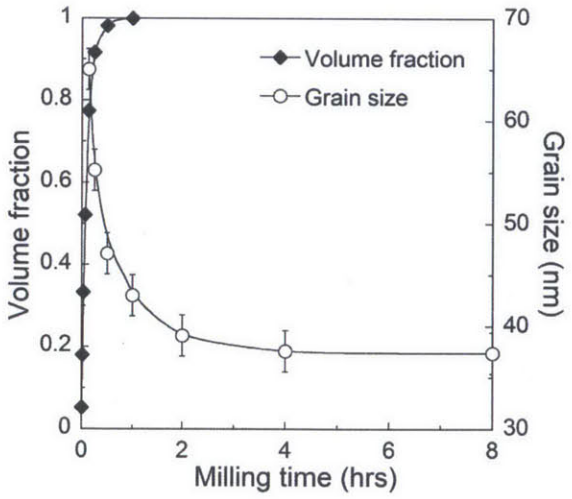

Fig. 3.2 The volume fraction of compound Bi_2Te_3 (rhombuses) reaches near complete formation after 15-30 minutes of milling, after which the grain size (circles) decreases towards a steady state after about 4 hours.

Fig. 3.3 reveals that the steady-state grain size, d_{ss}, increases measurably with milling temperature. Fig. 3.3(a) shows the evolution of grain size, d, as a function of milling time for three different milling temperatures, each with an average media radius of 3.5 mm and a milling frequency of 35.3 Hz. A secondary x-axis of specific milling dose is provided to allow comparison to other milling conditions. Fig. 3.3 also reveals that d_{ss} is reached at a milling time of about 4 hours, or a specific dose of 32 kJ/g, at each temperature. Fig. 3.3(b) shows bright field TEM images of the samples that have been milled to the steady state, confirming the increase in grain size with milling temperature. Fig. 3.3(c) shows the corresponding steady-state grain size distributions measured from at least 300 grains, which is in each case well-fitted with a log-normal distribution as shown by the solid lines. The volume-averaged spherical-equivalent grain diameter agrees well with the XRD data to within about ±2 nm, which is hence used to assign error bars on all reported XRD grain size values.

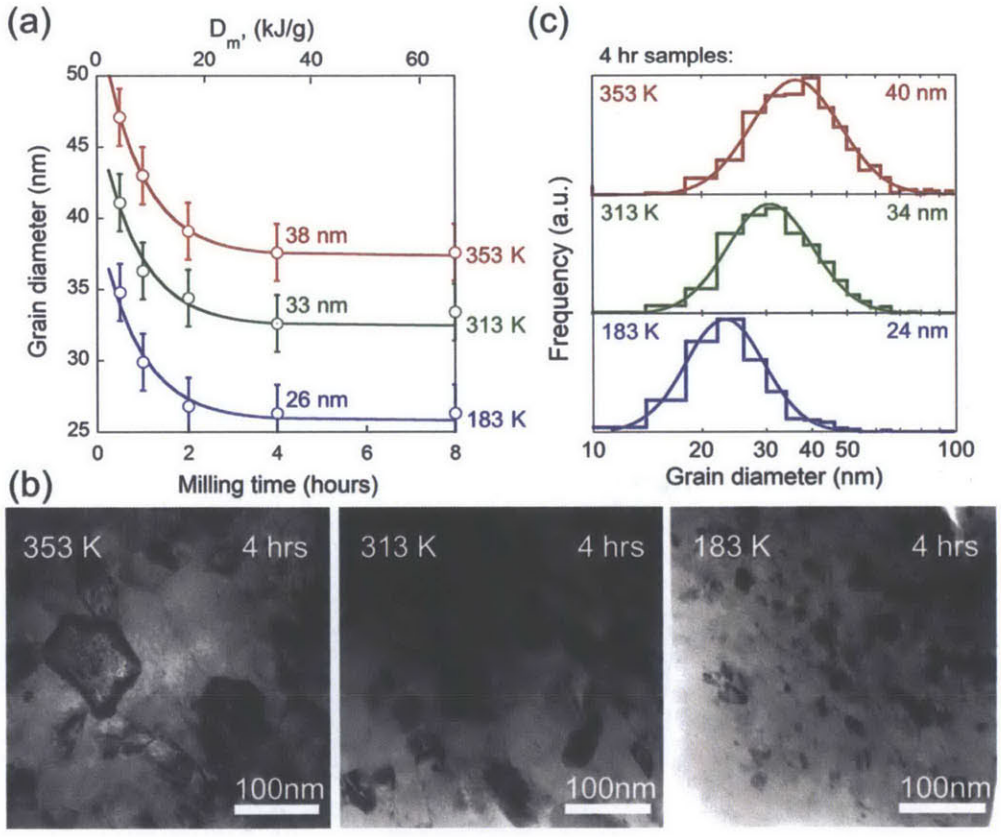

Fig. 3.3 Evolution in XRD grain size as a function of milling time at 183, 313, and 353 K is shown in part (a), while representative TEM micrographs at 4 hours of milling are shown in part (b). Grain size distributions of these samples, as shown in part (c), are log-normal as expected. Volume-weighted average grain sizes on each histogram are in good agreement with XRD.

The final structures achieved after milling, and the corresponding values of d_{ss}, are characteristic of a dynamical steady state governed by the milling parameters. This is shown by comparing the structural evolution from two batches with different starting grain sizes in Fig. 3.4. The first sample

was milled at a high vial temperature to achieve relatively large grain size (42 nm), and the second at a lower vial temperature to a finer grain size (24 nm). For each sample, a subsequent milling treatment was conducted at an intermediate vial temperature between the two extremes. Fig. 3.4 shows the evolution in structural parameters d and ε, along with the lattice parameters c and a for these two samples; under identical milling conditions, both samples converge on the same microstructural state after approximately 1 hour. The initially larger grain size (42 nm) saw a further reduction in d, accompanied by an increase in ε, an increase in a and a decrease in c. The initially smaller grain size (24 nm) experienced grain growth during milling to a new steady-state grain size characteristic of the intermediate conditions used; the lattice parameters and microstructure also showed the opposite evolution from the coarser (d = 42 nm) sample, and also converged to the same steady-state values upon subsequent milling. Error is introduced into the values for ε, a and c due partial relaxation of the structure during room temperature aging. An upper bound for this was determined by aging a series of samples for 24 months, from which the average relaxation in structural parameters observed (which are grain size dependent) is used to assign error bars to all subsequently reported values.

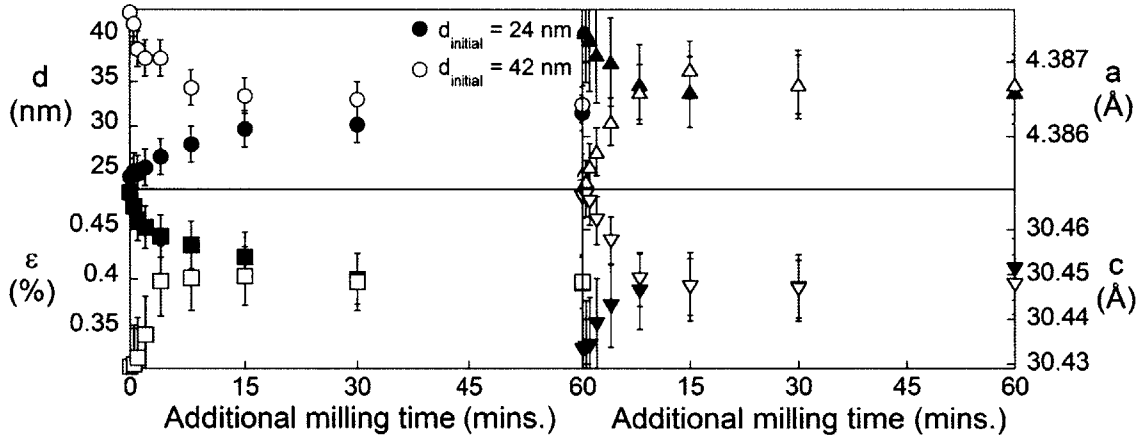

Fig. 3.4 The final grain size is a true dynamical steady state. Starting from two different starting initial grain sizes, 24 nm (closed symbols) and 42 nm (open symbols), both samples converge on the same structural state when milled under identical conditions.

The effect of milling frequency on structural evolution is shown in Fig. 3.5, for three different frequencies: 20, 35.3 and 47.3 Hz. Fig. 5(a) shows that d_{ss} is reached after progressively longer milling times as the frequency decreases. In addition, the value of d_{ss} increases with increasing milling frequency. Fig. 3.5(b) shows the same data re-plotted against the specific energy dose, D_m, which is calculated using Eq. (2). The D_m scaling reveals that the steady state is reached at the same D_m irrespective of N.

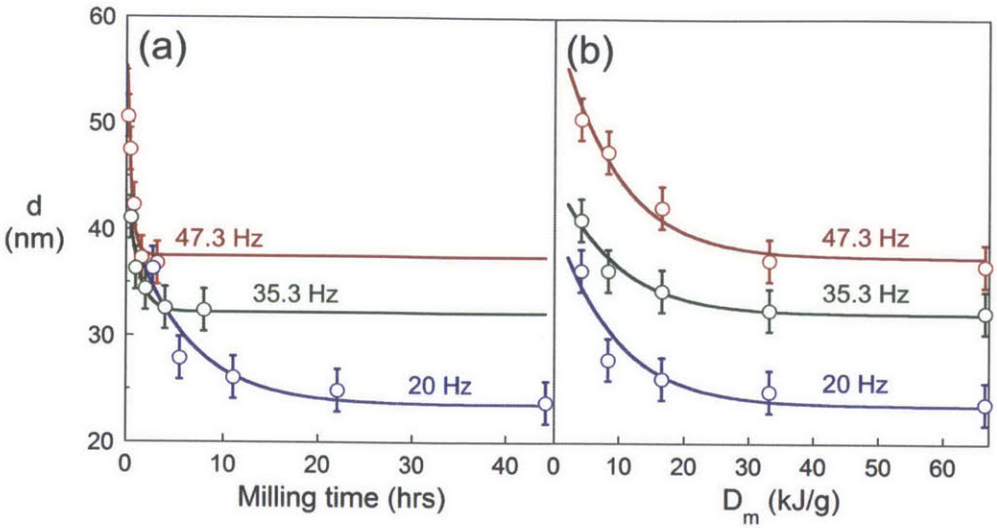

Fig. 3.5 Grain size evolution during milling as a function of (a) milling time, and (b) specific milling dose, D_m, for different milling frequencies, N. The steady state is reached at shorter times under higher N, but at the same D_m of about 32 kJ/g.

The effects of all milling parameters – vial temperature, T_{vial}, milling frequency, N, and media radius, R – on the steady-state structure are shown more quantitatively in Fig. 3.6. Each data point is taken after milling to a specific energy dose of 32 kJ/g, which is equivalent to 4 hours in the un-modified SPEX mill with a frequency of 35.3 Hz, and for simplicity we report just three main structural variables: d_{ss}, ε_{ss}, and $(c/a)_{ss}$. Fig. 3.6(a) shows the effect of T_{vial} in the range 41 to 170 °C. Fig. 3.6(b) shows the effect of N in the range 13.3 to 38.7 Hz. Finally, Fig. 3.6(c) shows the effect of R in the range 2 and 4 mm. For each varied parameter, the other three are kept constant, except in the case of Fig. 3.6(b) where there was a small unavoidable variation in T_{vial} as a result of increased N. This variation was kept to a minimum by employing fan cooling, and the reported range of temperatures in Fig. 3.6(b) covers the full range experienced by the vial during the experiment. We note that three different values of charge ratios were investigated (1.25, 2.5 and 5), by varying the media mass, however no measurable change in the resulting steady-state structure was observed. The essential point of Fig. 3.6 is that increasing milling intensity – by either increasing N or R – tends to mimic the effect of increasing T_{vial}, by increasing d_{ss} and $(c/a)_{ss}$, while reducing ε_{ss}.

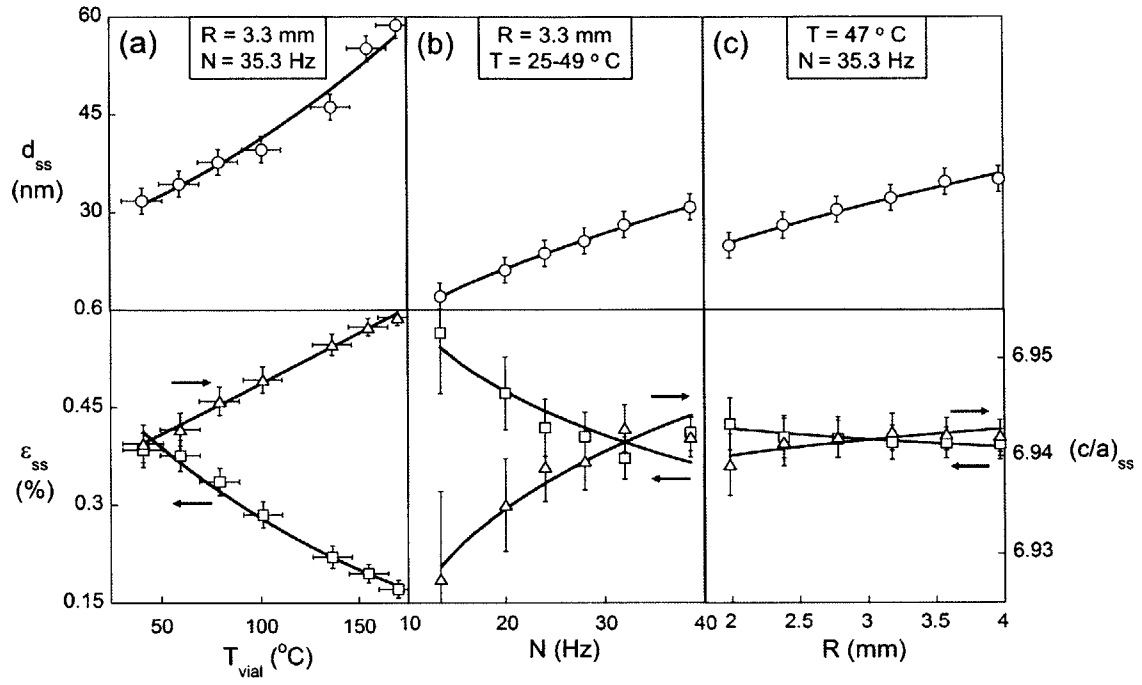

Fig. 3.6 The steady-state microstructural disorder decreases with increasing milling temperature and impact energy. The top panel shows the dependence of the steady-state grain size, d_{ss} on a) vial temperature, T_{vial} (b), milling frequency, N, and (c) media radius, R. The lower panel shows the corresponding change in microstrain, ε_{ss}, and c/a lattice parameter ratio, $(c/a)_{ss}$.

To illustrate how structural variables are linked, Fig. 3.7 shows ε and the deviation in lattice parameters from the literature values [133] - $\Delta c/c_0$ and $\Delta a/a_0$ - as a function of d. Every sample analysed in this study is shown. Clearly ε, Δc and Δa all show an inverse relationship with d, however the sign of the change in c and a are opposite; the unit cell expands in the a-direction but contracts in the c-direction as the grain size decreases. Again, some scatter is introduced in the data due to samples being analysed at varying times after milling, and also minor changes in stoichiometry from batch-to-batch.

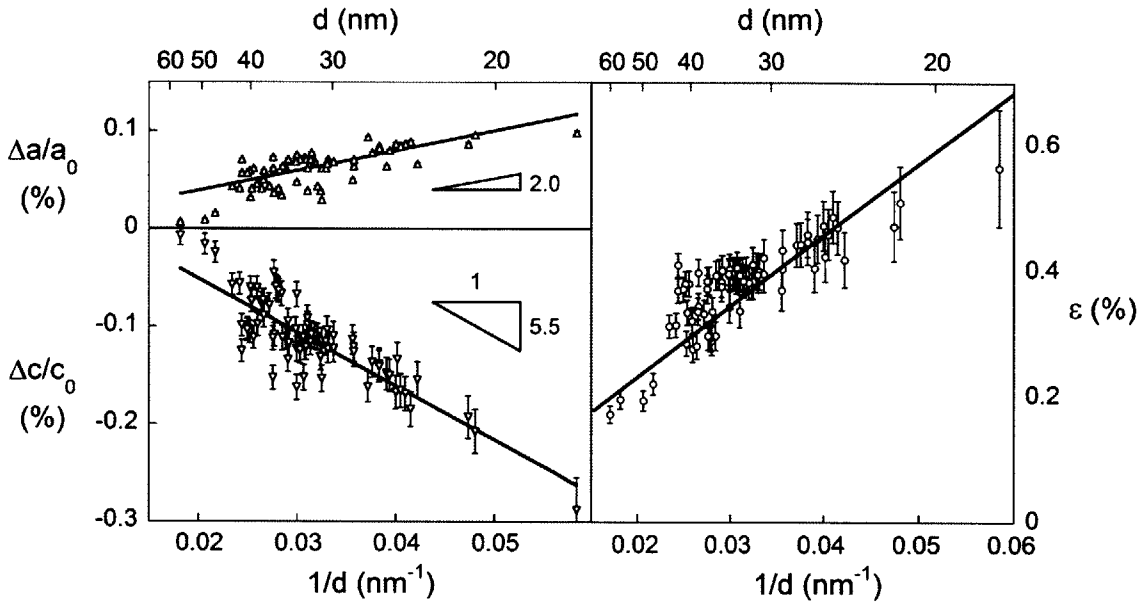

Fig. 3.7 Microstrain (upper panel) and deviation in lattice parameter (lower two panels) follow an inverse grain size dependence across all samples milled in this study. Lattice parameter a increases, while c decreases, relative to literature values [133].

3.4 Discussion

3.4.1 Microstrain and lattice parameter change

The most significant results in this work pertain to the grain size of the milled compound, and the majority of our discussion in the sections that follow will focus upon that feature. However, microstrain from dislocations influences thermoelectric properties due to phonon and electron scattering, while point defects introduced by milling act as charge carriers [43], so these quantities are of engineering relevance. We are not aware of prior reports on the evolution of point and line defects during mechanical milling, and so offer some observations on this issue here.

The monotonic increase in microstrain with decreasing grain size seen in Fig. 3.7 is characteristic of mechanical milling under dislocation-mediated deformation, and has been observed in other mechanically milled materials. For example, during milling of Fe under different conditions, an inverse relationship between grain size and microstrain was observed, although the intercept depended on analysis conditions [65]. In other nc-metals and intermetallics synthesized by mechanical milling a horseshoe trend is sometimes observed [49,151], i.e., a peak in the microstrain is reached at a grain size of around 5-20 nm, with further grain size reduction resulting in decreasing lattice strain, as dislocation mechanisms cease operating and the lattice relaxes [152]. However, we did not observe such a decrease, perhaps because our processing conditions could not achieve finer grains.

The reduction in axial c/a ratio of the lattice parameters away from the literature value of a = 4.386 Å and c = 30.497 Å [133] with decreasing grain size can be explained by increasing concentrations of point defects. As shown in Fig. 3.7, the relative lattice parameter change is larger in the c-axis than in the a-axis. The two slopes are different by a factor of 2.5, which can be explained by the high degree of bonding anisotropy in the Bi_2Te_3 crystal. In particular, the bonding between Te1-Te1 planes is much weaker, resulting in a large anisotropy in the elastic moduli [15] and hence the dilatory stress field imposed by a point defect will mostly be accommodated by straining the weaker inter-planar bonds along the c-axis. Antisites change the c/a ratio by about 0.15 to 0.2% for every 1% change in stoichiometry [153,154]. Alternatively, vacancies can even more readily account for such a deviation, especially since they accumulate preferentially on a specific lattice site. In particular, the fact that p-type stoichiometric Bi_2Te_3 samples will become n-type when subjected to heavy plastic deformation has been explained via an excess formation of $V_{Te}^{\bullet\bullet}$ over V_{Bi}''' [43,155,156]. Vacancies distort the lattice more strongly than antisites, since their coulombic repulsion is twice (for $V_{Te}^{\bullet\bullet}$) or three-times (for V_{Bi}''') that of an antisite.

3.4.2 Effect of milling temperature on steady state

Perhaps the most significant result of this study is the unexpected response of the steady-state grain size, d_{ss}, to variations in the impact energy, E, as shown in Fig. 3.6(b) and (c). What is most abnormal here is that d_{ss} increases with increasing E – which is achieved either by increased ball size or milling frequency. This trend runs counter to experimental investigations of many metals [58,60,65,67–69] and intermetallics [57], where more aggressive milling leads to finer grains, i.e. d_{ss} is found to decrease with increasing E. As we shall see in the coming sections, we attribute the unique response of Bi_2Te_3 to enhanced thermally-induced recovery effects. Accordingly, it is useful to begin by examining the temperature dependence of d_{ss}.

The steady-state milled structure of Bi_2Te_3 is unusually sensitive to the processing temperature. Fig. 3.6(a) shows that with an increase in vial temperature of only 130 ° C, the compound experiences an approximate doubling in d_{ss} from ~30 to ~60 nm. Similar enlargement of the microstructure with increasing milling temperature is observed in other metals [56,58,60,61] and intermetallic compounds [56,59], however the change is usually less extreme than we observe here. Literature studies of ordered intermetallic compounds, subjected to ball milling at various temperatures are summarized in Table 3.1. For example, in the compound Fe_3Si, over a larger increment of 277 ° C, d_{ss} increased almost imperceptibly from 8.2 nm to 9.2 nm. Other compounds see a similar small change of a few nanometers over a comparable temperature range [56,59]; all of these are very small compared to that seen in Bi_2Te_3, which is also shown in Table 3.1 for comparison.

Table 3.1 Change in steady-state grain size over the range in milling temperatures explored for this study, compared to other ordered intermetallic compounds in the literature.

Compound	Equilibrium structure	T_m (° C)	T_{mill} (° C)	d_{ss} (nm)
Bi_2Te_3	h*R*15	585	41	32
			170	59
Fe_3Si [56]	c*F*16 ($D0_3$)	1246	23	8.2
			300	9.2
FeAl [59]	c*P*2 (*B*2)	1310	70	7
			300	13
Ni_3Fe [56]	c*P*4 ($L1_2$)	1426	23	13.4
			300	18.7

We attribute the increased sensitivity of Bi_2Te_3 to its relatively low melting point, which is T_m = 585 ° C, compared to T_m = 1246 ° C for Fe_3Si and even higher temperatures for the other compounds in Table 3.1. For high melting point materials, the steady-state grain size is thought [53] to be limited by the critical distance below which a dislocation pileup cannot exist [157]. Below this grain size other intergranular deformation mechanisms begin to operate, and the limiting grain size is controlled by deformation rates rather than milling temperature. But for low melting point materials the steady-state grain size is governed by a dynamical balance between refinement and recovery trends [53]. At the typical operating temperature of the SPEX mill of 70 ° C, Bi_2Te_3 powders are already above a homologous temperature of 0.4, which is the point at which dislocation climb typically becomes important during deformation and recovery [54]. As such, in Bi_2Te_3 we expect recovery effects to be a controlling factor over the steady state.

The transition between recovery dominated (low-melting point) and deformation dominated (high-melting point) behavior can be seen in Fig. 3.8. The upper section [Fig. 8(a)] shows d_{ss} data taken from Koch et al. for a collection of pure metals [158] plotted against normalized milling temperature (T_{mill}/T_m), where the milling temperature is assumed to be a typical 350 K. Below a homologous milling temperature of about 0.2 there is no clear relationship between d_{ss} and melting temperature [158]. This may be interpreted as the "high melting point" regime where recovery is not significant in the steady-state development. However above about 0.2 T_{mill}/T_m, a clear relationship emerges. Similarly, Fig. 3.8(b) shows d_{ss} data taken from various studies [56,59,60,65] where T_{mill} was varied under identical conditions. A few metals and intermetallic compounds are shown along with Bi_2Te_3 for comparison. Data is scarce, however the same broad trend is observed, with a transition between strong temperature dependence and weak temperature dependence at homologous temperature around 0.2 to perhaps 0.3.

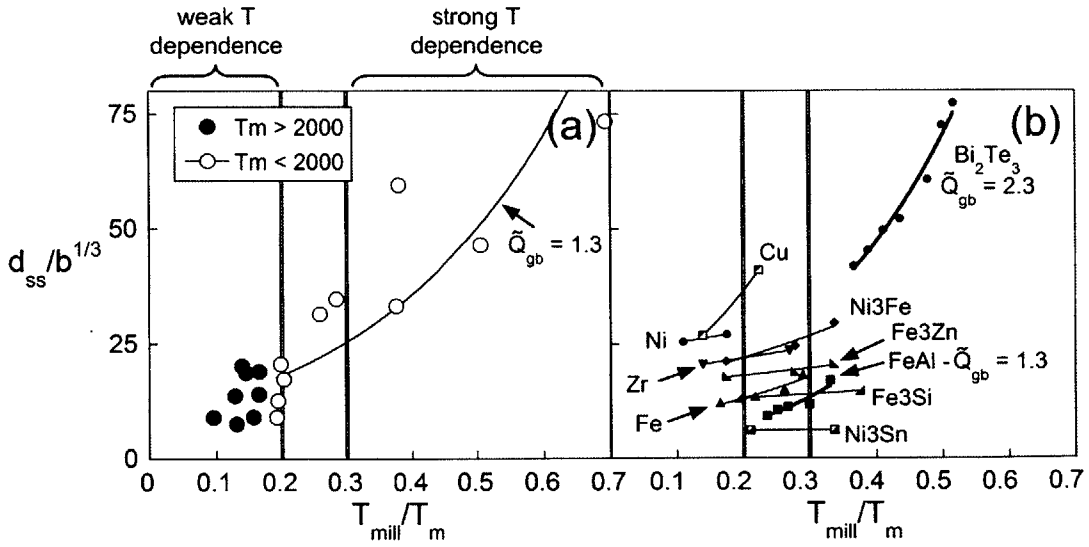

Fig. 3.8 The steady-state grain size becomes increasingly temperature dependent above a homologous temperature of 0.2. Data shown is for (a) pure metals milled at ambient milling temperatures [158] and (b) metals, alloys and intermetallics milled at various temperatures [56,59,60,65]. Eq. (3.2) is fitted to data above 0.2 T_m, yielding a dimensionless activation energy, $\tilde{Q}$, which varies from 2.3 for Bi_2Te_3 to 1.3 in the case of metals and the compound FeAl.

Several authors have modelled the microstructural end-state during severe deformation based on a balance between recovery and deformation processes [159–163]. Following the approach of Bouaziz et al. [163], we envision a grain size below which strain hardening can no longer occur. Their model considers a relatively simple picture of a grain deforming via dislocation shear, nucleating at one side of the grain and traversing across it, resulting in a pile-up at the boundary. Recovery is assumed to occur when the dislocation is absorbed by the boundary, and the resultant atomic displacement is accommodated by re-shuffling of the atoms at the grain boundary via boundary diffusion. By equating the timescales of the two process described, a relationship for the critical grain size is reached [163]:

$$d_{ss} = \left(\frac{D_{gb}b}{\dot{\gamma}}\right)^{1/3} \qquad [3.1]$$

where b is the burgers vector, $\dot{\gamma}$ is the shear strain rate, and D_{gb} is the grain boundary diffusivity. By expressing the diffusivity in its usual Arrhenius form and assigning a dimensionless grain boundary diffusion activation energy: $\tilde{Q}_{gb} = Q_{gb}/RT_m$, where R is the molar gas constant and Q_{gb} is the activation energy for grain boundary diffusion, gives:

$$d_{ss} = \left(\frac{D_0{}^{gb}\exp\{-\tilde{Q}_{gb}T_m/T\}b}{\dot{\gamma}}\right)^{1/3} \qquad [3.2]$$

By assigning a dimensionless activation energy, $\tilde{Q}_{gb}$, we have assumed some proportionality between Q_{gb} and T_m [164]. Fitting Eq. (3.2) to the data from the high homologous temperature region of Fig. 3.8 should thus reveal the apparent activation energy for recovery-controlled milling. Only two materials in Fig. 3.8 present enough data to assess $\tilde{Q}_{gb}$, and its value for Bi_2Te_3 (from the present study) and FeAl (from Ref. [165]) [Fig. 3.8(b)] is determined as 2.3 and 1.3 respectively. Similarly, for the pure metals below T_m = 2000 K [Fig. 3.8(a)] $\tilde{Q}_{gb}$ is about 1.3.

Based on the trends in Fig. 3.8, it seems possible that the value of $\tilde{Q}_{gb}$ for Bi_2Te_3 is somewhat larger than for the other materials simply because this study is probing much higher homologous temperatures not very well covered by prior mechanical alloying literature. In any event, all of the fitted values of $\tilde{Q}_{gb}$ are significantly below those that typically characterize grain boundary diffusion, which for BCC and FCC materials lie between 9 and 12 [164]. This discrepancy could be due to a thermally activated component to deformation [54] which would thus tend to reduce the observed activation energy. A smaller value for $\tilde{Q}_{gb}$ could also be explained on the basis of nanostructured materials containing a large excess free-volume [166]. Although direct measurements of non-equilibrium grain boundary diffusion activation energies are unfeasible, abnormally low activation energies for grain boundary mediated processes such as grain growth [82,89,95,96], sintering [167], and grain boundary relaxation [168] have been reported in nc-materials. Nevertheless, the apparent activation energy for Bi_2Te_3 agrees to within reasonable accuracy with other metals and compounds of similar melting point.

3.4.3 Effect of impact energy on steady state

We now turn to the most surprising result of this study – the anomalous positive correlation between d_{ss} and E. To better illustrate this result, Fig. 3.9 shows the change in grain size, Δd_{ss} as a function of E, as compared to data more typical of the literature, i.e., from Ni, Cu and Fe [68]. The literature trend for Fe has been observed by other authors [65,68,69] in other metals such as Ag, Co, Cu, Ti, Zr [68], Nb [169], the compound NiTi [57], and metalloid Si [68] and well as various ceramic materials [169]. A few other studies have claimed a similar energy trend [171,172] but are more ambiguous since the total energy dose was also varied. By comparison, we are only aware of a single prior report of a positive correlation between d_{ss} and E, for the compound FeAl; a study by Kuhrt et al. [165] showed this trend in a planetary ball mill (Fritsch Pulverisette 5), although a separate study by Pochet et al. [59] using a lower energy vibrating mill (Fritsch Pulverisette-0) indicated the reverse trend with milling intensity. The data from the present work on Bi_2Te_3 stand out in the landscape of Fig. 3.9, because the trend is extremely strong with a positive slope, where the preponderance of literature data is negatively sloped. The trend is also reproduced with two independent series of experiments that

vary the impact energy in distinct ways, via velocity and media radius (labelled as v_r and R in Fig. 3.9 respectively).

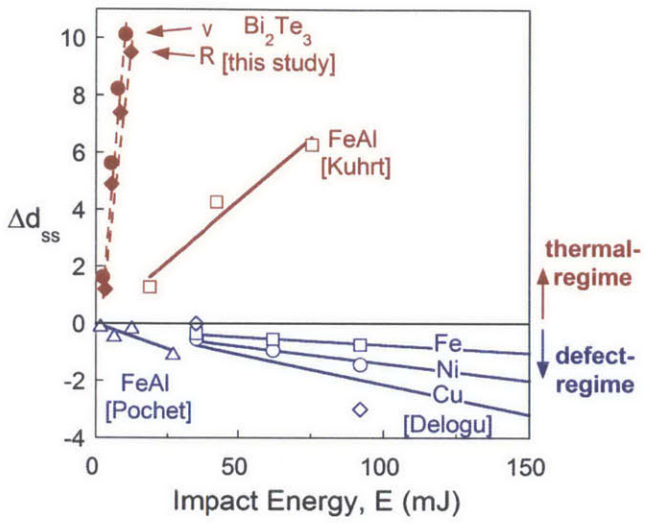

Fig. 3.9 The steady-state grain size change, Δd_{ss}, increases with increasing impact energy, E, in the case of Bi_2Te_3 [this study], but decreases in the case of Cu, Ni and Fe [68]. The two studies of Kuhrt et al. [165] and Pochet et al. [59] report opposing energy dependencies for FeAl.

We believe that the unusual trend of the Bi_2Te_3 data in Fig. 3.9 can be explained by considering the relative importance of deformation vis-à-vis heat creation and retention at the collision site during milling. When a powder particle is impacted, deformation is localized in shear bands [173], within which there is a process of defect accumulation, as dislocations coalesce into sub-boundaries, and subgrains rotate to form high angle grain boundaries [173]. Higher deformation rates that accompany higher impact energies result in more deformation and thus more defect generation. However, the work of deformation in these regions is converted mostly into heat [174], resulting in an attendant local temperature rise, which tends to anneal out some of the generated defects and opposes grain refinement. As a result, there is a tension between the increased rates of both defect accumulation and adiabatic heating that more intense milling promotes. Thus, we envisage two regimes of impact energy dependence, depending on which effect dominates:

1) Defect accumulation regime (hereafter denoted *defect-regime*): the dominant effect of increasing impact energy is a higher rate of defect accumulation, so structural refinement is enhanced preferentially; $dd_{ss}/dE < 0$
2) Impact temperature regime (hereafter denoted *thermal-regime*): the dominant effect is a higher effective time-at-temperature locally at each collision site, which preferentially enhances recovery processes; $dd_{ss}/dE > 0$

The balance between these processes – defect generation and recovery – governs d_{ss} in all low melting temperature materials during milling [51,175]. However, we propose that what is crucially different in the case of Bi_2Te_3 is that greater impact energy promotes more local recovery through adiabatic heating than it does defect accumulation. The local temperature rise at an impact site is controlled by the rate at which the heat of deformation can be dissipated to the surroundings, which can be parameterised by the thermal effusivity [176]. Bi_2Te_3 has a very low thermal effusivity (about an order of magnitude lower than typical metals), and therefore sees far more local heat retention during an impact event; Bi_2Te_3 experiences the thermal-regime, where most materials experience the defect-regime.

The two regimes can be more quantitatively understood by incorporating a dependence on impact energy into Eq. (3.2). To achieve this, we introduce the impact energy of a collision into both the temperature and the strain rate. Although the collision energy was varied parametrically in two ways in this study (by variations in relative velocity, v_r, and media radius, R), as noted above they had a quantitatively similar impact on the grain size, and therefore we consider them interchangeable for the purposes of the present analysis. Considering the trend in terms of relative velocity, v_r, an approximate shear strain rate during a collision is given by Maurice and Courtney [28]:

$$\dot{\gamma} = v_r/Mh \qquad [3.3]$$

where M is the Taylor factor of a polycrystal and h is the thickness of the powder trapped at the collision site. To incorporate the effect of temperature, we replace the ambient milling temperature in Eq. (3.2) with an impact temperature $T_{imp} = T_{mill} + \Delta T$, where ΔT is the temperature rise experienced during an impact. Many authors have modelled the impact temperature rise [28,147,148], and we adopt the form proposed by Schwarz and Koch [148] who assumed that the maximum temperature rise at an impacted particle can be represented by the problem of a semi-infinite volume with a constant energy flux at its surface:

$$\Delta T = \rho_b {v_r}^2 \left(4Rv_s/\pi K \rho_p c_p\right)^{1/2} \qquad [3.4]$$

where ρ_b and v_s are material parameters of the ball – density and speed of sound respectively; and K, ρ_p and c_p are the materials parameters of the milled powder – thermal conductivity, density and specific heat capacity respectively. We can rearrange Eq. (3.4) into a condensed form:

$$\Delta T = \phi {v_r}^2/e \qquad [3.5]$$

where we have defined two constants for the parameters of milling media and parameters of the milled powder respectively; $\phi = \rho_b(4R\nu_s/\pi)^{1/2}$, and $e = \left(K\rho_p c_p\right)^{1/2}$, where e is the thermal effusivity, a measure of the rate at which a material can exchange heat with its surroundings. Combining Eqs. (3.2, 3.3 and 3.5) yields the following:

$$d_{ss} = \left(\frac{A_0 \exp\{-\tilde{Q}_{gb}\frac{T_m}{(T+\phi\nu_r^2/e)}\}}{\nu_r}\right)^{1/3} \qquad [3.6]$$

where A_0 is a constant. Despite its simplicity, Eq. (3.6) now contains the necessary physics to describe the two competing effects of E on d_{ss}. Upon inspection we see that ν_r appears in both numerator and denominator, therefore the grain size could either increase or decrease upon rising impact velocity ν_r, depending on the rate of heat dissipation within the material favoring either the thermal-regime or defect-regime, respectively.

3.4.4 Milling intensity maps

To help understand the competition between defect accumulation and adiabatic defect annealing, Fig. 3.10 shows how d_{ss} varies as a function of E as described by Eq. (3.6). A series of thermal effusivity contours are plotted in the range 2 to 50 kJ/m^2 K s$^{1/2}$, which are physical bounds for most materials (S and Cu have the lowest and highest values of all the elements at room temperature, at 0.7 and 37 kJ/m^2 K s$^{1/2}$ respectively [149]). Low values of e correspond to higher temperature rise during impact and vice versa. In each curve, the two regimes described are displayed; the defect-regime, characterised by $dd_{ss}/dE < 0$, and the thermal-regime, characterised by $dd_{ss}/dE > 0$. There is a transition from the defect-regime behaviour at low E to thermal-regime at high E. This transition is demarked by a grain size minimum, which shifts to higher E as e is increased. Thus at experimentally accessible impact energies, low e materials will likely experience the defect-regime, whereas high e materials will likely be in the thermal-regime. This distinction agrees qualitatively with the data shown in Fig. 3.9, where the defect-regime materials Cu, Ni and Fe have very high values of e = 37, 19, and 17 respectively [149], whereas thermal-regime materials Bi_2Te_3 and FeAl have much lower values of e of 1.5 [1] and 4.5 [177], respectively.

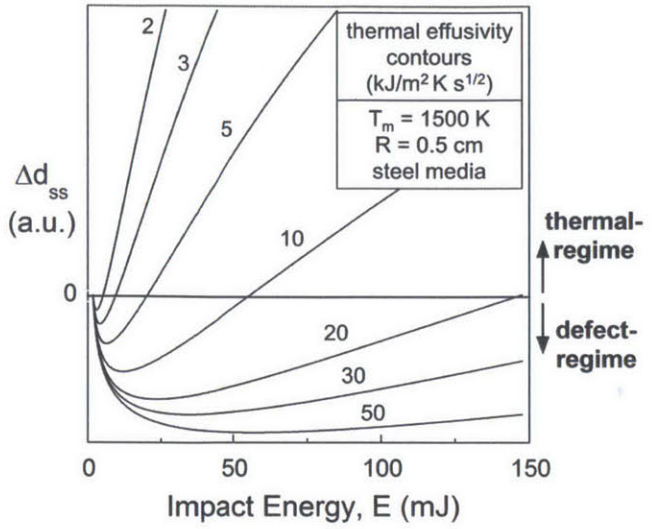

Fig. 3.10 Change in steady-state grain size as a function of impact energy using Eq. (3.6), for various values of thermal effusivity, e. Thermal-regime behavior ($dd_{ss}/dE > 0$) is predicted at low e and defect-regime behavior ($dd_{ss}/dE < 0$) at high e. For intermediate e, a transition between regimes occurs at intermediate impact energies.

Combining impact energy with temperature dependence, Fig. 3.11 shows the grain size landscape for two materials belonging to each regime: Bi_2Te_3 and Fe, plotted on axes of temperature and milling energy. The faces slope in opposite directions, reflecting the fundamental difference in E-dependence. In Bi_2Te_3 the steady state is minimized at low E and low T, whereas in Fe the minimum is at high E and low T. These trends agree well with the available experimental data points [58], which are plotted alongside for comparison.

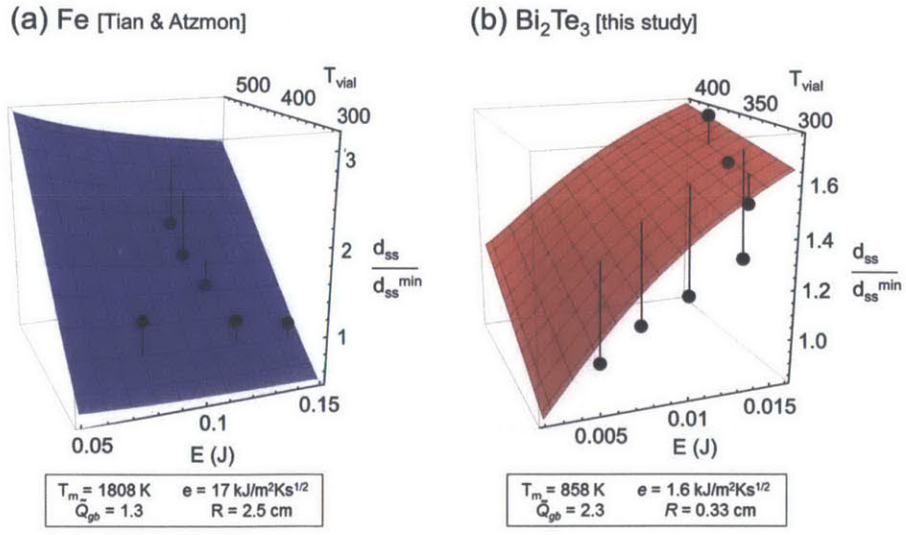

Fig. 3.11 The grain size landscapes (E vs T_{vial}) of Fe and Bi_2Te_3 have oppositely sloping faces, as predicted by Eq. (8). Fe is minimized at high E and low T_{vial} whereas Bi_2Te_3 is minimized at low E and low T_{vial}. Experimental data points [65] are overlaid and connected by verticals to the surface of Eq. (8), showing qualitative agreement with the model trends.

The point of crossover between the thermal and defect-regimes can be interpreted literally as the point where there is a slope inflection, i.e., $dd_{ss}/dE = 0$. Taking the derivative of Eq. (3.6) with respect to v_r and setting it equal to zero yields:

$$(Te)^2 = e\phi {v_r}^2\left(\tilde{Q}_{gb}T_m - T\right) - \phi^2 {v_r}^4 \qquad [3.7]$$

If the quantity $(Te)^2$ is larger than the quantity on the right, then $dd_{ss}/dv_r < 0$, i.e. the defect-regime is predicted, and vice versa for the thermal-regime.

Eq. (3.7) may be broadly useful in differentiating expected behaviors across a variety of materials, although the inputs to it are subject to large variations, dependent on microstructure, purity, etc. The analysis is also relatively simple, and neglects a variety of secondary but important material properties which could affect the steady-state milled grain size, such as stacking fault energy, phase strengths, elastic properties, etc. [51,52]. And of course, in comparing Eq. (3.9) to available experimental data, all of the errors and uncertainties in the experiments themselves enter in, and are variable across the many different labs and protocols for processing and characterization. With these caveats in mind, we nonetheless find it instructive to assemble a "milling intensity map" as displayed in Fig. 3.12. The map is presented on axes of T_m and e, where a given material is represented by a single point. Property data is collected from various sources for metals [149] and ordered compounds [177–183].

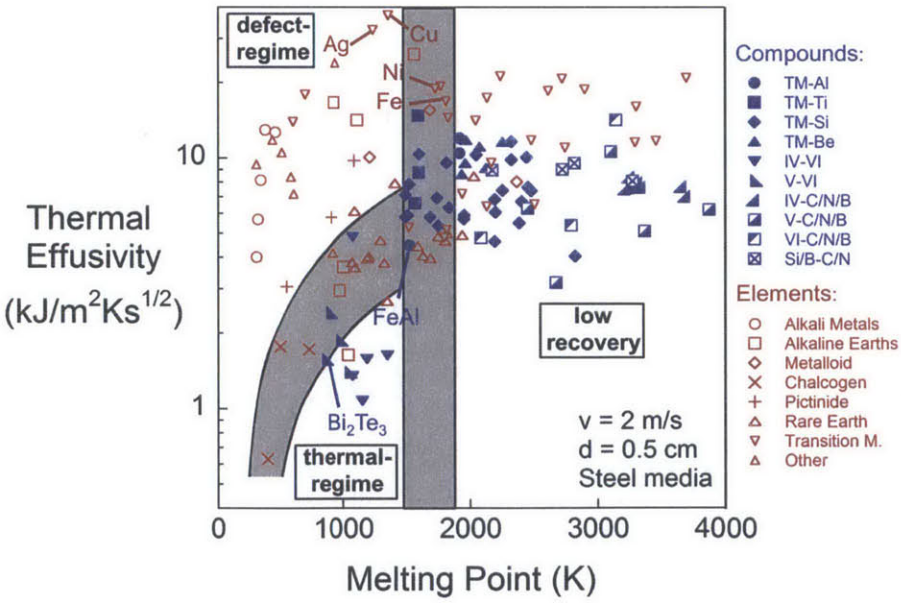

Fig. 3.12 A milling intensity map delineating materials exhibiting "defect-regime" ($dd_{ss}/dE < 0$) or "thermal-regime" ($dd_{ss}/dE > 0$) behavior. Shaded divisions indicate uncertainty in $\tilde{Q}_{gb}$ (between 1.3 and 2.3). Bi_2Te_3 and other V-VI compounds lie within the thermal-regime, with most materials in the conventional defect-regime. A region of "low recovery" is sketched where recovery only plays a limited role – uncertainty in the homologous temperature is shown as shaded region.

Following our earlier discussion surrounding Fig. 3.8, we first separate out the high melting point materials, for which thermal recovery effects are not determinant of d_{ss}; these are in the right half of Fig. 3.12 labelled "no recovery" and not relevant to the present discussion. The left side of the plot is the range where d_{ss} is determined chiefly by the dynamic competition of thermal recovery and impact, and the concave-down arc drawn through this space is the dividing line between the defect-regime (above the curve) and thermal-regime (below the curve); the curve is a representation of the condition $dd_{ss}/dE = 0$, used to derive Eq. (3.7). The width of the shaded region arises from uncertainty in the measured values for the activation energy, and encompasses a range of $\tilde{Q}_{gb}$ values between that measured for Bi_2Te_3 (2.3) and metals (1.3).

What is most quickly clear from examination of Fig. 3.12 is that most low-melting temperature materials lie in the defect-regime, which is the regime of standard behavior where more intense milling leads to finer grains; this aligns with intuition, as in most materials intense milling promotes deformation and refinement more than it does temperature rise and recovery. Only a few materials lie unequivocally in the lower region where more intense impacts generate preferentially more heating and recovery than they do refinement.

This mapping tends to agree with available experimental evidence. Firstly, Bi_2Te_3 is one of the rare materials that occupy the thermal-regime, and should exhibit increasing grain sizes with milling intensity, which is exactly what we have observed in the present study (cf. Fig. 3.6). Some other V-VI compounds such as Sb_2Te_3, and Bi_2Se_3 also lie within the thermal-regime, and would be worthy of detailed study during mechanical milling. Secondly, the metallic materials which have been observed in the literature to display defect-regime behavior, such as Ag, Cu, Ni, Fe, etc. [170] all lie as expected, well with the defect-regime in Fig. 3.12. Finally, the intermetallic FeAl, which to our knowledge is the only other material previously reported to show thermal-regime behaviour, lies within the shaded region between the two regimes. This placement, on the borderline between the two regimes, even helps provide clarity on why the two studies on FeAl discussed in section 3.4.2 exhibit different behaviour, with that of Kuhrt et al. [165] showing a positive dd_{ss}/dE and that of Pochet et al. [59] showing a weakly negative dd_{ss}/dE. It is quite possible that the difference between the two studies is due to the different milling devices employed. Kuhrt et al. used a planetary mill – with much higher impact velocity on the order 3-6 m/s, whereas Pochet et al. used a vibrating frame mill – with much lower impact velocities on the order 0.1-0.2 m/s. Therefore it is possible that Kuhrt et al. were probing the high-energy thermal-regime behaviour (as shown in Fig. 3.10), whereas Pochet et al. probing the low-energy defect-regime. This example, along with the predictions of Eq. (3.7), suggests that other materials may also display thermal-regime behavior, given that sufficiently high impact energies could be accessed.

3.5 Conclusions

Our systematic mechanical milling studies of Bi_2Te_3 powders show that the steady-state microstructure is strongly affected by the process parameters. Both higher temperatures and higher milling energies tend to produce larger grain sizes. While such a temperature dependence is ubiquitous across all mechanically milled materials, to our knowledge this is the first experimental report where the steady-state grain size is positively correlated with impact energy with a large and unambiguous slope.

By considering the balance between recovery and refinement during milling, the anomalous impact energy dependence is explained on the basis of the adiabatic heat produced during a collision remaining localized in the region of deformation, promoting localized defect loss through annealing. In Bi_2Te_3, the thermal properties of the powder are such that it retains adiabatic heat more effectively within the deformation zone, causing much higher temperature rises than in most materials. This, when combined with its low melting temperature, leads to enhanced annealing when the impact energy is higher. While the analysis is relatively simplistic, it reflects the interplay between milling energy and temperature across different materials. The resulting milling intensity map delineates regimes of different energy/grain size responses under mechanical milling, explaining which materials may be expected to exhibit the unusual rate response seen here in Bi_2Te_3.

The developments here may also speak more broadly to the role of defect recovery in mechanical milling of nanocrystalline materials in general. In particular, the relationship between deformation rates and recovery is not an area that well understood; current steady-state grain size models assume that the overall strain rate is limited by, e.g., diffusion of impurity atoms [51], however the variability of strain rate through processing conditions that is highlighted in this study ultimately questions this assumption. Inclusion of such variability, which will come from a mechanistic understanding of the rate limiting processes, may lead to improved models for the nanostructure that evolves upon milling. Such models will also rely on high-quality data; systematic mechanical-milling studies of some more common low-melting point materials are needed.

From an engineering perspective, this work provides guidelines for the processing of thermoelectric materials based on Bi_2Te_3 and its solid solutions. Not only are the finest grain sizes – which are attractive from the device-efficiency point of view – reached, counterintuitively, under lower energy milling conditions, but a greater degree of other structural disorder in the form of point and line defects is introduced along with the grain refinement. These excess defects are retained to some extent after consolidation, and therefore the need to control milling conditions is critical in understanding and controlling the thermoelectric properties.

Chapter 4: Nanocrystalline Recovery and Grain Growth

4.1 Introduction

Grain growth in nanocrystalline thermoelectric compounds reduces the effectiveness of grain boundary scattering, and therefore mitigating grain growth is crucial. In order design such materials that are resistant to grain growth, and provide baseline data for their comparison, a firm understanding of the grain growth process is needed. Such microstructural understanding can also offer predictive power when designing consolidation strategies that minimise grain growth and provide engineering limitations for device use at high temperatures.

As discussed in Chapter 1, although growth of coarse-grained materials is reasonably understood, in nc-materials new phenomena may emerge. Many experimental reports of nanocrystalline Bi_2Te_3-based materials indicated significant grain growth that occurs during the consolidation stage, but these offer only a two data-point view, and without systematic study no quantitative conclusions may be drawn.

The objective of this chapter is to present a systematic investigation of grain growth in a nanocrystalline Bi_2Te_3 alloy. To track changes in structure, we combine detailed X-ray diffraction, differential scanning calorimetry and transmission electron microscopy. By quantifying the kinetics of structure evolution, the rate limiting process for grain boundary migration is argued to transition from a short-range strain-relaxation process at low temperatures to long-range grain boundary diffusion at higher temperatures.

4.2. Experimental methods

Nanocrystalline Bi_2Te_3 powders were fabricated by mechanical alloying according to the methods discussed in chapter 2 and 3. In order to minimise the grain size, relatively low energy milling conditions employed. As such, milling balls of 1.5 g, at a milling frequency of 600 rpm for 22 hours.

The as-milled powders used in this study were themselves of micrometer dimensions (10-100 μm diameter in general), but internally had a fine grain size with a narrow size distribution – as characterized in Fig. 4.1. Part (a) shows a grain size histogram – taken from 345 grain tracings – indicating a volume averaged spherical equivalent diameter of 21 nm. Fig 1(b) shows a representative TEM micrograph from which the grain tracings were taken, indicating a fine equiaxed grain structure. The average grain size from TEM agrees well with the result from XRD analysis – which indicated a grain size of 23 nm and a microstrain of 0.51%.

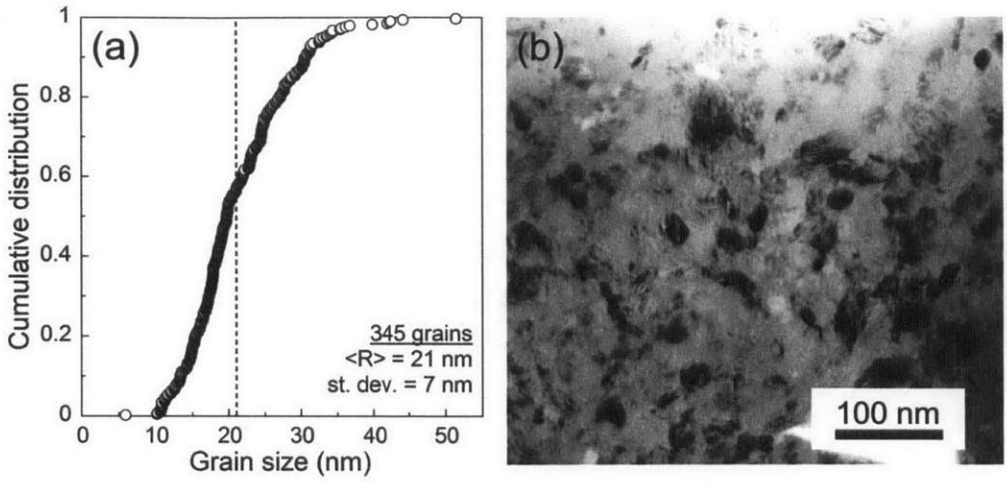

Fig. 4.1 The as-milled grain structure after mechanical alloying. Part (a) shows the a grain size histogram taken from grain size statistics of 345 grains, while part (b) shows a representative transmission electron microscopy image taken in bright-field imaging mode.

Heat treatment of the powders was performed via one of two methods, depending on the length of treatment. For anneals shorter than 1 hour, approximately 200 mg of powder was sealed within small foil packets made from 100 μm thickness stainless steel foil and immersed in a molten salt bath. Once the treatment time elapsed, a rapid quench was performed by rapidly transferring the wrapped specimens onto a large copper block. This allowed for accurate isothermal anneals as short as 5 minutes. For annealing treatments longer than 1 hour, powders were filled into an Alumina crucible and annealed in a Mettler Toledo DSC/TGA 1 with high purity argon purge gas. The powder was heated at 10 K/min to the set point temperature, followed by air cooling.

After heat treatment, samples of powder were characterized by x-ray diffraction and transmission electron microscopy (TEM) according to the procedure described in Chapter 3. Differential scanning calorimetry (DSC) experiments were performed on powders using a TA Instruments Q100 DSC operated with a purge gas of nitrogen and a liquid nitrogen cooling system. The instrument was independently calibrated to within ±0.1 °C using an In standard. All specimens were sealed inside an aluminum pan and heated from -50 to 400 °C at 50 K/min. A baseline signal was obtained by scanning a coarse grained sample that exhibited no grain growth signal. The baseline sample was annealed at 300 °C for 2 hours, and had grain size well over 100 nm. After baseline subtraction, the irreversible stored enthalpy release was obtained by integrating the area between the curve and a linear interpolation between the beginning and end of the exothermic region.

4.3 Results

Fig. 4.2 shows the evolution in XRD patterns that results from annealing at successively higher temperatures. A series of raw data patterns are shown, taken following 2 hour isothermal treatments in the range 50-300 ° C, along with the as-milled powders. A restricted section of the patterns – between 25 and 55 degrees 2 theta – is shown for clarity. At each annealing temperature, all diffraction peaks can be indexed to the rhombohedral Bi_2Te_3 phase. The successive narrowing of the diffraction peaks at increasing temperatures indicates continual grain growth and strain release.

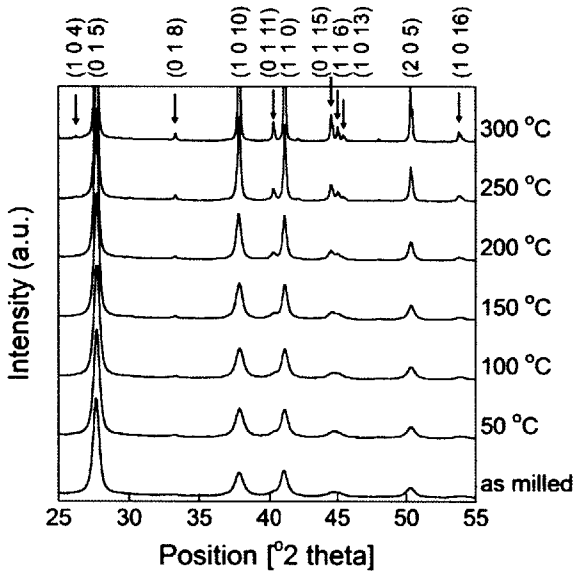

Fig. 4.2 Evolution in XRD linescans for samples annealed in the range 50-300 °C for 2 hours, compared to the as-milled state. A shortened section of the total profile is displayed. At successively higher temperatures, the peaks become progressive narrower as a result of recovery and grain growth.

Relaxation and grain growth can be further characterised by a DSC signature of the as-milled sample, as shown in Fig. 4.3. The upper panel shows a broad exothermic heat release, beginning at about 100 ° C and ending at about 380 ° C. Integration of the peak, as indicated by the grey area under the curve reveals a total stored enthalpy of about 14.9 ± 0.5 J/g. A small endothermic peak of about 22 ± 2 mJ/g corresponding to the melting of 0.08 ± 0.007 % residual Bi phase is observed at 271 ° C. Below the heat release plot are the first and second differentials of the heat flow signal, elucidating the underlying composition of the exotherm. The first differential of the heat flow reveals three clear peaks in curvature, suggesting that the different peaks corresponding to distinct kinetic processes. The second differential gives the location of maxima in these peaks as corresponding minima.

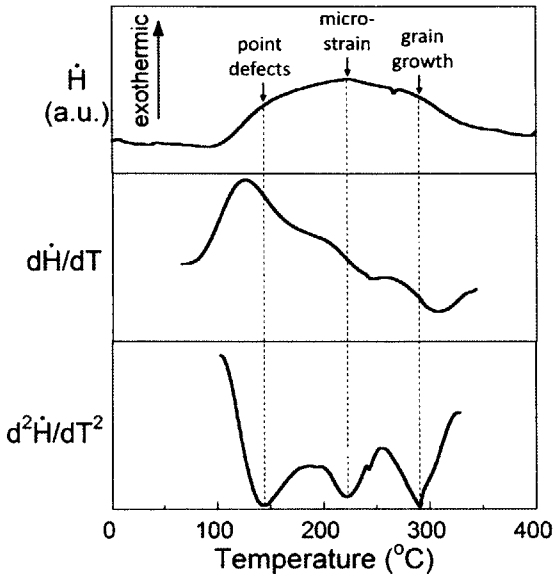

Fig. 4.3 A DSC scan from as-milled powders showing a broad exothermic heat release signal. Differentiation of the heatflow signal reveals three characteristic inflections, indicative of three convoluted peaks in the heatflow signal. The second derivative of the signal corresponding reveals three minima, the temperature of which corresponds reveal the maxima in the original signal.

The evolution in XRD-determined structural parameters, after annealing at various temperatures for 2 hours, is shown in Fig. 4.4. The average grain size, d, microstrain, ε, and lattice parameter ratio, c/a, of the powders are plotted in panels (a), (b) and (c) respectively. Each data-point corresponds to a different sample of powder from the same milling batch. The evolution in d can be well characterized into low and high temperature regions. In the low temperature region – up to about 230 °C – grain growth is very slow, with d increasing from 23 nm to only 37 nm after two hours. On the other hand, in the high temperature region – beyond 230 °C – the rate of increase sharply inclines, reaching 150 nm at 300 °C.

These two regions are further elucidated by the change in ε, shown in Fig 4.4(b). During the sluggish growth process (low temperature region), ε shows a monotonically decreasing signal, while the microstrain is mostly eliminated in the fast growth region (high temperature region). The change in c/a follows this regime change too. From an as-milled value of 6.94, the ratio increases during the slow growth region, reaching a maximum of about 6.96 at 230 °C, whereupon it begins to slowly decrease again, tending towards the literature value for a single crystal of 6.953 [133].

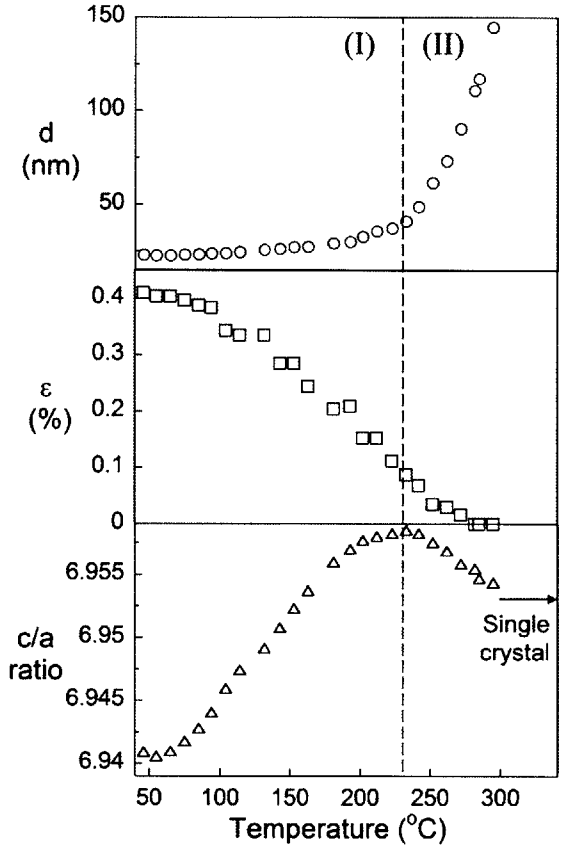

Fig. 4.4 Evolution in grain size, microstrain, and lattice parameter c/a ratio – as determined via XRD – shown in the top, middle and lower panels respectively. Structural evolution can be well-separated into two regimes: Regime I is characterized by sluggish grain growth, large strain release, and relaxation in the lattice. In Regime II on the other hand, grain growth is rapid, microstrain has mainly relaxed, and the c/a ratio deviates only a little from literature value.

The relaxation processes seen in Fig. 4.4 occur even at room temperature, as shown by Fig. 4.5. Structural parameters are compared for powders in the as-milled condition with those naturally aged for 24 months. Five samples of various grain sizes between 17 and 28 nm are shown, corresponding to samples milled at different milling intensities from N = 13.3 to 32 Hz respectively (see chapter 3 for processing details). In all cases the samples received the same milling energy dose in the as-milled condition, thus differing only in initial microstructure (see chapter 3). In each case, both the as-milled and aged samples were drawn from the same powder batch. All samples show similar relaxation behaviour; d changes by only 7%, whilst ε and c/a change by 24 % and 29 % respectively when normalized by the difference between the limiting grain sizes.

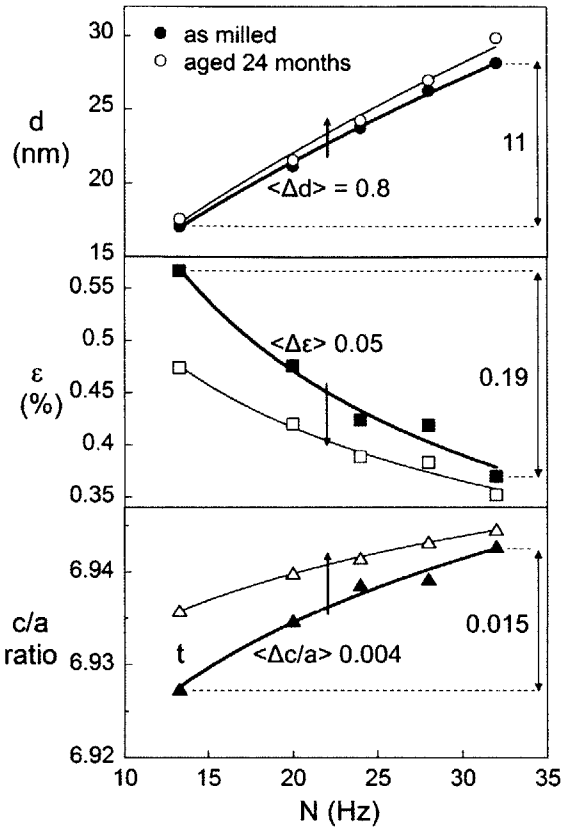

Fig. 4.5 Room temperature recovery and boundary relaxation from the as-milled condition (closed circles) to the 2 year aged state (open circles). Grain size, microstrain and lattice parameter c/a ratio are displayed in the top, middle, and lower panels respectively. While only a small amount of grain growth is detected, there is large recovery in microstrain and lattice c/a ratio.

The kinetics of grain growth are shown in Fig. 4.6, which plots d as a function of annealing time for 7 different annealing temperatures between 160 and 276 °C. The data has been fitted using the following equation:

$$d(t,T)^n - {d_0}^n = k(T)t \qquad [4.1]$$

where d_0 and d are the initial and measured grain size, t is the annealing time, and k is some temperature dependent kinetic constant. Here we fit the data using the least squares method, allowing for only a single value of the exponent n across all of the data series, and a different value of kinetic constant, k at each temperature. The entire dataset is best fitted with a value of $n = 6.5$.

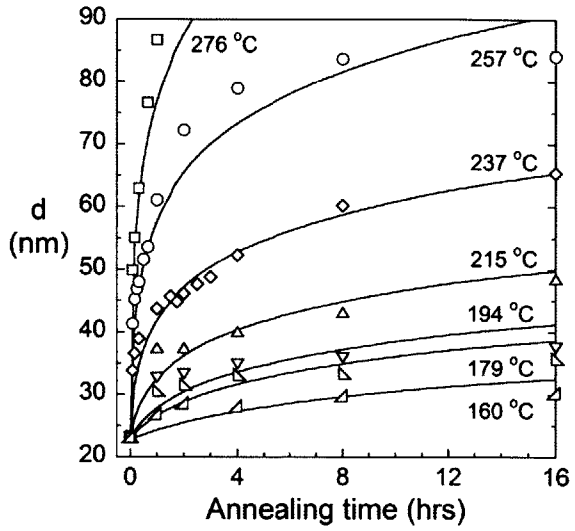

Fig. 4.6 Isothermal grain growth kinetics at a range of 7 different annealing temperatures. The grain size evolution can be well-fit with a generalized parabolic relationship given by Eq. 4.1, with n=6.5, and a variable kinetic constant, k, which is plotted as a function of temperature in Fig. 4.7.

Fig. 4.7 shows an Arrhenius plot of the rate constants returned by fitting Eq. 4.1 to the data in Fig. 4.6. The points can be well fit with two straight lines – corresponding to annealing treatments above and below 230 ° C. This change in behaviour coincides with the low and high temperature regions in Fig. 4. The characteristic activation energy from the gradient of the line corresponds to 89 and 242 kJ/mol for low and high temperature grain growth respectively.

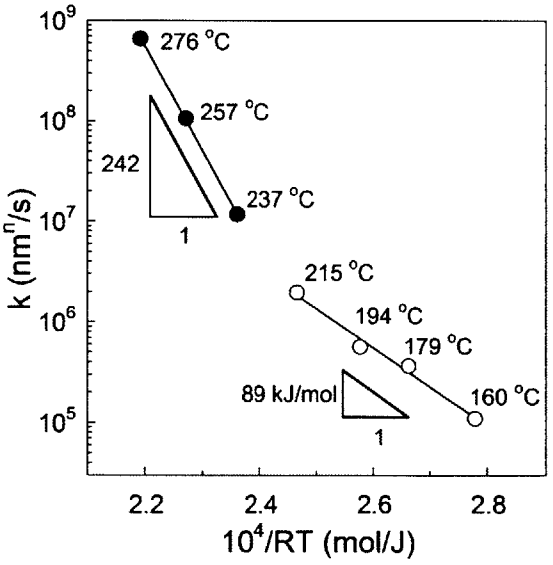

Fig. 4.7 Grain growth rate constant as a function of reciprocal temperature. The rate constants are determined by fitting Eq. 4.2 to data in Fig. 4.6. The point are well fitted with two straight lines, corresponding to high temperature regions (above 230 °C), with an activation energy of 242 kJ/mol, and a low temperature region (below 230 °C), with an activation energy of 89 kJ/mol.

Fig. 4.8 shows good agreement between XRD and stereological TEM grain size measurements. A series of TEM micrographs are shown, taken from powders annealed at 257 °C for 0.25, 1 and 8 hours respectively. The upper left-hand corner shows the grain size distributions taken by tracing grains from a series of micrographs at each annealing time. The grain size distributions are well matched with the expected log-normal distribution, while the volume-averaged spherical equivalent grain diameter agrees with the XRD measurements to within about ± 5 % in the case of 0.25 and 1 hour anneal. For the 8 hour anneal sample, the XRD measurement underestimates the grain size by about 20 %, which is characteristic of a worsening accuracy of XRD as the grain size approaches 100 nm (see Appendix C).

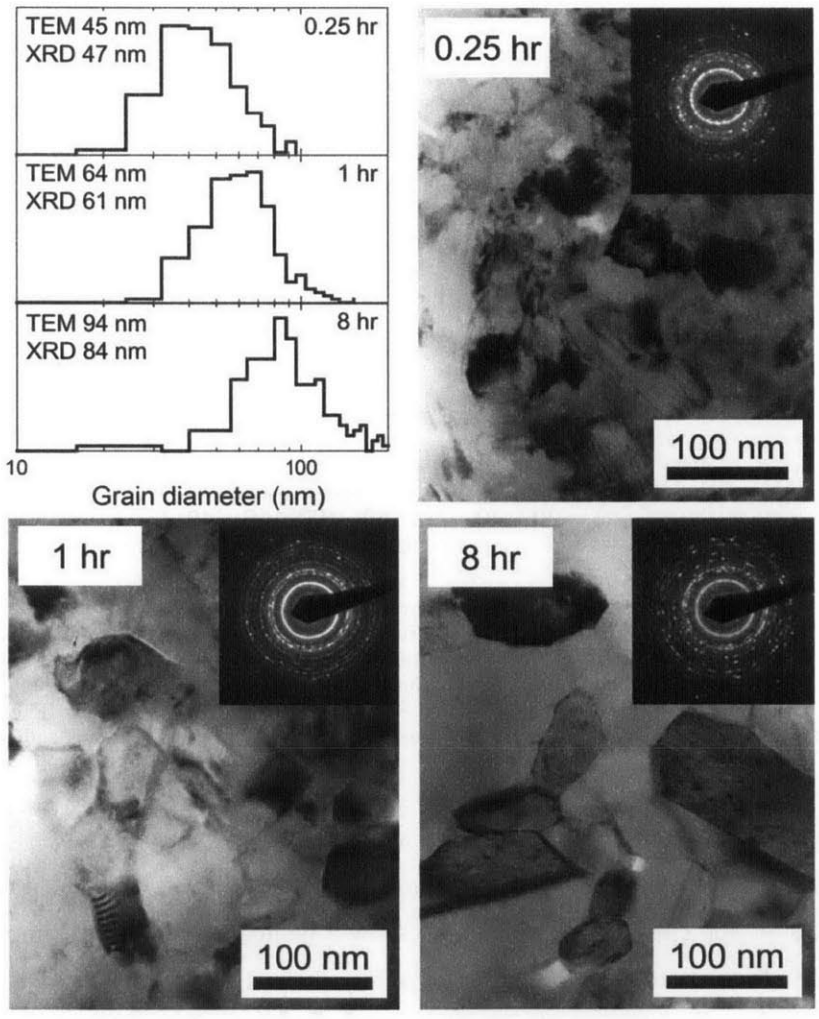

Fig. 4.8 TEM micrographs of powders annealed at 257 °C for 0.25, 1, and 8 hours respectively, with corresponding grain size distributions shown in the top left. The mean grain size – as measured from TEM grain tracings – shows good agreement with XRD measurements.

The relationship between microstrain and grain size during growth is elucidated in more detail in Fig. 4.9(a). The strain release can be well fitted with a power-law equation [184] of $\varepsilon = 0.01(d/d_1)^{-m}$ where d_1 is the grain size and n is the scaling exponent. Fitting the data using the method of least squares results in $d_1 \approx 16$ nm, and $m \approx 2.5$. Excess strain release during grain growth is highlighted by the best-fit line of data for as-milled powders (chapter 3) , where ε was found to follow a *1/d* relationship. Fig. 4.9(b) shows the corresponding *c/a* value as a function of *d*. The lattice parameters initially relax much faster than the microstrain, levelling off at around 40 nm. The slow decrease in the lattice parameter thereafter is characteristic of high-temperature precipitation of a small amount of Te-rich phase (discussed in chapter 5).

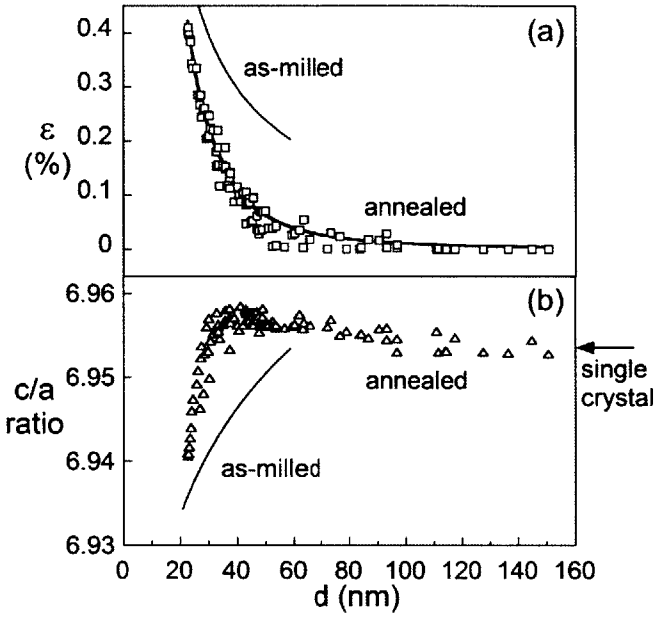

Fig. 4.9 (a) Microstrain and (b) lattice c/a ratio as a function of grain size for all annealed samples in this study. The microstrain decreases monotonically with grain size, and is fitted with a parabolic grain size relationship with an exponent of 2.5. The c/a ratio increases initially, peaks at about 40 nm and then decreases slowly. For comparison, the structural data taken on as-milled samples at a range of milling conditions (chapter 3) is indicated by a line of best-fit for inverse grain size dependence.

A direct view of the relaxation process is seen in the HRTEM images of Fig. 4.10. The left-hand image shows a sample annealed at 260 $^{\circ}$C for 0.25 hrs while the right-hand image shows one annealed at 330 $^{\circ}$C for 2 hrs. While the images show a limited section of the sample, they broadly reflect multiple observations in different grains across the rest of the sample from which they are taken. The images are both viewed normal to the prismatic plane, and the stripe pattern thus corresponds to basal atomic rows. The sample annealed at the lower temperature (which had a measured microstrain of 0.06 %) contains many retained defects such as stacking faults – which are observed by variations in lattice spacing – and dislocations – which are seen as discontinuities in the atomic rows. By contrast, the sample annealed at higher temperature exhibits a more homogenous

structure with no visible defects over the same field of view, which is in agreement with XRD measurements showing immeasurably small ε.

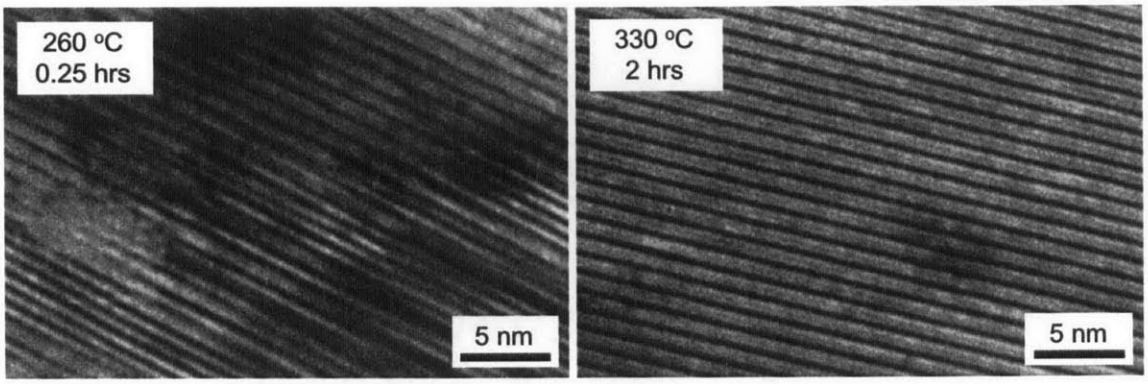

Fig. 4.10 High resolution TEM of the grain interiors – as viewed along the basal plane – after different annealing conditions. The sample in the upper micrograph, which was annealed at 260 °C for 15 minutes, shows a highly disordered grain interior with many dislocations and stacking faults. The sample in the lower micrograph, which was annealing at 330 °C for 2 hours, shows no observable lattice defects.

To investigate further the origins of stored enthalpy in the powders, Fig. 4.11 shows a series of DSC scans from powders first annealed at a higher temperature for 2 hours; the series examines successively higher annealing temperatures from top to bottom. In all cases, the heat exotherm begins at a temperature about 40-50 ° C beyond the prior annealing temperature. The total stored enthalpy progressively diminishes with increasing annealing temperature, falling to zero as the annealing temperature approaches 300 °C.

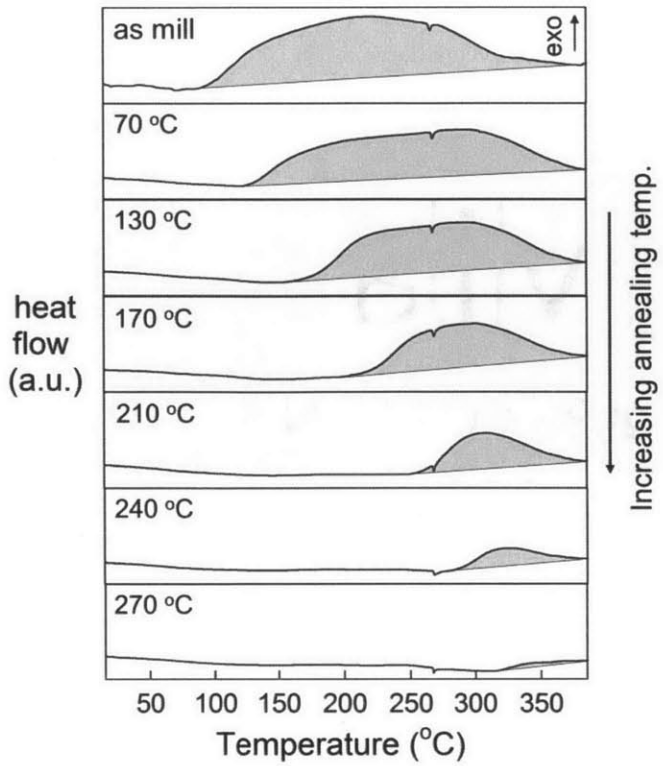

Fig. 4.11 DSC scan evolution for annealed powders, showing the reduction in stored enthalpy with annealing temperature. The as-milled scan is shown alongside samples annealed for 2 hours in the range 70-270 °C.

Fig. 4.12 shows the enthalpy retained after annealing of these powders, as revealed by the DSC scans in Fig. 4.11, as a function of reciprocal grain size. The form of the x and y-axes are selected on the basis of the following expression for the stored enthalpy governed within grain boundaries [185]:

$$H = 2\gamma g V / d \qquad [4.2]$$

Where H is the stored enthalpy, γ is the grain boundary energy, g is a geometric factor accounting for the grain shape, which is estimated to be 1.3 ± 0.2 [185], and V is the molar volume. The axes chosen thusly allow the grain boundary energy in J/m^2 to be read off from the slope. A secondary y-axis in J/g, and x-axis in nm are provided for reference.

The stored enthalpy for as milled, 24 month-aged, and furnace-annealed samples are plotted. After prolonged ageing, the stored enthalpy is shown to fall by about a third. During subsequent annealing treatments, the stored enthalpy evolution can be well fitted by two straight lines. Again, the distinction between the two regions agrees with Fig. 4.4 and Fig. 4.10, with the same delineating temperature of about 230 ° C. The gradient of the high temperature line is 0.26 J/m^2. This represents a measure of the grain boundary energy, since samples in this region contain little microstrain, and therefore other

contributions to stored enthalpy can be neglected. By contrast, the gradient of the low-temperature line is 1.16 J/m^2. This energy is a convolution of the boundary energy plus some additional driving force for grain growth provided by other defects.

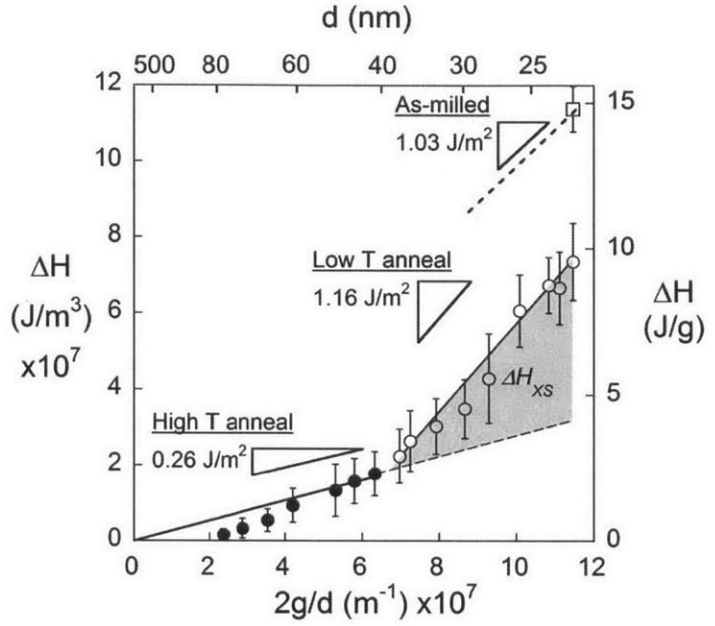

Fig. 4.12 The volumetric stored enthalpy (J/m^3) as a function of inverse grain size. The data is split into three categories: (i) as milled, (ii) annealed below 230 °C, and (iii) annealed above 230 °C, which is the temperature where the activation energy changes (Fig. 4.7). Below this temperature, the grain boundary energy is very high (1.16 J/m^2) because growth is associated with annihilation of defects. Below this temperature, grain boundaries are relaxed, and hence have a much lower stored enthalpy associated with them (0.26 J/m^2).

4.4 Discussion

4.4.1 Stored enthalpy origins

The most striking result of this study is the emergence of two distinct regimes of grain growth – a low activation energy regime at low temperatures, and a high activation energy regime at high temperatures. This is observed directly in Fig. 4.7, and indirectly in Fig. 4.4. Measurements of other structural parameters such as microstrain indicate that the transition in grain growth regime is caused by some sort of structural relaxation. However it is not readily apparent whether this relaxation process is specific to a relaxation of the grain boundary structure, or grain interior defects annealing out. In nanocrystalline materials, both boundary and bulk contributions to lattice strain have been identified. The simplest of all is perhaps the surface driven intrinsic microstrain that is imposed by the size of a grain, which is shown theoretically and experimentally to scale with 1/d [184]. However in the case of ball-milled nanocrystals, a surplus of grain boundary dislocations and regions of excess

free-volume are created as a result of heavy deformation [97]. Thus, relaxation in grain boundary structure upon annealing have been shown to account for changes in grain boundary diffusivity [17,186], and therefore grain boundary mobility could reasonably be affected in this way. Deformation also creates disorder in the grain interior though, which could easily account for the low activation energy region as well. Indeed, super-saturations of point defects have been shown theoretically to account for 'self-locking' of grain growth [90]. Determination of the rate-limiting mechanism is made difficult since many of the specifics of deformation-induced defects in Bi_2Te_3 remain unclear. In order to better understand the defect evolution upon relaxation and grain growth, an appreciation of the various defect contributions to the stored enthalpy is the necessary starting point.

In pure nanocrystalline metals, the stored enthalpy is mostly accommodated at grain boundaries [50], while dislocations only contribute a small fraction – on the order of 1 kJ/mol [50]. However, the non-equilibrium nature of grain boundaries in nc-materials allows them to store more enthalpy per unit area than fully relaxed boundaries – for FCC metals estimates vary between twice as much for Pd [53] and 4-times for Ni [53]. As a result, nc materials can store a significant fraction of the fusion enthalpy, $\Delta H/H_f$. Johnson and co-workers found for a range of metals, that $\Delta H/H_f$ ranged between about 0.06 and 0.43, for Co [50] and Al [53] respectively. The relative amount appears to follow trends for some crystal structures but not others; In FCC materials, higher T_m elements seem to show a lower $\Delta H/H_f$ despite possessing smaller grain sizes in the as-milled state [53]. However in BCC & HCP metals no such relationship emerges. In the case of intermetallic compounds however, the same authors found generally larger values of $\Delta H/H_f$. For a range of Cs-Cl compounds, $\Delta H/H_f$ was between 0.18 and 0.39 for AlRu and SiRu respectively [55]. The additional contribution can be attributed to chemical defect enthalpy.

By comparison, in the present study the stored enthalpy in the as-milled condition was 14.9 J/g or 11.9 kJ/mol, which is only 10% the heat of fusion. This relatively low stored enthalpy is most likely due to the low melting point of the compound Bi_2Te_3 meaning thermal recovery will limit the amount of defect storage. Indeed, the grain size was found to be strongly limited by thermal recovery during milling (chapter 3) and thermally induced relaxation that is observed at ambient temperatures in Fig. 4.5 demonstrates this point explicitly. In order to elucidate how recovery and grain growth are connected, we now estimate the stored enthalpy contributions from various defect sources.

In estimating the origins of stored enthalpy, we consider four dominant defects. The grain interior with contribute: (i) enthalpy form dislocations, E_{dis}, and (ii) point defects, E_{PD}, while within the grain boundary we consider (iii) the relaxed grain boundary energy, E_{GB}, and (iv) an additional contribution due to any excess free volume at the grain boundary as a result of deformation, which we term E_{rel}. The total must therefore sum to the experimentally determined stored enthalpy:

$$E_{stored} = E_{dis} + E_{PD} + E_{GB} + E_{rel} \approx 14.9\, J/g \quad [4.3]$$

Firstly we consider dislocation enthalpy. As mentioned above, dislocations are not expected to contribute significantly; dislocation densities in severely cold worked materials rarely exceed $\rho = 10^{16}$ m^{-2} [152], and this value is probably an over-estimate considering the preponderance of thermally activated recovery in Bi_2Te_3. Nevertheless, using this value we can estimate the stored enthalpy from dislocations [187] using:

$$E_{dis} = \frac{\rho G b^2 (1-\frac{\nu}{2})}{4\pi(1-\nu)} ln\left(\frac{R}{R_0}\right) \approx 1.7\, J/g \quad [4.4]$$

where G is the shear modulus, ν is the Poisson ratio, and b is the dislocation Burgers vector magnitude, which for Bi_2Te_3 are estimated to be G=17 GPa [188], ν=0.3, and b=0.438 nm [189]. R, and R_0 are the outer and inner cut-off radii, taken to be the dislocation spacing $L=\rho^{-1/2}$ and the Burgers vector respectively. As expected, the total dislocation stored enthalpy estimate of 1.7 J/g is low; even using a generous overestimate the total energy is only about 10% of the total stored enthalpy of 14.9 J/g.

Next we consider the grain boundaries. A measure of the relaxed grain boundary energy can be made from the straight line fit to the ordered region of Fig. 4.12, which equates to 0.26 J/g. The relaxed grain boundary enthalpy can be estimated using Eq. 3, for an initial grain size of 23 nm:

$$E_{GB} = \frac{2g\gamma}{d} \approx 3.7\, J/g \quad [4.5]$$

This is considerably more than the dislocation estimation, at about 25% of the as-milled stored enthalpy. However this leaves a further 65% of unaccounted stored enthalpy, which can be attributed to grain boundary relaxation, E_{rel}, and recombination of point defects, E_{PD}. We term the sum of these quantities the excess stored enthalpy, E_{XS}, which is represented visually via the shaded region of Fig. 4.12. These quantities can be estimated on the basis of how the stored enthalpy varied with structural parameters. E_{XS} is plotted in Fig. 4.13 as a function of the microstrain, ε, on the primary y-axis and the deviation in lattice parameter, Δ(c/a), from the literature value plotted on the secondary x-axis. The plot shows that Δ(c/a) converges to the literature value at a larger E_{XS} than ε does, indicating that the majority of point-defects recover at significantly lower temperatures than the remaining grain boundary defects. A lower bound for the excess grain boundary enthalpy, E_{rel}, can be made from the intercept of the Δ(c/a) curve with the x-axis, which is about 4 J/g, or just over 25% of E_{stored}. We therefore consider the remaining defect contribution of 40% E_{stored} to come from point defects. This could arise from antisites and constitutional vacancies.

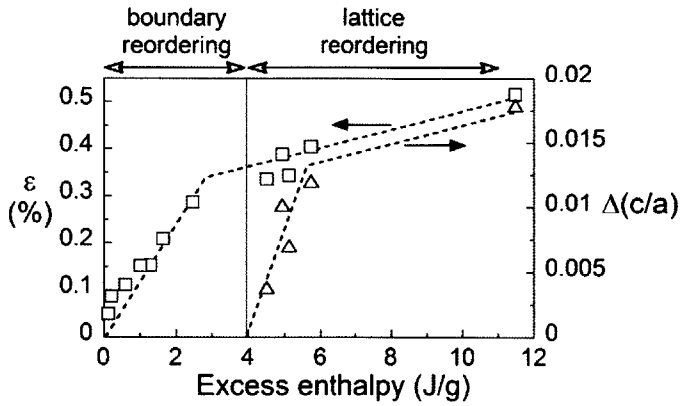

Fig. 4.13 The excess enthalpy plotted as a function of the microstrain, ε, on the primary y-axis and the deviation in lattice parameter, Δ(c/a), from the literature value on the secondary x-axis. The plot shows that Δ(c/a) converges to the literature value at a larger excess enthalpy than ε does, indicating that the remaining excess enthalpy can be attributed to recovery of grain boundary defects.

A crude estimate of the point-defect concentration can be made by correlating this value to calculations of point defect energies in the literature [11]. Energies for Bi_{Te} antisites have been calculated using density functional theory [11] – and we take the average value of 0.9 eV between the Te-rich and Bi-rich values as a first-order estimate. With this antisite defect energy, we can now estimate the concentration as $n = E_{PD}/eE \approx 3.6\text{x}\ 10^{18}\ /\text{cm}^3$,where e is the charge of an electron = $1.6\text{x}10^{-19}$.

While this stored enthalpy analysis is rather approximate in nature, it reveals a salient point about the driving force for grain growth. Contrary to the assumptions of the grain growth model, approximately 75% of the total stored enthalpy comes from defects other than the relaxed grain boundary. During the initial stages of grain growth these defects anneal out, therefore reducing the effective driving force for further grain growth.

4.4.2 Activation energy: grain growth regime transition

With the above understanding of the relative energetic contributions occurring during the recovery process, we now turn our analysis to the transition in grain growth activation energy from low to high temperatures. Point and line defects do not account for all of the excess stored enthalpy in the as-milled material, and grain boundary relaxation was shown in Fig. 4.9(a) to lead to a more relaxed structure at a given grain size than in the as-milled condition. The conventional picture of grain boundary relaxation is that it occurs at temperatures below which grain growth does; the atoms at such highly-energetic grain boundaries are very far from equilibrium, and only a small amount of thermal energy is required for relaxation. However in Bi_2Te_3 we observe measurable grain growth during the relaxation process – from a grain size of 23 nm to 37 nm (Fig. 4.3). This recovery-

dominated grain growth is seen most explicitly during room temperature ageing experiments of Fig. 4.5. As such, it appears that grain growth and GBR are much related processes in Bi_2Te_3 at low temperatures. In the present section we discuss the likely mechanism of low-temperature relaxation-based boundary motion.

Table 4.1 Reports of grain growth activation energy change from low-T to high-T annealing in mechanically milled nc-systems. Available diffusion data is also provided for comparison.

Material	Proc. route	Transition temperature		grain growth E_a (eV)		Diffusion E_a (eV)	
		K	T/Tm	LT	HT	GB	Self
Fe [95]	MA	773	0.43	125	248	174	252-282
Ni [82]	ED	493	0.29	11	108	115	
Ni-0.21Fe [96]	ED	600	0.34	82	286		252-282
Al [190]	Cryo	723	0.77	79	112	84	124-142
RuAl [88]	MA	1073-1173	0.48	39	214		
Fe_3Si [86]	MA	703-773	0.49	32	279		312
Bi_2Te_3	MA	500	0.58	89	242	unknown	unknown

The low temperature grain growth regime characterized in Fig. 4.10 exhibits an activation of 89 kJ/mol. Similarly, low activation energies have been reported for a number of mechanically milled nc-materials, which are summarized in Table 4.1. For example, in nc-Fe [95] the low temperature activation energy approached values of nc grain boundary diffusivity, and self-diffusion at higher temperatures. A similar change in activation energy was observed in electrodeposited nc-Fe [89]. In nc- Ni a much lower activation energy of 11kJ/mol was reported [82], which is about one tenth the activation energy for grain boundary diffusion. These results could be explained by Ni containing more grain boundary disorder; stored enthalpy measurements from Johnson and co-workers indicate $\Delta H/H_f$=0.25 for Ni at 12 nm [53], but only $\Delta H/H_f$=0.15 for Fe at a finer grain size of 8nm [50]. As well as pure metals, the mechanically milled intermetallic compound Fe_3Si is reported to exhibit a low-T activation energy of only 32kJ/mol in its disordered BCC form and a high temperature region of 289kJ/mol upon forming its ordered $D0_3$ structure [86]. Similarly, low grain growth activation energies have been observed for the intermetallic RuAl [88], a solid solution of Fe-0.21Ni [96], and cryo-milled Al [190] – although in the case of cryo-milling the effect of N contamination could play a role. Anomalously low Ea reports have also been made for Cu [191], and in a cryomilled Al-Mg alloy [192].

We suggest that the low E_a region exhibited by Bi_2Te_3 is due to a reordering process within the grain boundary. Support for this thesis comes from the stored enthalpy measurements discussed in the previous section. The lower activation energy for grain growth would be expected from a disordered,

due to the relative ease of atomic re-shuffling in these highly strained regions. As a result, very little thermal energy would be required for re-arrangement.

Correspondingly, the high E_a region can be attributed to some sort of grain boundary diffusion process, in accordance with most theories of grain growth. It is difficult to attribute the high temperature activation energy to any particular mechanism of diffusion, since the self-diffusion and grain boundary activation energies for Bi_2Te_3 have not yet been measured. The self-diffusion activation energy of Se in Bi_2Se_3 – which is an isomorphous compound of similar melting point – was measured to be 209 kJ/mol [193]. Since Te has a larger ionic radius than Se the self-diffusion activation energy for Bi_2Te_3 could reasonably be higher than this, although direct measurements of the Bi_2Te_3 system are needed.

4.4.3 Kinetics of grain growth

The best-fit grain growth exponent in this study was n=6.5, which is much larger than the ideal value of n=2 as proposed by Burke and Turnbull. Similarly high grain growth exponents have been observed for a number of nc-systems [79]. We attribute the large n primarily to the transition in rate-dominating processes that will occur during an isothermal anneal. In reality, whether recovery dominated growth or diffusion dominated growth is dominant, will depend on both the grain size and the temperature. As such, we envisage that the measured n is a composite of relatively fast relaxation-based grain growth kinetics at small grain sizes, followed by a much slower grain growth regime at larger grain sizes. Such a transition can be rationalized by considering the driving forces for grain growth and grain boundary relaxation. The former is proportional to the grain boundary area, and thus scales with the $1/d^2$, while the latter is derived from grain boundary volume and thus scales with $1/d^3$. Therefore during an isothermal treatment, a transition from a relatively low activation energy process to a higher activation energy process would reasonably result in a progressive slowing of the grain growth kinetics at larger grain sizes, and thus a larger grain growth exponent.

As well as a progressive change in the rate limiting process of grain growth, there is a drastic change in the driving force for grain growth. In Eq. 4.5, we estimated that the grain boundaries in their full relaxed state could therefore only account for about 30% of the stored enthalpy. As a result, the driving force for grain growth when normalized by the boundary area falls during grain growth. This progressive lowering of the driving force could lead to higher values of n than suggested by the analysis of Burke and Turnbull, who assumed a constant driving force. Natter et al. [89] proposed a temperature dependent initial grain size, which resulted in a much better fit to experimental data on nc-Fe samples. To investigate this idea further, we consider how the change in driving force during grain growth will affect the kinetics. In deriving the parabolic kinetic equation, Burke and Turnbull [194] assumed a constant grain boundary energy, γ, and thus a linear relation between boundary

velocity and inverse grain size. However if the driving force varies as a function grain size, this assumption will not hold. To account for this non-linearity, we introduce a driving force exponent, m:

$$E = c/d^m \quad [4.6]$$

Thus the rate of boundary migration and the corresponding grain size evolution will vary according to:

$$dd/dt = C\gamma/d^m \quad [4.7]$$

$$d^{m+1} - {d_0}^{m+1} = k(T)t \quad [4.8]$$

where the grain growth exponent, n, has been replaced by the driving force exponent, m+1. We note that if the driving force is linearly with inverse grain size, i.e. m=1, then m+1=2, and parabolic kinetics are predicted. Fig. 4.14 shows a plot of inverse grain size vs stored enthalpy from the data in Fig. 4.12. The relationship can be best fitted with a driving force exponent of m=2.4, which is in excellent agreement with the power-law relationship between microstrain and grain size, with an exponent of 2.5, as shown in Fig. 4.9(a). For comparison, a driving force exponent of m=5.5 is shown, which would correspond to n=6.5. This analysis suggests that while a variable driving force predicts an artificially large n, the enlargement cannot necessarily account for the observed value of n=6.5 in this study. It is possible that a non-linear relationship between driving force and boundary velocity exists for the compound Bi_2Te_3.

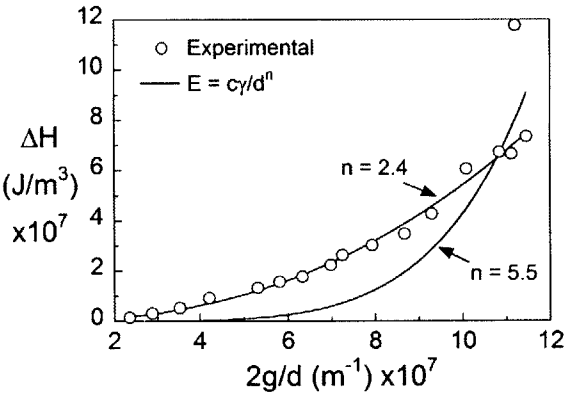

Fig. 4.14 the driving force for grain growth as a function of inverse grain size. The dataset is fitted using a parabolic relationship, yielding an exponent 2.4. By comparison, the line for an exponent of 5.5 is compared – which would yield a grain growth exponent of 6.5, as indicated by Eqs. [4.6-4.8].

4.4.4 Thermal budget map

The engineering motivation of this study was to inform nc-Bi_2Te_3 consolidation strategies, and device operation limitations, with microstructural guidelines – in other words to allow microstructural prediction based on a given thermal history. To meet this goal, in this section we present a visual

thermal budget map that allows a direct comparison of commonly used thermal conditions, with the grain growth constants that were determined in this study. In order to construct the map, the high temperature grain growth constants that were quantified via the straight line fit to the high temperature region of Fig. 4.7 are extrapolated to higher temperatures. The extrapolated grain growth law is displayed as a series of contours, representing regular grain size intervals, where the time/temperature path is defined by solving Eq. 4.1. The contours are indications of what the expected grain size and microstrain will be under a given isothermal history. For example, the map predicts that from a 23 nm starting grain size, a 2 hour anneal at a temperature of 500 °C would result in a grain size of about 1 μm.

The thermal history of expected processing steps and device operation conditions are overlaid in Fig 4.15. Two regions are shown; firstly the "TEG devices" box corresponds to the operational lifetimes of TEG devices that are expected to withstand temperatures up to 230 °C, with operational lifetimes of tens of years. Secondly the "powder consolidation" box corresponds to typical sintering techniques used to consolidate bulk materials, which are at temperatures of 450-500 °C, for times ranging from a few minutes (in the case of Spark-Plasma Sintering) to a few hours (in the case of furnace sintering). By comparing the different grain size contours that intersect these two boxes, we see that for typical powder consolidation routes, device operation is not expected to cause degradation in the properties. I.e. these materials – if consolidated at high temperature – will be stable for very long timescales. Interestingly, if we want to consolidate materials with grain sizes on the order of 100 nm, the consolidation time must be on the order of a second or less. Such rapid consolidation processes are possible with techniques such as shock-wave consolidation, however these processes are difficult to control precisely with a timed short thermal excursion. This suggests that in order to consolidate a truly nanocrystalline material, efforts to engineer more thermally stable grain boundary structures must be made, by using the addition of second phases, or by employing thermodynamic stabilization techniques.

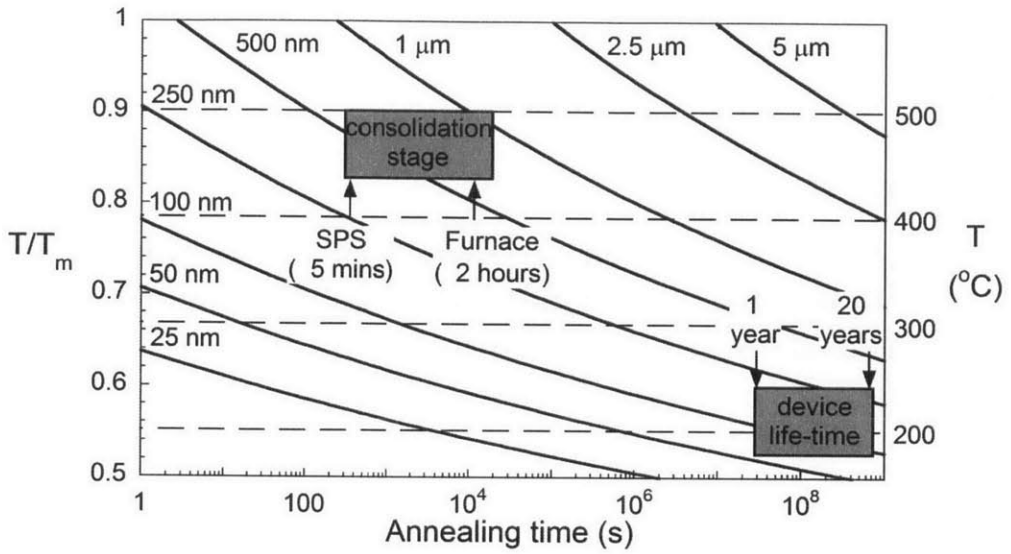

Fig. 4.15 A "thermal budget map" showing the extrapolation of the generalized grain growth law (Eq. 4.1) fitted to high temperature data, as a function of time and temperature. Overlaid on the map are typical sintering conditions, as well as expected conditions for TE generator device operation.

4.5 Conclusions

In this chapter we show that grain growth in the nanocrystalline compound Bi_2Te_3 occurs according to two regimes. At low temperatures, grain growth is controlled by defect annihilation processes, followed by a high temperature regime that is controlled by long-range diffusion.

By studying the structural evolution via a comprehensive range of techniques, the low temperature was shown to remove the majority of stored enthalpy in the material, despite minimal grain growth. Chemical reordering of the lattice was shown to be dominant at the lowest temperatures, with significant recovery occurring even at room temperature, while the remaining lattice strains that characterise the low temperature region can be attributed to non-equilibrium grain boundary structure. By analysing the grain size evolution via a generalized parabolic grain growth law, a relatively high grain growth exponent of 6.5 is measured. The deviation from the conventional exponent of 2 can be attributed to the non-linear variation in stored enthalpy with grain boundary area.

In engineering terms, the quantification of the grain growth constants – which to our knowledge are the first for nanocrystalline thermoelectric material – set markers for the development of nanocrystalline thermoelectrics. Furthermore, the thermal budget developed here suggests that in order to consolidate bulk nanocrystalline structures, steps to engineer advanced thermal stability by employing kinetic inhibitors or thermodynamically lowered grain boundary energies.

Chapter 5: Solid state foaming

5.1 Introduction

In addition to grain growth that was treated in chapter 4, telluride compounds are unstable with respect to significant porosity evolution during thermal annealing. This process is apparently accelerated when materials are processed via non-equilibrium means. Better understanding of porosity evolution is required in order to guide sintering operations, where components are subjected to extreme thermal excursions. In addition, due to the relatively high temperatures experienced at the hot-side of a thermoelectric module, and long expected component lifetimes, pores could also evolve during service. Porosity can also lead component shape change and induced mechanical stresses or cracking. This will degrade thermoelectric efficiency or even cause device failure. Despite a number of anomalous reports of the phenomenon in telluride-based thermoelectric materials [71,72,107–109], to our knowledge, no systematic study of the foaming process induced by intermetallic decomposition has been made.

In this chapter we report the porosity evolution of bulk nanocrystalline samples of Bi_2Te_3 after the powders have been consolidated by cold-pressing. Thermomechanical properties are measured using a dilatometer up to a temperature of 550 °C. Close attention is paid to the kinetics of porosity evolution, which is related to the evolution of deformation induced defects and non-equilibrium phase separation of the compound. The quantitative understanding developed makes it possible to predict the evolved porosity as a function of temperature, and thus provide safe operating bounds for service life of TEGs and other thermoelectric devices containing bismuth telluride.

5.2 Experimental methods

Nanocrystalline Bi_2Te_3 powders were fabricated by mechanical alloying according to the methods discussed in chapter 2 and 3. Milling media of 1.5 g were employed, at a milling frequency of 1060 rpm for 4 hours. Fig. 5.1(a) shows a transmission electron microscopy image (taken using a JEOL 2010 high resolution transmission electron microscope in bright field imagine mode) of the powders after mechanical alloying, indicating an average grain size of about 30 nm.

Powder compacts were made by cold pressing approximately 0.76±0.01 g of resulting powders in a uniaxial die press, operated inside the glovebox. Compacts were compressed in a tool steel die of 6 mm bore diameter, under a pressure of 750±20 MPa, to a relative density $D=\rho/\rho^*=0.905\pm0.005$ (where ρ^* is the specific gravity of Bi_2Te_3, taken to be 7.86 g/cc [16]. Figure 5.1(b) shows a scanning

electron microscopy image (taken using a JSM-6610 SEM in secondary electron imaging mode) of a compact cross-section, illustrating a high density in the as-pressed compact.

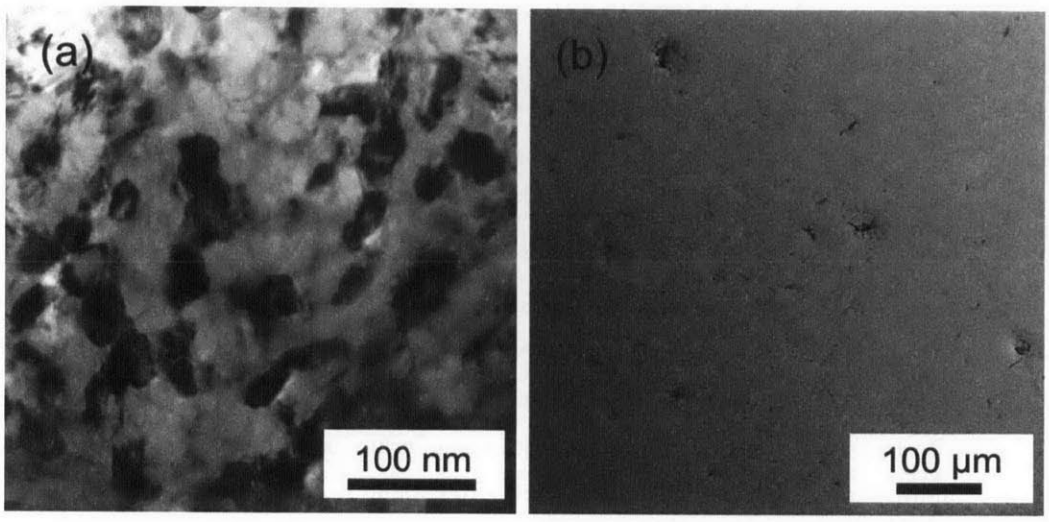

Fig. 5.1 Mechanically alloyed Bi2Te3 observed by (a) transmission electron microscopy of the powders, showing nanocrystalline grain size of approximately 30nm in diameter, and (b) scanning electron microscopy, after cold-pressing of the powders into a pellet, showing a relative density of D=0.9.

Differential scanning calorimetry (DSC) and thermogravimetric analysis (TGA) experiments were performed on the as-pressed compacts using a Mettler Toledo DSC/TGA 1 operated with a purge gas of high purity argon. Thermomechanical analysis (TMA) was performed in a Netzsch 402 F3 dilatometer, operated with a purge gas mixture of 3% H and remainder Ar. Each compact was heated under constant, very low uniaxial stress (900 Pa) at a constant heating rate to the indicated set-point, followed by air cooling. The temperature was monitored using an S-type thermocouple, which was calibrated over the temperature range by monitoring the melting transitions of 6 metallic standards (In, Sn, Bi, Pb, Zn, and Al). Thermal lag between sensor and sample was also accounted for by repeating the calibration at various heating rates [195]. In all samples the expansion normal to the compact-press loading direction was slightly greater than in the radial direction. Volumetric expansion was inferred from length changes measured by TMA under an assumption that the aspect ratio changed linearly with density change. Finally, to calculate the instantaneous porosity, thermal expansion of both instrument and sample was corrected for. Instrumental expansion was measured by running a "blank curve" using an Al_2O_3 reference sample for each heating rate used, whilst sample expansion was modelled by assuming a constant value of thermal expansion coefficient for Bi_2Te_3 (taken to be $17x10^{-6}$/K [196]).

After TMA, compact density was determined using a digital micrometer and microbalance, with respective accuracies of ±5 µm and ±10 µg. Resulting porosity readings were compared with

metallographic examination, by preparing cross sections using SiC paper 1200-4000 followed by polishing with Colloidal Silica suspension (0.05μm). A measure of the pore connectivity was made by making a comparative density measurement using the Archimedes method, after grinding one side of the compact to expose the pores. The compacts were immersed in a beaker of water which was subsequently evacuated by a roughing pump for 1 hour to ensure complete infiltration of water into the pores connected to any free surfaces.

5.3 Analysis of structure and phases present

As suggested in the introduction, the foaming behavior of Bi_2Te_3 is governed principally by the microstructure of the sample, and hence a preliminary discussion of the expected phases – and how they differ in the case of mechanically milled samples – is crucial for interpretation of our results. As a first point to facilitate later understanding of non-equilibrium alloys, we consider firstly samples made by solidification from a stoichiometric melt. According to the equilibrium phase diagram in Fig. 5.2a [197], the first material to crystallize is Bi-rich with a composition of about 40.065% due to a tendency for the compound to form Bi_{Te} antisite defects [16]. As a result the material will be intrinsically p-type. However if Te-rich samples are made by forming an over-pressure the sample will be n-type due to Te_{Bi} antisites. Fig. 5.2(a) indicates the change in dominant carrier either side of the Bi_2Te_3 stoichiometry.

In mechanically milled Bi_2Te_3 however the equilibrium phase diagram does not apply; materials prepared at stoichiometric compositions phase separate despite being nominally within the single-phase region of the line-compound. This phenomenon can be explained as follows: During severe plastic deformation an excess of point defects in the form of anti-sites are produced. Point defect production can be tracked by deviations in lattice parameters from the equilibrium values with decreasing grain size (chapter 3). (ii) when material is subsequently annealed, these defects react to produce an excess of Tellurium vacancies, as proposed by Navratil and co-workers [155]:

$$2V'_{Bi} + 3V^{o}_{Te} + Bi'_{Te} \rightarrow V'_{Bi} + Bi^{x}_{Bi} + 4V^{o}_{Te} + 3e'$$

These excess V^{o}_{Te} results in strongly n-type behavior [43] even in p-type alloy chemistries. This concept can be visualized in the schematic phase diagram in Fig. 5.2(b), where the Bi_2Te_3 line compound is shifted to the Bi-rich side. What this defect reaction means is that in the deformed state, the forced line compound is constitutionally supersaturated with Te, resulting in precipitation of a Te-rich phase during annealing. As a result, when Bi_2Te_3-based compounds are prepared via MA, usually a strong Te-rich eutectic phase signature is observed in a DSC trace [36,198,199]. Indeed we observe the same eutectic melting peak in the DSC here, which is shown in Fig. 5.2(c). The DSC signal shows

an exothermic transition beginning at about 410 °C, corresponding to the eutectic phase transformation (Te + $Bi_2Te_3 \rightarrow$ L) at 413 °C [200]. The total heat release is 2.1±0.5 J/g, which is equivalent to 3 % of Te in the Te-rich phase, and 97 % in the Bi_2Te_3-rich phase (based on an enthalpy of fusion for Te of 17.4 kJ/mol [201]).

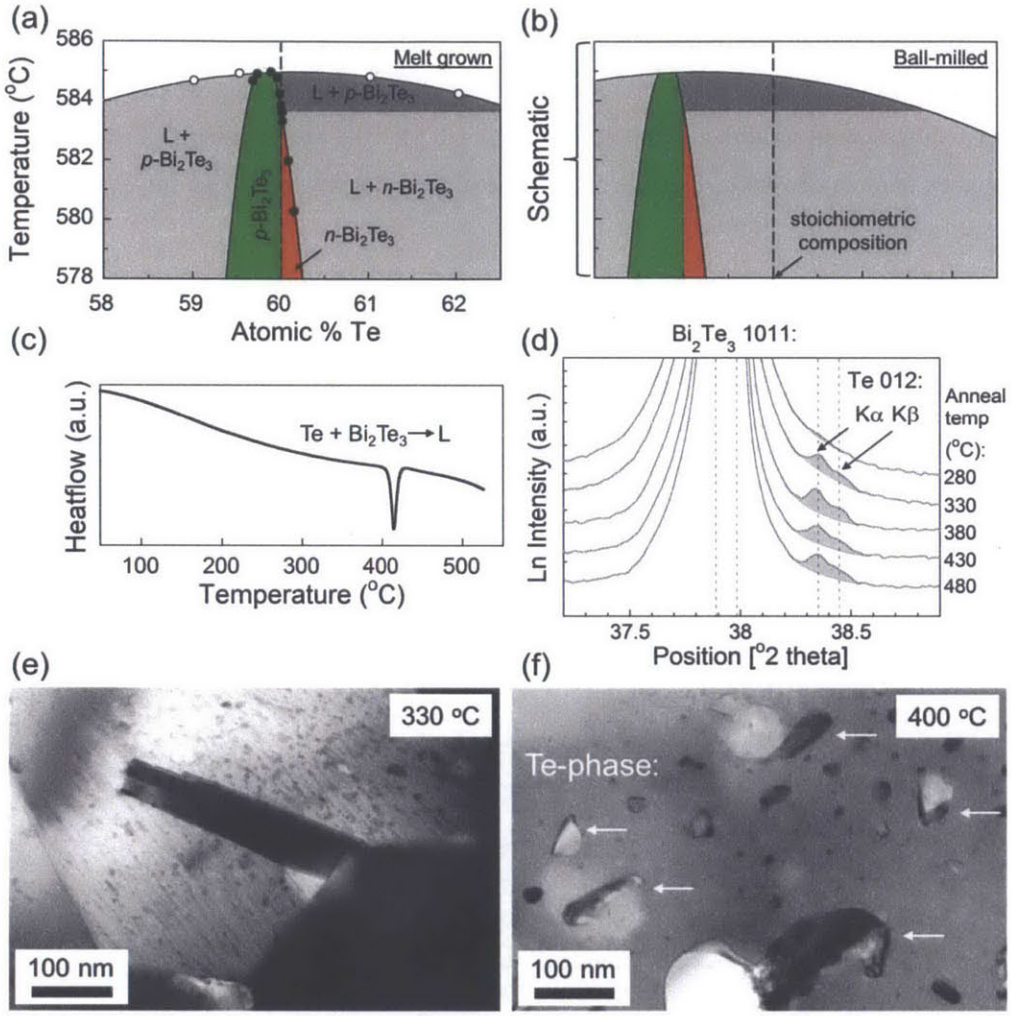

Fig. 5.2 (a) Phase diagram of the Bi-Te phase according to Satterthwaite and Ure [197], showing that at stoichiometric compositions, a single phase is predicted. (b) A schematic phase diagram based after plastic deformation, whereby the line compound is shifted to Bi-rich compositions, resulting in a two phase region at the Bi2Te3 stoichiometry. This phase separation is observed in the Te-rich peaks that emerge in XRD linescans of samples annealed at successively higher temperatures (c), via eutectic melting peak in DSC (d) and by TEM micrographs (e), and (f) taken after annealing at 330, and 400 °C respectively for 2 hours.

Observations of precipitates of the Te-rich phase below the eutectic temperature are shown in the TEM micrographs of Fig. 5.2(d), (e) and (f), which were taken of samples held isothermally for 2 hours at 260, 330 and 400 °C respectively. The size of precipitates increases with increasing annealing temperature due to coarsening.

5.4 Results

Figure 5.3(a) illustrates the average porosity, labelled P and calculated as P = 1 – D, as a function of annealing temperature for a compact heated to 550 °C at a rate of 3 K/min. The onset of significant porosity change occurs at approximately 350 °C, which is followed by a sharp transient to a peak rate of porosity evolution at approximately 408 °C. This is about the same temperature as the eutectic melting peak, which is shown in Fig. 5.3(b) for comparison. Upon further heating, P increases at a markedly slower rate toward a final porosity P_f = 0.51. The measurement of P_f from TMA is supported by manual density measurement and optical stereology, which yield values of P_f = 0.48 and 0.52 respectively.

The mass flow via TGA for a nominally identical sample to that in Fig. 5.3(a) is shown in Figure 5.3(b) alongside the DSC signature, which is acquired under the same heating conditions as above. The TGA curve shows a monotonic mass loss, beginning at approximately 400 °C, resulting in a cumulative mass change of 1.04 % that can be attributed solely to evaporation of Te, since the vapor pressure of Te is approximately 10^3 times that of Bi at these temperatures [202].

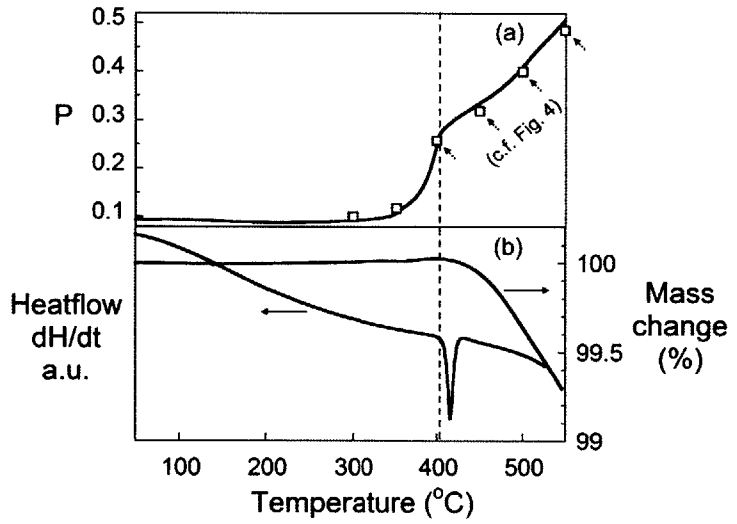

Fig. 5.3 (a) Porosity evolution at a heating rate of 3 K/min along with (b) heatflow by differential scanning calorimetry and mass loss by thermogravimetric analysis. At the eutectic point, Te + Bi_2Te_3 → L, as shown by a peak in the heatflow signal, there is a corresponding slowing in the rate of porosity increase, whilst simultaneously the onset of mass loss begins.

The evolution in pore structure is depicted in Fig. 5.4, by optical micrographs taken after heating compacts at 3 K/min to various temperatures. The final porosities for compacts annealed at 400, 450, 500, and 550 °C are P=0.26, 0.32, 0.40, and 0.48 respectively – as measured by macroscopic density measurements. These density measurements agree with stereoscopic densities to within ±0.05 porosity. Initially, a mixture of isolated micro-scale and larger pores grow – with the largest pores

approximately 50-100 μm in diameter. At higher temperatures, pores begin to impinge upon one another, and the images in Fig. 5.4 suggest coalescence into larger connected structures.

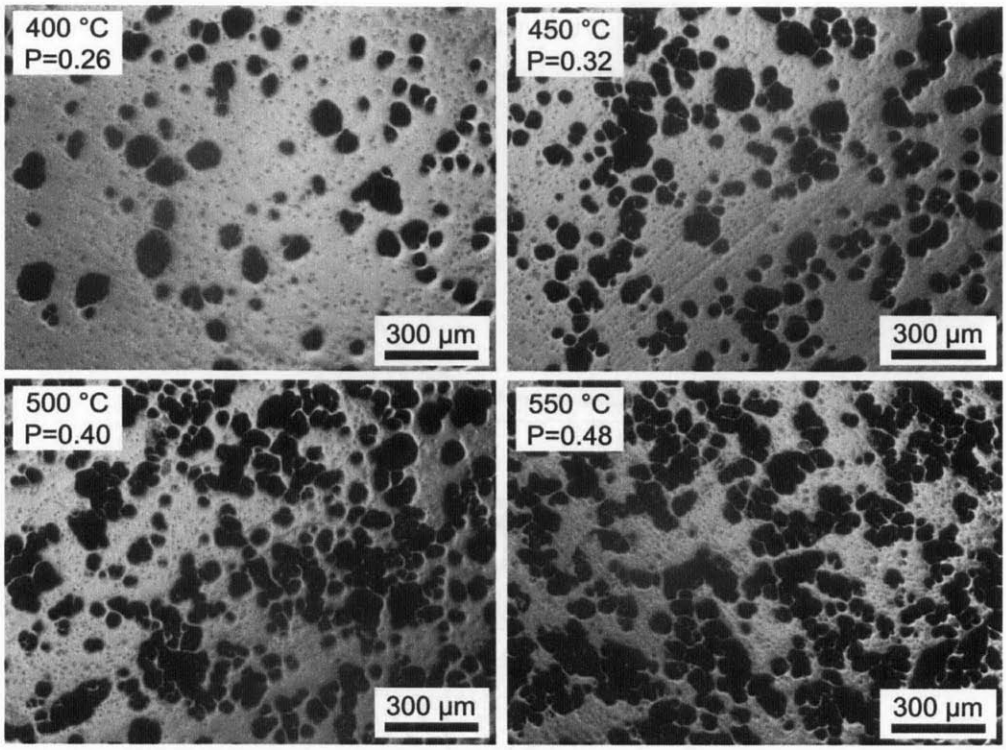

Fig. 5.4 Optical micrographs of cross-sections taken from compacts heated to various temperatures, showing the evolution in pore volume fraction and morphology.

Faster heating rates lead to lower final porosity, as represented in Fig. 5.5(a). This is evidenced by macroscopic porosities of P=0.40, 0.40, 0.38, and 0.37 for samples heated at 1, 3, 10, and 30K/min respectively to 500 °C. This is due to delayed onset of porosity at higher heating rates – visualized more clearly in Fig. 5.5(b) – which shows the rate of change in porosity, (dP/dt), normalized by the heating rate. The two peaks in (dP/dt) correspond firstly to the onset of foaming – hereafter referred to as the "onset-peak" – and secondly to the maximum at the eutectic temperature – hereafter referred to as the "eutectic-peak". The derivative curve clearly shows that the onset-peak is strongly dependent on heating rate, whereas the eutectic-peak occurs isothermally at an average temperature of 408 °C, irrespective of heating rate.

The effective activation energy for the foaming process corresponding to the onset-peak can be extracted using a Kissinger analysis [ref]:

$$\beta/T_c^{\,2} = \exp(Q/RT_c) \qquad [5.1]$$

where β and T_c are the heating rate and temperature of the onset-peak respectively. Fig. 5.6 plots β/T_c^2 against $1/T$ for the onset-peak and eutectic-peak in foaming rate in Fig. 5.5. The gradient of the line of best fit reveals an activation energy of 270 kJ/mol for the process corresponding to the onset-peak. The eutectic-peak is not amenable to a Kissinger analysis because there was no measureable temperature shift.

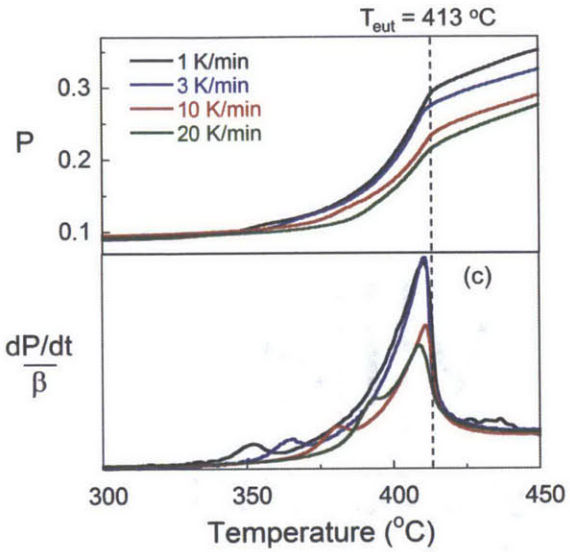

Fig. 5.5 Above: Porosity evolution curves for various heating rates between 1 and 20 K/min, showing increasing porosity with decreasing heating rate. Below: Derivative of the porosity curve showing a shift in the onset of porosity with heating rate, indicating that the porosity onset is controlled by diffusion. By contrast, the maximum in rate of porosity increase occurs isothermally at the eutectic temperature of 410 °C (as measured by DSC) regardless of the heating rate.

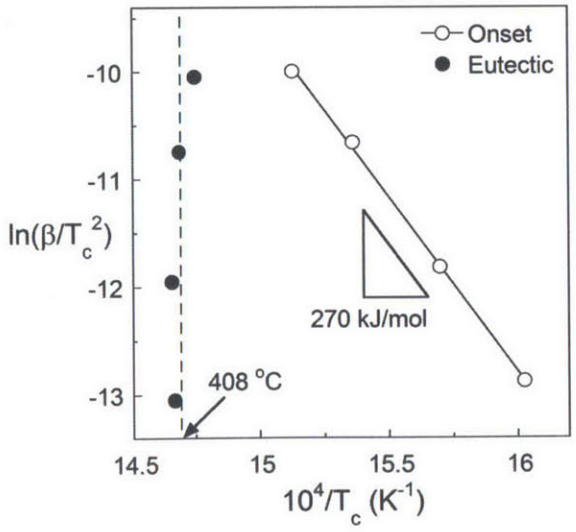

Fig. 5.6 A Kissinger plot of the peak temperature in foaming rate from Fig. 5.5 show that the onset-peak has an activation energy of 270 kJ/mol, whilst the eutectic-peak occurs isothermally at 408 °C.

The pore connectivity can be determined by comparing the micrometer-measured total porosity, P, with the Archimedes method which is a measure of closed porosity, P_{closed}. Fig 5.7 plots these two quantities on the primary y-axis, while the secondary y-axis plots the fraction of open porosity, $f_{open}=(P- P_{closed})/P$, as a function of maximum compact annealing temperature. A value of $f_{open}=0$ corresponds to completely closed pores, i.e. zero water infiltration occurs after compact immersion, while a value of $f_{open}=1$ corresponds to completely open pores, i.e. they are completely infiltrated by water after immersion. The open porosity fraction starts at approximately $f_{open}=0.6$ at 300 °C and falls to about $f_{open}=0.1$ at 400 °C where it remains up to the highest annealing temperature. The low f_{open} value at high temperatures confirms that the evolved pore walls are closed.

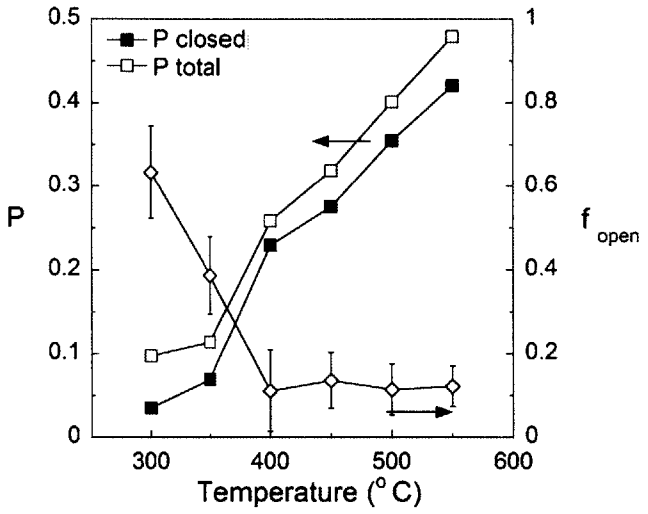

Fig. 5.7 The relative density of the compacts, as measured via the Archimedes method (open symbols) and in air (closed symbols) can reveal the connectivity of the pores. The resulting infiltration parameter remains relatively low for all samples above 400 °C, indicating that pores are not connected.

To further clarify the pore structure, Fig. 5.8 shows an optical micrograph (a) alongside an SEM micrograph taken at higher magnification (b) of the same region of the 550 °C compact cross section. Due to the much greater depth of view in the SEM, the structure of the pore wall can be seen. A hierarchical morphology is revealed where each pore is comprised of many smaller ones.

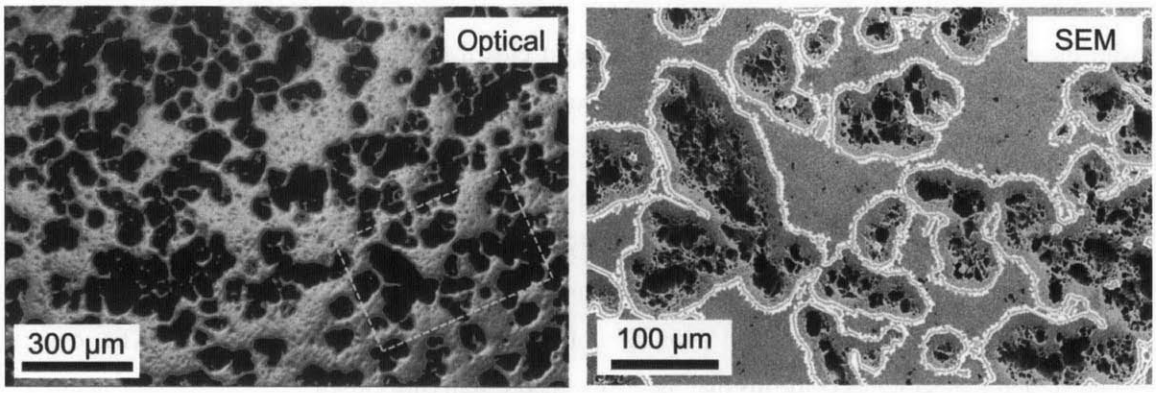

Fig. 5.8 An SEM image of a cross section of a compact heated to 550 °C reveals a hierarchical pore structure, where the large pores shown in Fig. 4 consist of many smaller pores that group together.

Pores nucleate primarily on precipitates, as shown by the TEM micrograph in Fig. 9 for a compact annealed at 400 °C for 2 hours, with a final porosity of P=0.29. The micrograph shows that all the pores present are abutted by precipitates – seen as regions of light and dark contrast respectively.

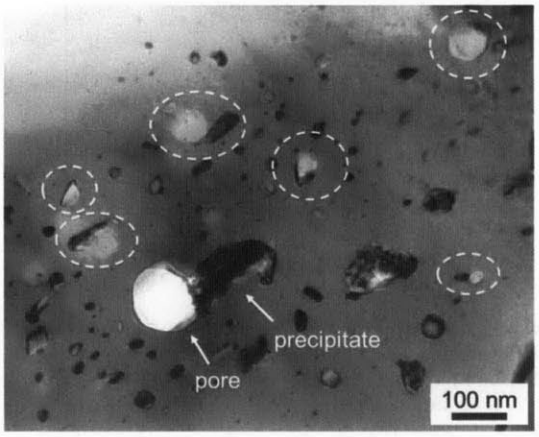

Fig. 5.9 A TEM image of a cross section of a compact heated to 400 °C reveals tendency of pores to nucleate on precipitates.

5.5 Discussion

A quantitative analysis of the porosity evolution is difficult for two reasons. Firstly, the lack of high quality diffusion and creep data for Bi_2Te_3 – which are usually required for modelling pore growth – presents a challenge. The second difficulty is that due to the highly non-equilibrium nature of the starting material – recovery, grain growth, phase separation, and eutectic melting occur simultaneously during annealing, making it difficult to compare experimental data to theory. Therefore in the following discussion, our analysis is mainly qualitative, employing only a semi-quantitative analysis in considering the relative importance of specific phenomena.

5.5.1 Driving force for pore growth:

Foaming of Bi_2Te_3 is broadly driven via decomposition of the intermetallic into Bi_2Te_3 and a Te-rich eutectic at high temperatures. However an explicit understanding of the origins of stress that forces deformation around a growing pore, remain unclear. Certainly the abnormally high vapor pressure of Te [203] provides some driving force, however it also possible that residual trapped gas coming out of solution could play a role.

Regardless of the origins of the internal stress, it is true that in order for a pore to grow, the stress must exceed the interfacial stress that results from the increase in surface area. A simple force balance gives the required internal pressure to prevent the pore from sintering:

$$p = \frac{2\gamma}{r} \qquad [5.2]$$

where r is the pore radius and γ is the surface energy. For Te, γ=0.36J/m^2 [204], and from Fig. 5.4 the approximate pore radius is 50 um, which gives a required internal pore pressure of about p=10kPa. In the following discussion we consider the possible origins of stress.

Tellurium vapor pressure

One driving force for foaming can be attributed to the decomposition of Bi_2Te into a Te-rich eutectic phase at elevated temperatures, resulting in large vapor pressure above the Te-rich phase. Evidence for the phase separation process is given in Fig. 5.2, while Figs. 5.5 and 5.6 show that the peak foaming rate coincides with the eutectic transformation. To investigate the role of Te content further, non-stoichiometric compacts were prepared in the range 58 at. % Te to 62 at. % Te. The resulting porosity evolution is reported in Fig. 5.10. The results confirm the role of the Te phase in driving porosity, in that the Te-poor samples (58 and 59) display improved resistance to porosity; until temperatures above 500 °C. These samples are prepared within the Bi_2Te_3+BiTe phase field, and therefore the Te-rich eutectic phase is not present. The vapor pressure above these phases is much lower than above Te-rich liquid. By contrast the Te-rich samples (61, and 62) show much enhanced rates, reaching final porosities of 0.55 and 0.62, as compared to 0.48 at stoichiometric compositions.

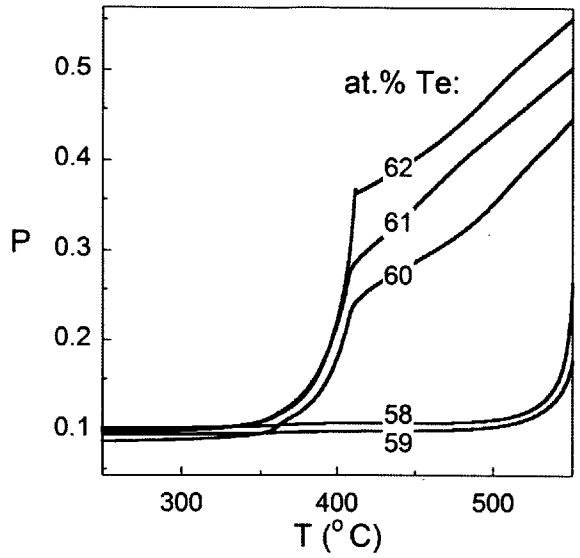

Fig. 5.10 Porosity evolution at non-stoichiometric compositions. When the compound is forced to the Bi-rich compositions (x=0.58, 0.59), porosity formation is suppressed, due to the absence of Te-rich eutectic. At Te-rich compositions (x=0.61, 0.62), porosity formation is further enhanced due to excess Te phase.

Te has an abnormally large vapor pressure above it, and as such has been observed to cause bubble formation in Bi_2Te_3 that is solidified from the melt [205]. The vapor pressure of Te over the solid Te and Bi_2Te_3 has been measured by Brebrick using optical density measurements [203]. Fig. 5.11 shows a plot of the vapor pressure above liquid and solid Te between 360 and 510 °C. The equilibrium vapor pressure of Te over the liquid and the solid are the given by the equations:

$$\log {P_0}^{sol}(\text{atm}) = -8.001 \times 10^3/T + 7.540 \quad [5.3]$$

$$\log {P_0}^{liq}(\text{atm}) = -5.9602 \times 10^3/T + 4.7192 \quad [5.4]$$

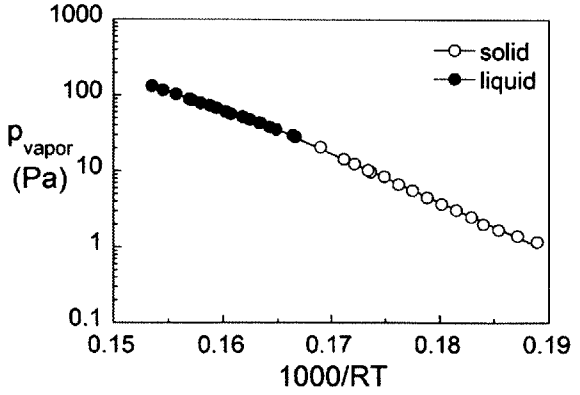

Fig. 5.11 Vapor pressure above pure Te as a function of temperature.

The vapour pressure above the liquid Te phase given by Eq. 5.4 – which is on the order of 10-100Pa – is thus relatively small compared to our estimation from Eq. 5.2 of 10 kPa. However in the beginnings of phase separation, the precipitate size will be very small, which will incur an increase in vapor pressure due to interface curvature. The non-equilibrium vapor pressure, P_0^k for a solid or liquid with radius of curvature, r, is given by the kelvin equation [206]:

$$P_0{}^r = P_0 \cdot \exp\left(\frac{2\gamma V_m}{RTr}\right) \qquad [5.5]$$

where P_0 is the vapor pressure over a flat surface, γ is the surface energy, V_m is the molar volume, T is the temperature and R is the molar gas constant. Fig. 5.12 shows the vapor pressure of above the Te phase a function of diameter of Te precipitate for a series of temperatures between 400 °C and 500 °C. Overlaid on the plot is the vapor pressure estimate from Eq. 5.4 which intersects the modified vapour pressure curves at a precipitate size of about 1 nm.

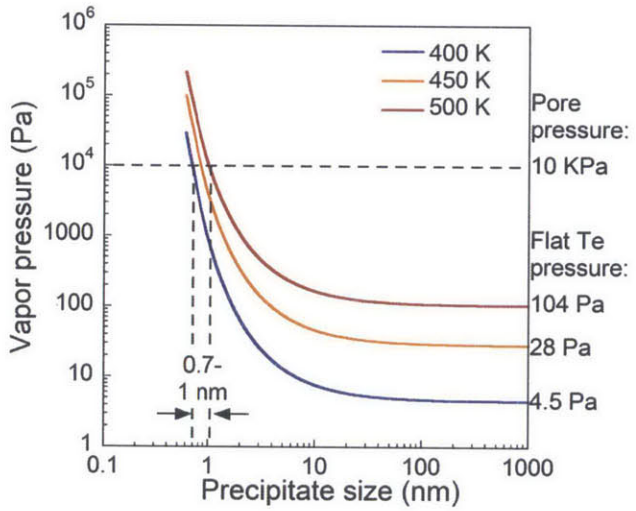

Fig. 5.12 Vapor pressure above Te as a function of precipitate size. Based on the estimated internal pressure pore pressure from Eq. 5.5, the Te vapor pressure will equilibrate with the pore pressure at a precipitate size on the order of 1 nm.

Trapped gas

Secondly we consider the possibility of expansion of trapped gas being incorporated into the powders during milling and subsequent cold-pressing. The expansion of trapped gas is a common method of solid-state foaming by annealing of compacts made via Hot Isostatic Pressing of powders in an overpressure of Argon [207]. Expansion of trapped gas has been shown to cause pore expansion in cryo-milled Cu powders [208], and trapped gas is well known to prevent full density from being reached in during the final stages of sintering operations. The possibility of incorporating trapped gas

during MA is unlikely however due to the very low solubility of Argon in metals. Furthermore, flash evaporated films [109] and hand-crushed ingots [107] were also reported to exhibit thermal induced porosity, which do not involve mechanical alloying and therefore trapping of gas during milling is improbable. It could also be argued that a small amount of gas could be trapped between pressed particles during cold pressing. The quantity of gas can be estimated via the relative density of the as-pressed powders, which was about P=0.1, which is relatively small compared to the P=0.48 that was achieved in the case of the sample annealed at 550 °C.

To test the possibility of trapped gases being incorporated via the methods discussed above, two control experiments were performed. The first was to fabricate a compact in vacuum from mechanically alloyed powders, and the second was to compress a compact in Argon from powders that were not mechanically alloyed. The behaviour of these compacts is compared in Fig. 5.13 to the curve taken from Fig. 5.3. The compact pressed in vacuum approximately overlays with the compact pressed in Argon, to within experimental error, confirming that trapped Argon gas from the pressing procedure does not contribute considerably to porosity. The results of Fig. 5.13, along with the discussion above suggest that trapped gas does not play a significant role, although it cannot be eliminated completely.

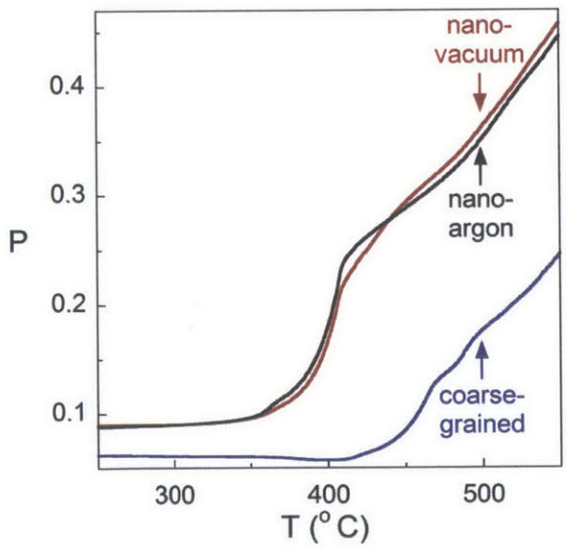

Fig. 5.13 Porosity as a function of temperature for compacts pressed in vacuum, and from commercially obtained powders, compared to the conventional compact pressed in Argon. The vacuum sample overlays, confirming trapped gas plays no role. By comparison, the commercial compact exhibits delayed porosity onset.

5.5.2 Deformation mechanism during pore growth:

With the above understanding of the driving force for grain growth, we now turn to the deformation mechanisms that can accommodate pore growth. Based on the equilibrium pore size, the vapor pressure was estimated to be on the order of 10 kPa. This is equivalent to a normalized shear stress γ/μ, of about 10^{-6}, which is comparatively small compared to typical dislocation creep stresses. It is therefore unlikely that typical dislocation creep can accommodate the flow. It is therefore likely that Bi_2Te_3 deforms via diffusive creep. To estimate transport rates, the grain size at the eutectic point can be estimated by employing the grain growth equation for a scanning experiment [185]:

$$d^n(t) = d^n(0) + k(T)\left(\frac{k_B T^2}{bQ}\right) \quad [5.6]$$

in where d, k_B, and b, are the grain size, Boltzmann's constant and heating rate respectively, and n, k(T), and Q are the grain growth exponent, kinetic constant and activation energy respectively that were measured recently in nc-Bi_2Te_3 (chapter 4). Despite the large shift in transient temperatures, the estimated grain sizes are nearly constant at 171, 168, 164 and 164 nm for heating rates of 1, 3, 10, and 20 K/min respectively. This small grain size is consistent with a grain boundary transport regime.

The grain boundary diffusion can be estimated on the basis of literature trends in grain boundary materials [164]. The diffusivity can be estimated according to the equation:

$$\delta D_{GB} = D_0 \exp(-BT_m/T) \quad [5.7]$$

where δ is the grain boundary width which we assume to be 1 nm, and B is a dimensionless grain boundary diffusion activation energy, $B=Q/RT_m$, which is on average between 10 and 15 for most materials [164] – and here we assume the average value of 12.5. Finally, D_0 is the attempt frequency which is between about 10^{-15} and 10^{-13} for most materials [164] and which we take to be an average of approximately 10^{-14}. As a result, at the eutectic temperature, we estimate the grain boundary diffusivity to be on the order of 10^{-12} m^2/s.

We can now estimate the coble creep rate on the basis of our estimated grain boundary diffusivity using the equation for coble creep [209]:

$$\dot{\varepsilon}_{ss} = \frac{42\pi D_{GB}\sigma\delta\Omega}{kTd^3} \quad [5.8]$$

where Ω is the atomic volume, σ is the applied stress which we take to be the pore pressure, p=10kPa, and d is the grain size. Substituting for the estimated parameters: $D_0=10^{-12}$ m^2/s; T=686 K; D=170 nm yields a strain rate of 10^{-3} s^{-1}. Comparing this to the peak strain rates observed on a global scale in the

compacts – which at its peak are approximately 10^{-5}-10^{-4} s^{-1} – the estimated coble creep stress is adequate to accommodate pore growth.

5.5.3 Porosity evolution:

With an understanding of the likely deformation mechanism that accommodates the growing pore, we are now in a position to analyse the porosity evolution curves that were shown in Fig. 5.3, and in more detail as a function of heating rate in Fig 5.5. We consider the curve into two sections: (i) the leading transient before the eutectic; and (ii) the secondary transient after the eutectic.

Initial transient

The leading transient is notably characterised by a temperature heating rate dependent onset of porosity, which is shown by a shift in the onset in Fig 5.5(a) and by a shift in the primary peak in Fig. 5.5(b). The temperature shift can be attributed to some thermally-activated kinetic process, which we assume to be due to a peak in the rate of creep. This idea is consistent with the magnitude of the activation energy for the initial transient, which – as shown in Fig. 5.6 – was measured to be 270 kJ/mol. In the previous section it was shown that coble creep is the most likely deformation mechanism. Eq. 5.8 showed that the strain rate will vary with the inverse cube of grain size, therefore during grain growth the number of sites available to boundary transport will decrease with temperature, while the diffusivity and vapour pressure will increase. The initial peak in foaming rate – which is observed at all heating rates – can therefore be understood in terms of a trade-off between a reduction in available diffusion sites, and an increase in the boundary diffusivity.

Secondary transient

The decrease in foaming rate that is observed at 408 °C is large and sudden; the rate falls by a factor of 2 in about 10-20 seconds regardless of the heating rate. This is about the same rate as is observed during discontinuous melting of pure metals and therefore likely to be limited by instrument response, and not the sample. We therefore view the shoulder in porosity evolution at 408 °C the result of a an instantaneous change from the melting of Te-rich precipitates, since this temperature is very close to the eutectic temperature that was measured to be 410 °C by DSC in Fig. 5.3. We propose two possible reasons as to why the phase transformation could cause a large drop in the foaming rate:

1) *Vapor pressure drop* – During melting, Te liquid could wet the inside of growing pores, thus invoking a negative surface curvature which would immediately decrease the equilibrium vapor pressure in a discontinuous fashion.
2) *Chemical redistribution* – At the eutectic point, the Te-rich phase would begin to dissolve Bi from the matrix in order to follow the equilibrium solidus line. This would lower its vapor pressure.

5.5.4 Fine grained material stability

The reason for the enhanced foaming in after mechanical alloying can be explained on the basis of both the increased driving force for pore growth and the enhanced kinetics of matter transport as a result of the nanocrystalline state. The increased driving force was explained on the basis of a constitutional supersaturation of Te atoms (section 5.3) as a result of mechanically induced defects. This results in a higher vapour pressure (as discussed in section 5.5.1). In addition, the increased kinetics can be explained on the basis of a large grain boundary area available for diffusive creep. The enhanced porosity is shown explicitly in Fig. 5.11, where a compact made from coarse-grained powders of the same nominal stoichiometry show also shows a significantly delayed onset of porosity. In addition, the final macroscopic porosity was P=0.26 as compared to P=0.48 for the nanocrystalline powder.

Although not enough literature data exists to corroborate the effect of grain size and mechanical deformation on the degree of thermally induced porosity, Table 5.1 summarizes the available literature reports. Not only is Bi_2Te_3 susceptible but also several sulphide and telluride compounds.

Table. 5.1 Literature reports of thermally induced porosity for Telluride compounds.

Chemistry	Preparation method	As-prepared grain size	Max annealing temp. (°C)	Max porosity
$Bi_{1.5}Sb_{0.5}Te_3$ [107]	Crushed and cold press	Not reported	500	0.11
$Bi_{0.5}Sb_{1.5}Te_3$ [107]			500	0.13
PbTe [72]	MM & HP	1-10 μm	450	0.22
$Bi_{1.5}Sb_{0.5}Te_3$ [105]	MM & HP	Not reported	500	Not reported
$Bi_2Se_{0.3}Te_{2.7}$ [108]	Sinter	Not reported	550	0.18
$Bi_2Se_{0.3}Te_{2.7}$ [109]	Flash-evaporation	30 nm	350	Not reported
Bi_2S_3 [210]	MM & SPS	<100 nm	550	0.07
$CuFeS_2$ [106]	MA & SPS	Not reported	650	0.11

5.6 Conclusions

In this chapter we have shown that the foaming of cold-pressed nanocrystalline Bi_2Te_3 results in a spontaneous foaming, which is driven by phase separation of the compound into a Te-rich eutectic. The degree of porosity increases with Te content due to the highly volatile nature of the Te rich phase.

By analysing the equilibrium pore size on the basis of competition between internal pore pressure and surface energy, the internal stress within a pore is estimated. The pore stress is comparatively large compared the equilibrium vapour pressure above the solid Te, however due to the relationship between precipitate curvature and vapour pressure, very fine precipitates of Te can match the pore stress if small enough. Under this internal stress, the resulting deformation around a growing pore can be accommodated via coble creep, and therefore foaming is expected to be enhanced when the initial grain size is small.

Despite the apparent ubiquity of porosity evolution in these materials, this is the only detailed study of the foaming process we are aware of. The results are therefore of great interest for the advancement of processing nanocrystalline thermoelectric materials, which are commonly fabricated via mechanical alloying or other non-equilibrium means. Our results suggest that in order to minimize foaming during powder consolidation, samples should be prepared at compositions that are slightly rich in metallic species. In addition, the mechanistic understanding developed suggests some materials design routes towards the mitigation of foaming. Traditional creep suppressers, such as second phase particles can inhibit high temperature creep and thus present an opportunity to engineer materials with higher dimensional stability.

While the results of this study are most pertinent to Bi_2Te_3 and its solid solutions, the observations have broader implications for the processing of other telluride compounds, and indeed chalcogenide semiconductor compounds such as the sulphides and selenides, which have tend to form line compounds with similarly narrow phase fields, retrograde solubility, and high vapour pressure in the chalcogen rich region of the phase diagram.

Chapter 6: Recrystallization, grain growth, and thermoelectric performance of oxide-dispersed materials

6.1 Introduction

In chapters 4 and 5, the thermal instability of nanocrystalline thermoelectric compounds was explored. It was suggested that to achieve improved thermal stability, materials with enhanced resistance to grain growth and foaming must be developed. An attractive method for improving stability is to employ insoluble inclusions, which act as pinning sites for grain boundaries, and in addition tend to provide enhanced creep strength [119]. Although this strategy could be applicable to nanocrystalline thermoelectric alloys, it has not yet been explored in detail.

The optimization of inclusion additions to thermoelectric materials would rely on deeper microstructural understanding. In order to stabilize a fine grain size, the correct inclusion size, shape, volume fraction and chemistry must be selected. Inclusion engineering must therefore be guided by a quantitative understanding of microstructural evolution in thermoelectric materials. The thermoelectric properties of materials with second phase oxide additions indicates favourable properties [128] could be incurred, however no detailed study of microstructural evolution during heat treatment has been reported.

The effect of second phase particles on recovery and grain growth is now relatively well understood [77]. The static grain size following grain growth can be linearly related to the ratio of inclusion particle size and volume fraction, i.e., D/f, via the Zener relation [120]. The original Zener theory can adequately account for general grain size trends in experiments [211], even down to the nanoscale [123], with departures from linear scaling above volume fractions of about $f = 0.1$, where a non-linear relationship between grain size and D/f is predicted [212].

However, many other annealing-related microstructural phenomena can occur in the presence of particles. For example, when the inclusion size is reduced below a certain critical size – on the order 20 nm – thermally activated unpinning of the grain boundary can become increasingly problematic [213], leading to a grain size much greater than the Zener limit. As well as un-pinning, small particles are also susceptible to being dragged along by the boundary via diffusive mechanisms, if the particle is sufficiently mobile [214]. Under certain conditions inclusions can also promote abnormal grain growth [215]. Finally, due to the enhanced deformation within the region neighbouring an inclusion, particle stimulated nucleation of recrystallization can occur in highly deformed materials [216]. These phenomena could be prevalent in mechanically alloyed and milled materials, which are of great interest to the thermoelectric community. The final grain size will therefore be dictated by the

interplay of many annealing related phenomena, which points to the need for systematic study of inclusion related annealing phenomena in thermoelectric materials.

In this chapter we present a systematic microstructural investigation of a nanocrystalline Bi_2Te_3 with a fine dispersion of inert inclusions. For the inclusion phase, Yttria (Yttrium [III] Oxide) was selected, on the basis of it being a well-studied oxygen scavenger, thus promoting high inclusion stability. Interestingly, at low annealing temperatures particles tend to induce a larger final grain size in comparison to the single phase alloy, while at higher temperatures particles induce a finer grain size. Enhanced stability is maintained – rather encouragingly – to temperatures near the compound melting point. This behaviour is explained in terms of the relative strength of boundary driving pressures operating during the recovery and grain growth process. Finally, the engineering relevance of this study is explored by consolidating thermoelements from the powders and investigating the density evolution and transport properties of these materials are compared to pure Bi_2Te_3. As a result we make several recommendations for selection of inclusions in thermoelectric materials based on Bismuth Telluride.

6.2 Experimental methods

Characterisation and heat treatment

Powders were characterized by x-ray diffraction according to the procedures described in chapter 3. In the analysis of XRD patterns of the two phase materials, the Bi_2Te_3 and Y_2O_3 crystal structures were modelled using literature values for atomic positions [133], and refined for simultaneously. Transmission electron microscopy (TEM) of the as-milled powders was performed using a JEOL 2010 high resolution transmission electron microscope (HRTEM) operated at an accelerating voltage of 200 kV in bright field imaging mode. TEM specimens were prepared according to the method described in chapter 3.

Annealing treatments were performed according to the same procedures as in chapter 4. Differential scanning calorimetry (DSC) experiments were performed on powders using a TA Instruments Q100 DSC operated with a purge gas of nitrogen and a liquid nitrogen cooling system. The instrument was independently calibrated to within ±0.1 °C using an In standard. All specimens were sealed inside an aluminum pan and heated from -50 to 400 °C at 50 K/min. The irreversible stored enthalpy release was obtained by integrating the area under the curve between the linear regions either side of the exothermic region.

Composite synthesis

Nanocrystalline Bi_2Te_3 – Y_2O_3 composites were fabricated by mechanical alloying of elemental powders Bi and Te with pre-oxidized Y_2O_3 nanoparticles. The Bi and Te powders were identical to those used in previous chapters, with maximum particle diameters of 45 and 75 microns respectively, while the Y_2O_3 particles (from Sigma Aldrich) had a mean particle diameter <50 nm. Fig. 6.1(a) shows a representative TEM image of the Y_2O_3 nanoparticles, where a number of 20 nm grains are agglomerated into a larger cluster, typical of the as-received condition. The XRD analysis as shown in Fig. 6.1(b) is consistent with these observations, showing an estimated grain size of 23 nm, a microstrain of 0.21 %, and a cubic body-centered crystal structure with a lattice parameter of a=1.061 nm.

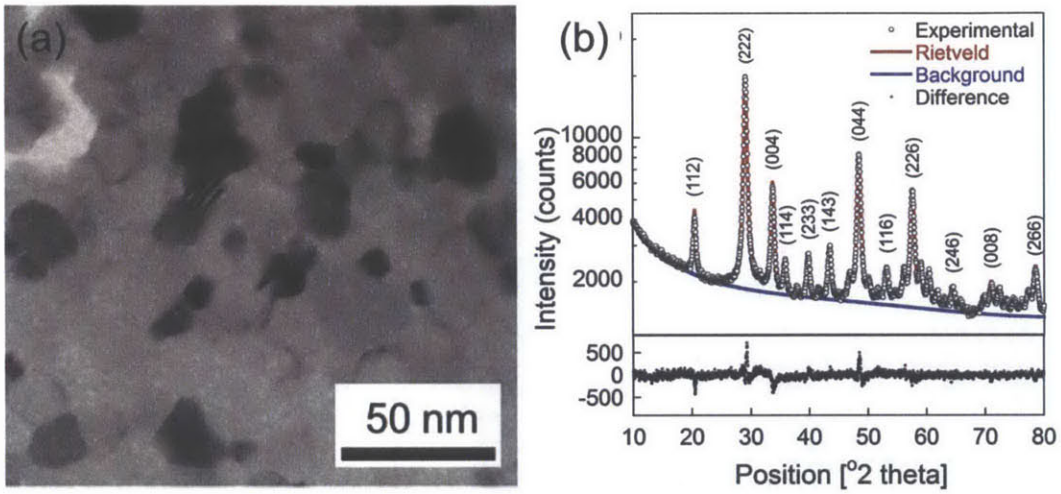

Fig. 6.1 (a) TEM of as-received Y2O3 particles showing a grain size of 20 nm, and (b) XRD pattern of as-received powders indexed to the Y2O3 phase.

The powders were mechanically alloyed according to the procedures described in chapter 2, where it was showed that the alloying process occurs rapidly during the initial stages of milling, with continued treatment resulting in a minimum grain size after a specific mechanical energy dose of 32 kJ/g (see chapter 3). Hence, we employed this energy dose consistently to fabricate all samples in this study, which was achieved using a ball-to-powder weight ratio of 5:1 using milling media of 1.5 g, at a milling frequency of 1060 rpm for 4 hours.

Composites ranging from 0.5 wt. % to 15 wt. % Y_2O_3 were fabricated. We hereafter refer to these samples as 0.5Y, 2Y, 5Y, 10Y and 15Y, corresponding to the relevant wt. % Y_2O_3 added. Mechanical alloying of the composites occurred in a similar fashion to pure Bi_2Te_3, with the final as-milled microstructure varying little with additions of Y_2O_3. In particular, for all samples the mean grain size was estimated to be 31± 2 nm, with a microstrain of 0.37 ± 0.03 %, and lattice parameters of a =

0.4386 ± 0.0001 nm and c = 3.044 ± 0.002 nm, and can thus be considered comparable for the purposes of analysis in this study.

During MA, the Y_2O_3 phase is not deformed significantly, due to its high hardness; the estimated structural parameters of the Y_2O_3 phase via XRD remain unchanged before and after MA. The Y_2O_3 particles were generally found to be dispersed evenly, however some agglomerated particles remained. To determine the particle size distribution of the dispersion, some milled composite powders were annealed at 400 °C for 2 hours and imaged via TEM. Fig. 6.2(a) shows a bright field TEM image of the powders after annealing, revealing a bi-modal particle size distribution, consisting of very fine single crystal particles with an average diameter of 20 nm, interspersed with large polycrystalline aggregates of about 65 nm in diameter. Fig. 6.2(b) shows a particle size histogram – taken from over 400 particle tracings – indicating a volume averaged spherical equivalent particle diameter of 32 nm.

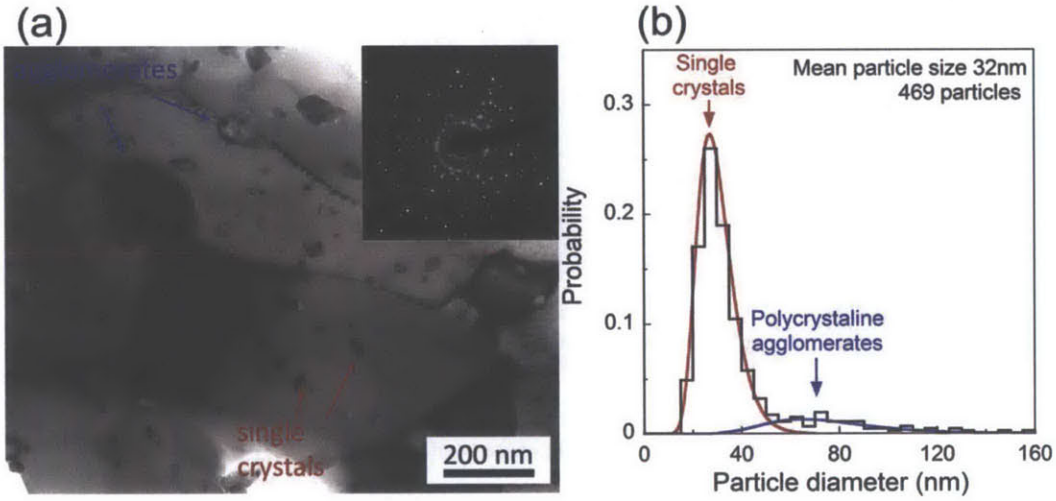

Fig. 6.2 Size analysis of the Y_2O_3 particle dispersion showing (a) a representative TEM image of milled and heat treated composite showing a bimodal distribution of particles, with (b) a particle size histogram showing an average particle size of 32 nm

6.3 Results

Fig. 6.3 shows the evolution in XRD patterns for the 15Y composite powders after annealing at successively higher temperatures for 2 hours. A restricted section of the patterns – between 25 and 55 degrees 2 theta – is shown for clarity. At each annealing temperature, all diffraction peaks can be indexed to the rhombohedral Bi_2Te_3 phase and the cubic Y_2O_3 phase, as labelled. The successive narrowing of the diffraction peaks at increasing temperatures is indicative of an increase in grain size and decrease in microstrain.

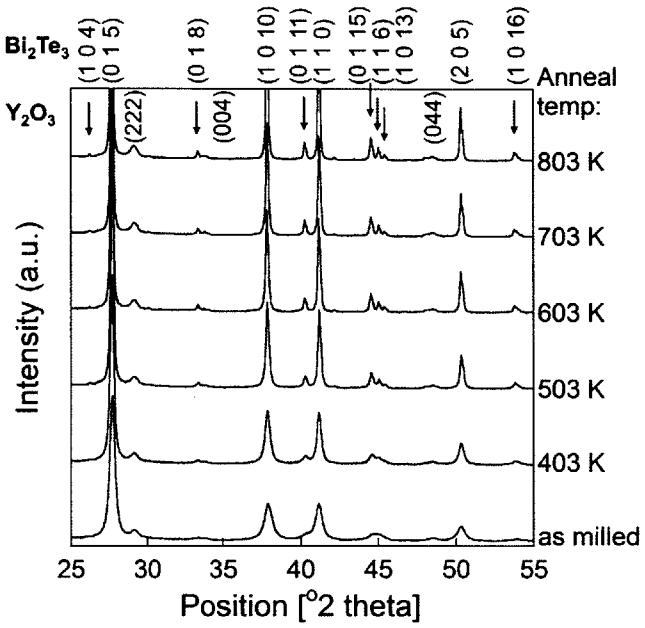

Fig. 6.3 A series of XRD patterns for the 15Y composite after annealing at temperatures between 403 and 803 K for 2 hours.

The evolution in stored enthalpy for the composite powders is shown in Fig. 6.4 alongside pure Bi_2Te_3. The pure compound shows a broad exotherm between about 120 and 380 °C. By comparison, the exotherm for the composite powders becomes increasingly narrower with increasing Y_2O_3 content. The composite exotherm onset remains at about the same temperature, but ends significantly earlier; by about 320 °C in the case of the 15Y sample. As a result, the peak heatflow becomes more intense and is shifted to lower annealing temperatures. The total release in stored enthalpy shown at the right of each curve – that is normalized per unit mass of Bi_2Te_3 – increases somewhat with increasing Y_2O_3 content.

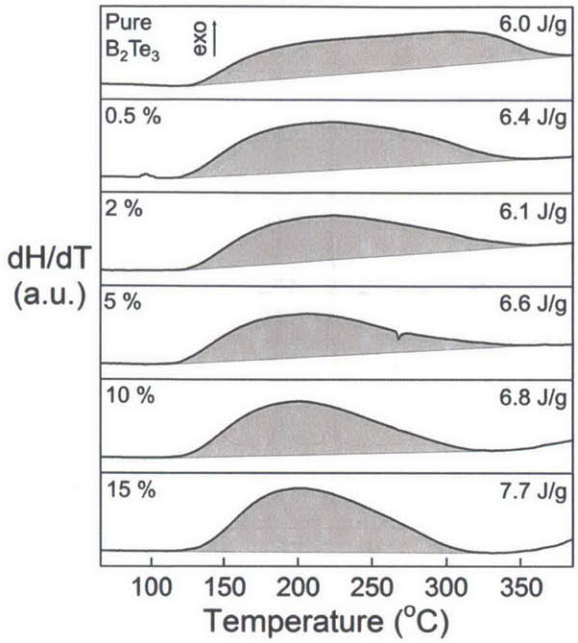

Fig. 6.4 A series of DSC scans showing the release of stored enthalpy for composite powders alongside the pure Bi_2Te_3 alloy, showing increasing heat release at low temperatures with increasing Y_2O_3 content.

The kinetics of grain size evolution for the 15Y composite and the pure Bi_2Te_3 is shown in Fig. 6.5, which plots the XRD-determined grain size as a function of annealing time at 300 °C. Pure Bi_2Te_3 shows continuous grain growth, evolving to a grain size of about 150 nm after 2 hours. The data-points have been fit with a grain growth exponent of 6.5, as determined in a previous study [ref]. By contrast, the composite evolves rapidly to a grain size of about 70 nm after 2 minutes, where it remains in a quasi-static state for prolonged annealing times.

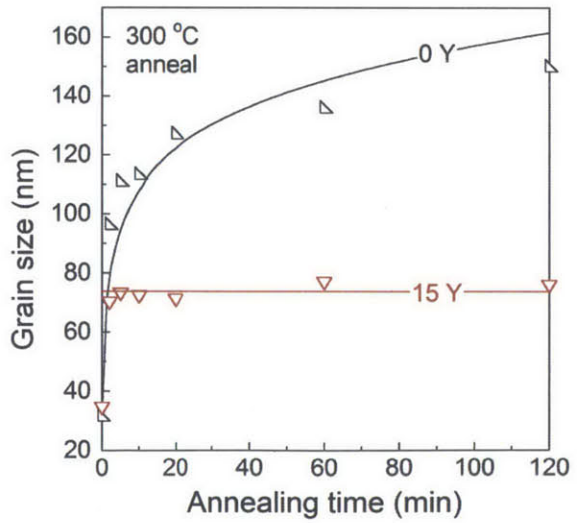

Fig. 6.5 The kinetics of grain growth for the pure Bi_2Te_3 and 15 wt. % Yttria powders during annealing at 300 °C as determined by XRD.

Fig. 6.6 shows the evolution in grain size (d), as a function of annealing temperature for the nano-composites and single phase Bi_2Te_3 alloy. Grain size was determined using XRD for most samples; however above 200 nm the grain size was measured using TEM and SEM. All data points were collected after a 2 hour long annealing treatment. A monotonic increase in grain size is observed for all materials; however two clear regions of behaviour emerge. In the low temperature region, T<250 °C, there is relatively little grain growth for the pure Bi_2Te_3 alloy, but apparently enhanced grain growth in the composite materials. For example at 180 °C the 15Y composite and pure Bi_2Te_3 alloy have d=52 and d=35 nm respectively, from a common starting grain size of 31 nm. This trend is reversed at temperatures above 250 °C where grain growth in the pure Bi_2Te_3 alloy becomes rampant relative to the composites; by 430 °C the 15Y and pure samples reach grain sizes of about 94 nm and 2.6 μm respectively. The grain size of the composite materials above 250 °C also clearly decreases with increasing Y_2O_3 content. For example, at the same temperature the 0.5Y sample reaches a gain size of about 196 nm, about double the size of the 15Y sample. At higher annealing temperatures, the grain size of the composites continues to increase mildly, however good thermal stability (<200 nm) is retained up to the melting point, while the pure Bi_2Te_3 material evolves to grain sizes on the order of 5-10 μm.

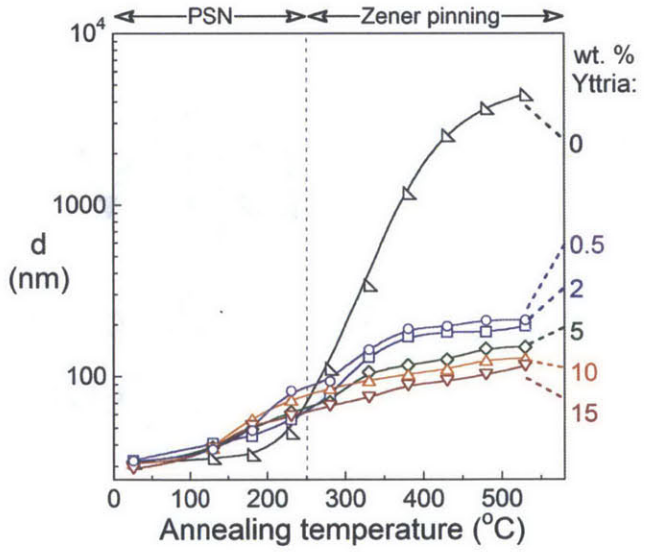

Fig. 6.6 The evolution of grain size with annealing temperature for the composite and pure powders after 2 hour anneals. At 250 °C there is a transition from grain size enlargement to grain size refinement for the composite materials.

Fig. 6.7 which shows TEM micrographs of (a) pure Bi_2Te_3, (b) 0.5 wt. % Y_2O_3 and (c) 5 wt. % Y_2O_3, taken after annealing at 430 °C for 2 hours. The grain sizes of the 0.5 and 5 wt. % Y_2O_3 samples – as measured stereologically – are 305 nm, and 224 nm respectively.

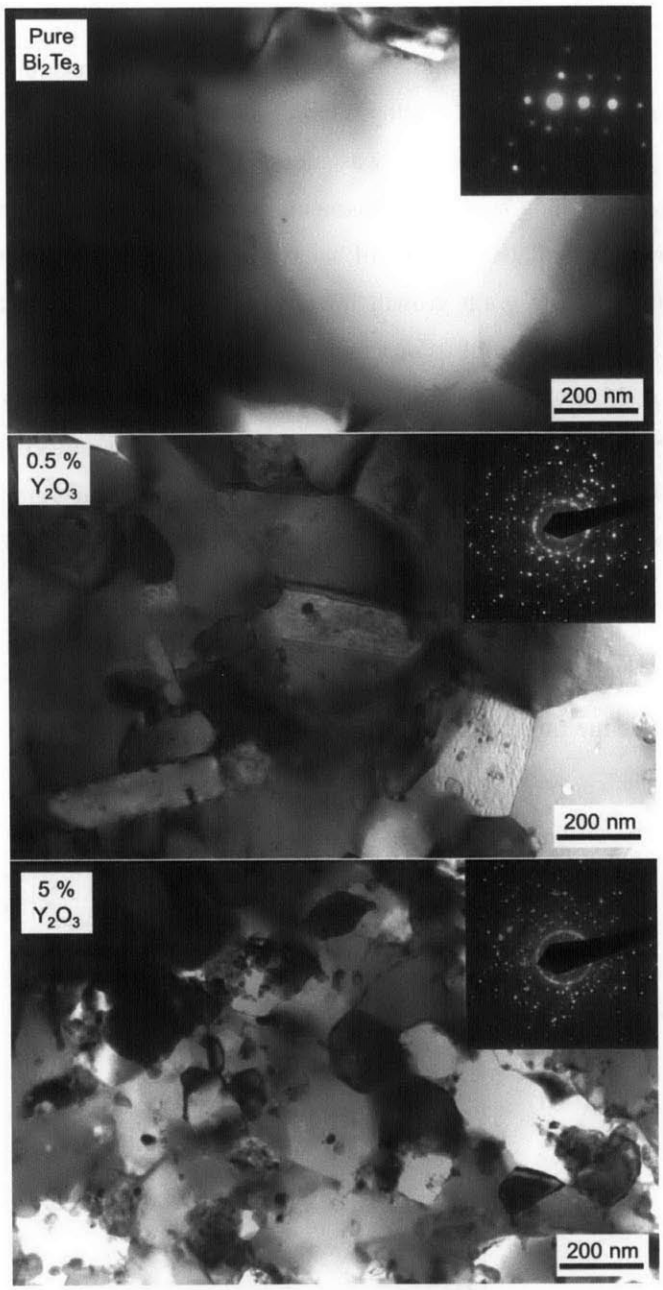

Fig. 6.7 TEM comparison of the composite and pure powders after annealing at 430 °C for 2 hours, showing finer grain size with increasing Y_2O_3 content.

Fig. 6.8 shows the evolution in microstrain and lattice parameters as determined via XRD. The microstrain (ε) – as depicted in the upper panel – shows a continual decrease with increasing temperature. Similarly to the grain growth trends in Fig. 6.6, the composite powders show enhanced recovery below 250 °C, and thus lower microstrain values, but above 250 °C the reverse is true. For example the 15Y and 0Y alloys have ε=0.06 and ε=0.20 at 180 °C respectively, but at 330 °C the same alloys have ε=0.02 and ε=0. At higher annealing temperatures still, the composites evolve towards a

microstrain that is fairly constant with temperature, but that increases with increasing Y_2O_3 content. The lattice parameter evolution (c/a) – as shown in the lower panel – is more complicated because it is not monotonic with annealing temperature. At temperatures below 250 °C, the c/a ratio increases from about 6.94 in the as-milled state towards the literature value c/a ratio (which has been measured to be 6.953 [133]). However, above 250 °C a divergence in the lattice parameter is observed, with the pure alloy showing a dramatic decrease in c/a ratio, which can be attributed to decomposition of the compound. Conversely, the composite samples show an increasing c/a ratio trend at higher temperatures.

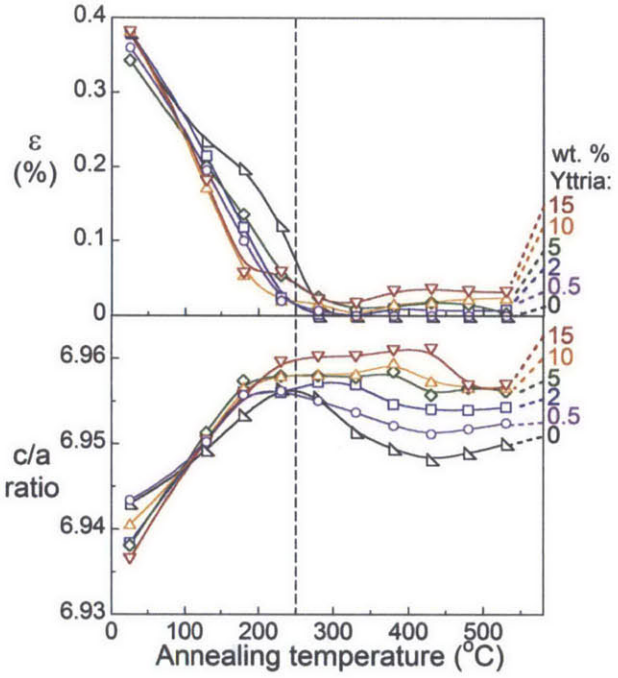

Fig. 6.8 The evolution of microstrain, (Upper panel) and lattice c/a ratio (lower panel) with annealing temperature for the composite and pure powders after 2 hour anneals.

6.4 Discussion

The most interesting effect of particle additions is the crossover seen in Fig. 6.6, where the particles not only slow grain growth at high temperatures, but apparently enhance grain growth at low annealing temperatures. The lower-temperature phenomenon is reminiscent of particle stimulated nucleation (PSN) of recrystallization, in which new grains are nucleated at the particles, leading to grain size reduction, although PSN is generally rarely observed around nano-scale <100 nm particles [217]. The higher-temperature phenomenon is reminiscent of thermally activated particle unpinning, as could be expected for very small pinning particles [213]. In the following we discuss the origins of

these phenomena and their expected prevalence with respect to particle size, volume fraction and annealing temperature.

6.4.1 Criterion for PSN

Evidence for particle stimulated nucleation (PSN) of recrystallization is given by the enhanced grain growth and recovery in the composite materials at low annealing temperatures. This behavior is further evidenced via the DSC signatures of Fig. 6.5, which show enhanced stored enthalpy release at low temperatures relative to the pure Bi_2Te_3 alloy, indicative of an accelerated grain growth and strain release process.

PSN in nanocomposite materials is generally unexpected due to the decreasing tendency for PSN as the size of the particle is reduced, as explored systematically during recrystallization of cold worked aluminum with oxide particles [216]; below a certain particle size, that is dependent on the level of deformation, PSN could not be observed. The driving force for PSN is enhanced plastic defect content produced around the undeformable particles, which provides a surplus driving force for recrystallization. In addition, the particle surface can in some cases provide a preferred heterogeneous nucleation site. The increase in stored enthalpy with increasing Y_2O_3 content, as shown in Fig. 6.4, indicates that the particles could have a greater degree of stored enthalpy in their vicinity.

In order to assess the likelihood of PSN, we first consider the various forces acting on a moving grain boundary during a recrystallization event in a two-phase material. In general, the driving pressure for growth of a recrystallization front (P_D) is due to the stored deformation enthalpy within the grain into which it is growing. Opposing this pressure are two boundary contributions which tend to shrink the recrystallizing nucleus. The first is a Zener pinning pressure (P_Z) from the second phase particles, and the second is the boundary curvature pressure (P_C). The net driving pressure on a migrating boundary is then [77]:

$$P = P_D - P_Z - P_C = E_{stored} - \frac{3f\gamma_b}{D} - \frac{4\gamma_b}{d} \qquad [6.1]$$

Where E_{stored} is the stored enthalpy with the grain interior, f is the volume fraction of particles, γ_b is the grain boundary energy, and D is the particle diameter. The simplest criterion for particle simulated nucleation considers the case where a nucleus of diameter d, is growing on a particle of diameter D, assuming that due to surface minimization, D=d [77], and in addition the Zener pinning pressure is neglected since it is usually small compared to the stored enthalpy in the grain. The condition for PSN is then:

$$D = \frac{4\gamma_b}{E_{stored}} \qquad [6.2]$$

However, as shown in Fig. 6.2, there is not a single particle size in this study, but rather a bimodal distribution of D. The effect of a bimodal particle size distribution is two-fold, since the largest particles provide favourable sites to nucleate recrystallized grains, while the smaller particles exert an increased pinning pressure. The recrystallization behaviour of a bimodal particle size distribution was studied in detail [218]. These two effects can be modelled by assuming that the driving pressure for recrystallization, P_D, is offset by the Zener pinning pressure, P_Z, where P_Z is assumed to be governed by the diameter of the smaller particles, and the critical nucleation size is for the larger particles. The critical particle size for growth of a nucleus is then given by [77]:

$$D = \frac{4\gamma_b}{P_D - P_Z} = \frac{4\gamma_b}{E_{stored} - 3f\gamma_b/D_{min}} \quad [6.3]$$

Where D_{min} is the diameter of the smaller pinning particles. Thus as the size of the finest particles decreases, the Zener pinning force increases, and the critical particle size for PSN increases.

In order to calculate the values of the critical pinning particle diameter in Eq. 6.3, we consider the grain boundary energy and driving force for recrystallization from the grain interior. The grain boundary energy for a random relaxed boundary in Bi_2Te_3 was recently measured via calorimetry to be γ_b=0.26 J/m^2 (chapter 4). The driving force for recrystallization can then be calculated by subtracting the grain boundary enthalpy from the total stored enthalpy [185]:

$$E_{stored} = E_{total} - \frac{2gV\gamma_b}{d} \quad [6.4]$$

where g is a geometric factor accounting for the grain shape, which is estimated to be 1.3 ± 0.2 [185], and V is the molar volume. The average stored enthalpy in the composite powders is 6.7 J/g, from which the stored enthalpy in the grain interior is calculated to be 2.8 J/g.

Fig. 6.9 shows a plot of D_{crit} as a function of volume fraction of pinning phase as given by Eq. 6.3. Several lines for the minimum particle diameters have been plotted, according to D_{min}=2, 5, 10, 20, and 50 nm. The lines intercept the y-axis at approximately 47 nm, which is the minimum particle size limit given by Eq. 6.2 in the limit of no Zener pinning pressure. Superimposed on the plot are the agglomerated and single crystal particles at a range of volume fractions used in this study that were observed in Fig. 6.2(a) and quantified in Fig. 6.2(b). The plot shows that the single crystal particles are unlikely to exhibit PSN, since they lie below the D_{min}=20 nm line, however the larger particles are. The plot also shows that as the size of the smallest particles is reduced, the Zenner pinning force for a given volume fraction increases, and therefore D_{crit} increases, indicating decreasing likelihood for PSN being observed.

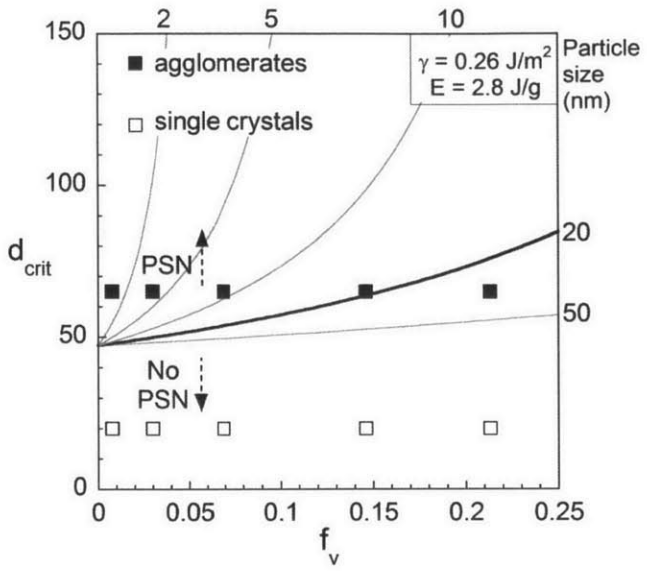

Fig. 6.9 The criterion for the critical maximum particle size to exhibit particle stimulated nucleation of recrystallization is plotted against volume fraction of second phase particles. For the smaller particle size fraction, a number of contours are plotted, for different particle sizes, where the 20 nm line is relevant to this study. The volume fractions and maximum particle diameters are plotted as squares, revealing that PSN is predicted to occur around the largest particles but not the smallest ones.

6.4.2 Particle accelerated vs inhibited growth

In the previous section it was shown that particle stimulated recrystallization of grains could result in acceleration of grain growth at low temperatures. At higher temperatures however, Fig. 6.6 shows that the grain size of the composites becomes finer. As a result there is a transition from a regime where particles accelerate grain growth, to a regime where particles retard grain growth. The transition is broadly due to a large decrease in the driving force for recrystallization, as the particle as recovery of the grain interiors occurs, and the stored enthalpy falls. If boundary mobility is assumed not to change, then transition from acceleration to retardation can be considered as the point where the driving force for particle stimulated nucleation of recrystallization in the particle containing alloy is equal to the driving force for grain growth in the pure alloy.

In order to estimate the driving force we must first consider the stored enthalpy within the grain interior, E_{stored}. In the previous section, we estimated E_{stored} in the as-milled state. However in this case we wish to consider the evolution of E_{stored} as a function of grain size during an annealing treatment. Experimentally, E_{stored} for the pure Bi_2Te_3 compound of initial grain size 23 nm was found to vary according to the equation (chapter 4):

$$E_{stored} = \frac{c}{d^n} \qquad [6.5]$$

where n was determined to be n=2.5±0.5, and c was a constant, found to be about c=5.6e-12 J/m^{3+n}. The stored enthalpy in the composite powders can be expected to follow a similar grain size trend to the pure material as shown by Fig. 6.10, which shows a plot of the microstrain as a function of inverse grain size for annealed composites, as well as pure Bi_2Te_3 powders. The composite microstrain shows a similar trend similar to pure Bi_2Te_3, which are both fit with a parabolic grain size trend with the same exponent of n=2.5, but different value of c, due to the different as-milled grain sizes in the two studies.

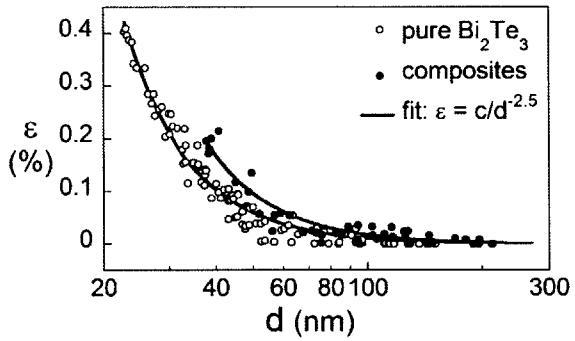

Fig. 6.10 The microstrain of the pure compound (data taken from chapter 4) and composite materials (this chapter) as a function of grain size – which is plotted on a logarithmic scale. Both sets of data are fitted with a parabolic relationship with an exponent of 2.5.

The fact that the composite powders follow a quantitatively similar trend in grain size dependence means that it is reasonable to assume E_{stored} will follow a similar trend. As a result, the driving force for recrystallization (in the composite) and grain growth (in the pure alloy) are given by the expressions:

$$P_{PSN} = \frac{c}{d^{2.5}} - \frac{3f\gamma_b}{D} - \frac{4\gamma_b}{d} \qquad [6.6]$$

$$P_{growth} = \frac{4\gamma_b}{d} \qquad [6.7]$$

Fig. 6.11 shows a plot of the driving forces for PSN and grain growth as a function of grain size. At the lower grain sizes the driving force for PSN is higher than that for grain growth, and at larger grain sizes vice versa. The crossover between the driving force curves is the point at which the driving force for grain growth becomes greater, corresponding to a transition from particle-accelerated growth to particle-inhibited growth. Several PSN driving force curves have been plotted, corresponding to the various volume fractions used in this study. As the volume fraction of particles is increased, the transition grain size is shifted to lower values. This makes intuitive sense; the pinning force of

particles tends to inhibit particle stimulated nucleation. Thus we can predict the following parameters to affect the transition grain size, d_{trans} :

Volume fraction – as f increases, d_{trans} decreases due to enhanced Zener pinning. This is also in accordance to what is observed in this study; a linear interpolation between the grain size data for the 0.5Y and 15Y samples yields a transition grain size of 90 nm and 61 nm respectively.

Particle size – D has a complicated effect on d_{trans}. For the smallest particles, an increase in D will increase d_{trans} due to a reduction in Zener pinning. However for the larger particles the reverse is true. We note that if the largest particle size is below the as-milled grain size, PSN is unlikely to occur.

Excess stored enthalpy – as the E_{stored} increases, d_{trans} increases due to a greater driving force for recrystallization. The E_{stored} is a parameter that is dependent on the material properties as well as the powder processing method. In chapter 3 it was shown that E_{stored} could be increased by employing lower energy milling conditions.

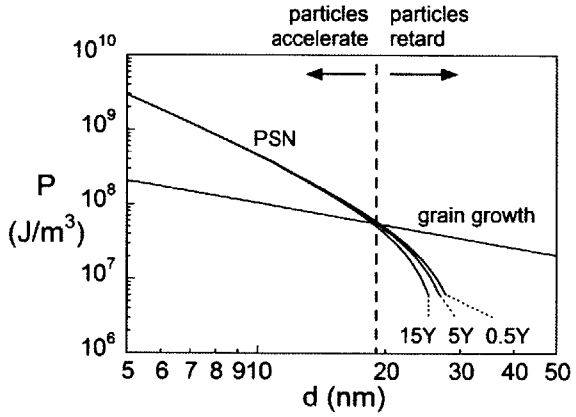

Fig. 6.11 The driving force for particle stimulated nucleation of recrystallization is higher at smaller grain sizes. At larger grain sizes however the driving force for grain growth becomes larger. This causes a transition from particle-accelerated growth to particle-inhibited growth.

6.5 Engineering Relevance

The enhanced thermal stability of the composite materials over the pure compound at elevated temperatures has some important implications for the engineering of thermoelectric materials. The very fine retained microstructures – which were shown to be typically in the range 100-200nm – are likely to impart enhanced thermoelectric properties, as well as enhanced densification characteristics. To investigate these properties, several compacts were made from the powders studied above. In what follows, we show that thermoelements made from the composite powders exhibit better consolidation characteristics – and enhanced thermoelectric properties as a result of the retained fine grain structure.

Next, more industrially relevant routes to composite synthesis were investigated. We demonstrate that in-situ production of Y_2O_3 nanoparticles is possible, which is a more cost effective technique. Finally, we make several recommendations for selection of inclusions in thermoelectric materials based on Bismuth Telluride.

6.5.1 Improved densification of composites

Oxide particle dispersed alloys are well known to endow high temperature creep resistance, since they tend to as defect trapping sites. To investigate the effect of Y_2O_3 nanoparticles additions, several compacts were made via the procedures outlined in chapter 5, at various chemistries between 0.5 and 10 wt. % Y_2O_3. The resulting porosity evolution is shown in Fig. 6.12. The porosity evolution, ΔP decreases dramatically with increasing Y_2O_3 content; at 500 °C a porosity increase of ΔP=0.3 is observed in the case of the pure compound, compared to an increase of between ΔP=0.07 and ΔP=-0.01 in the case of the 0.5Y and 10Y samples respectively. These results are backed up by macroscopic density measurements on the compacts after TMA, which are indicated as squares next to the curves.

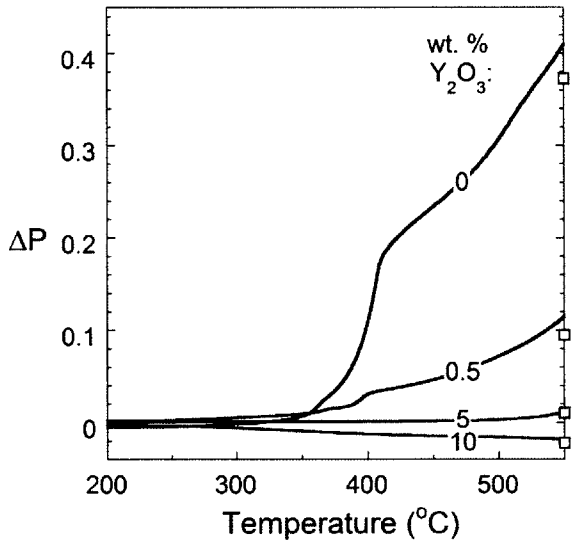

Fig. 6.12 Porosity evolution for composites in comparison to the pure compound. The additions of Y_2O_3 particles inhibit foaming, which is backed up by macroscopic density measurements indicated on the plot.

Micrographs of the compacts (taken using a JSM-6610 SEM in secondary electron imaging mode) are shown in Fig. 6.13, after heating to 550 °C in the TMA. The images show fracture surfaces of the compacts, which reveals the grain boundary and pore structure. The decrease in porosity with increasing Y_2O_3 content that is shown in Fig. 6.12 is reflected by the decrease in pore size and frequency in the micrographs, as well as a finer grain structure.

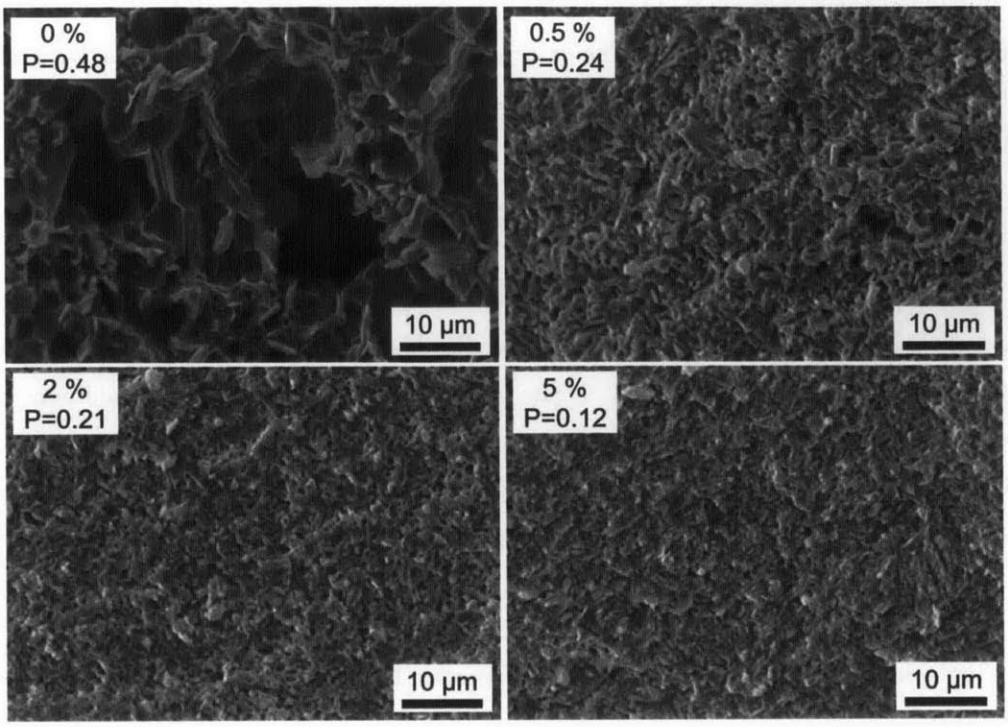

Fig. 6.13 Fracture surface of compacts taken after heating to 550 °C in the TMA. Both porosity and grain size are shown to decrease with increasing Y_2O_3 content.

The improved resistance to foaming displayed by the composites is encouraging from an engineering perspective, but cannot be explained readily without detailed study. A large number of chemical and structural defects are introduced into these materials as a result of deformation, and second phase particles are likely to interact with these in a number of ways. Nevertheless, the enhanced resistance to porosity formation is encouraging from an engineering perspective and offers opportunities for further study.

6.5.2 Enhanced thermoelectric properties

To compare the transport properties of the composites to the pure compound, thermoelements at the compositions 0Y, 5Y, and 15Y were fabricated. Firstly, powder compacts were made by cold pressing approximately 3 g of powders in a uniaxial die press in air. Powders were compressed in a tool steel die of 13 mm bore diameter, under a pressure of 465±20 MPa. The resultant compacts were then sintered under high purity flowing Argon for 3 hours at 400 °C. Following sintering, samples were polished and metallic contacts were sputtered into the sample for electrical contacts. From the disk shaped sample, cuboids of dimensions 2 x 2 x 3 mm were cut for measurement of thermal conductivity and seebeck coefficient, while an elongated sample of dimensions 1 x 2 x 12 mm was cut

for electrical resistivity. Transport measurements were made using a Physical Properties Measurement System (PPMS) from Quantum Design in the range 5-350 K.

The temperature dependence of the transport properties is shown in Fig. 6.14. The thermal conductivity (a) shows a decreasing trend with increasing Y_2O_3 content, with the 15Y sample showing between 25% and 50% the thermal conductivity of the pure compound depending on the temperature. All samples exhibit a negative seebeck coefficient (b), corresponding to n-type behaviour. Both composite materials show enhanced seebeck coefficient almost double that of the pure compound. The electrical resistivity (c) increases dramatically with increasing Y_2O_3 content; with a resistivity of 14, 44, and 162 μΩ-m for the 0, 5, and 15 Y samples at 300 K. Combining these parameters, via Eq. 1.1, ZT is enhanced relative to the pure compound in the 5Y sample, but diminished in the 15 Y sample, with maximum ZTs of 0.34 and 0.12 respectively.

The beneficial decrease in thermal and of the composite materials can be explained via two additional scattering mechanisms provided by the particles; firstly from the high area density of grain boundaries, and secondly the inclusion particles themselves. This result is at first unintuitive, since the Y_2O_3 phase has a bulk thermal conductivity of about 27 W/m-K at room temperature, which is more an order of magnitude greater than Bi_2Te_3. This benefit however is somewhat offset by the decrease in electrical resistivity, which can again be attributed to increased scattering sites. Electrical resistivity is also expected to be decreased by the presence of Y_2O_3 since it has a resistivity on the order of 10^8 Ω-m, which is almost 13 orders of magnitude greater than the Bi_2Te_3 phase. The increase in seebeck coefficient can be explained via an increase in structural defects which act as electron donor sites in Bi_2Te_3.

The overall increase in ZT for the 5Y sample over the pure compound – which is observed over the entire measured temperature range – is encouraging; and indicates that inert second phase doping could be an effective strategy for enhancing ZT in these materials. However, more detailed study is required in order to optimise the transport properties in this system. For example, we envisage that the peak ZT will occur at some intermediate concentration of Y_2O_3 particles between 0 and 5 wt. %. In addition, optimization would require – among other things – careful tuning of the particle size, host matrix composition, and sintering operation.

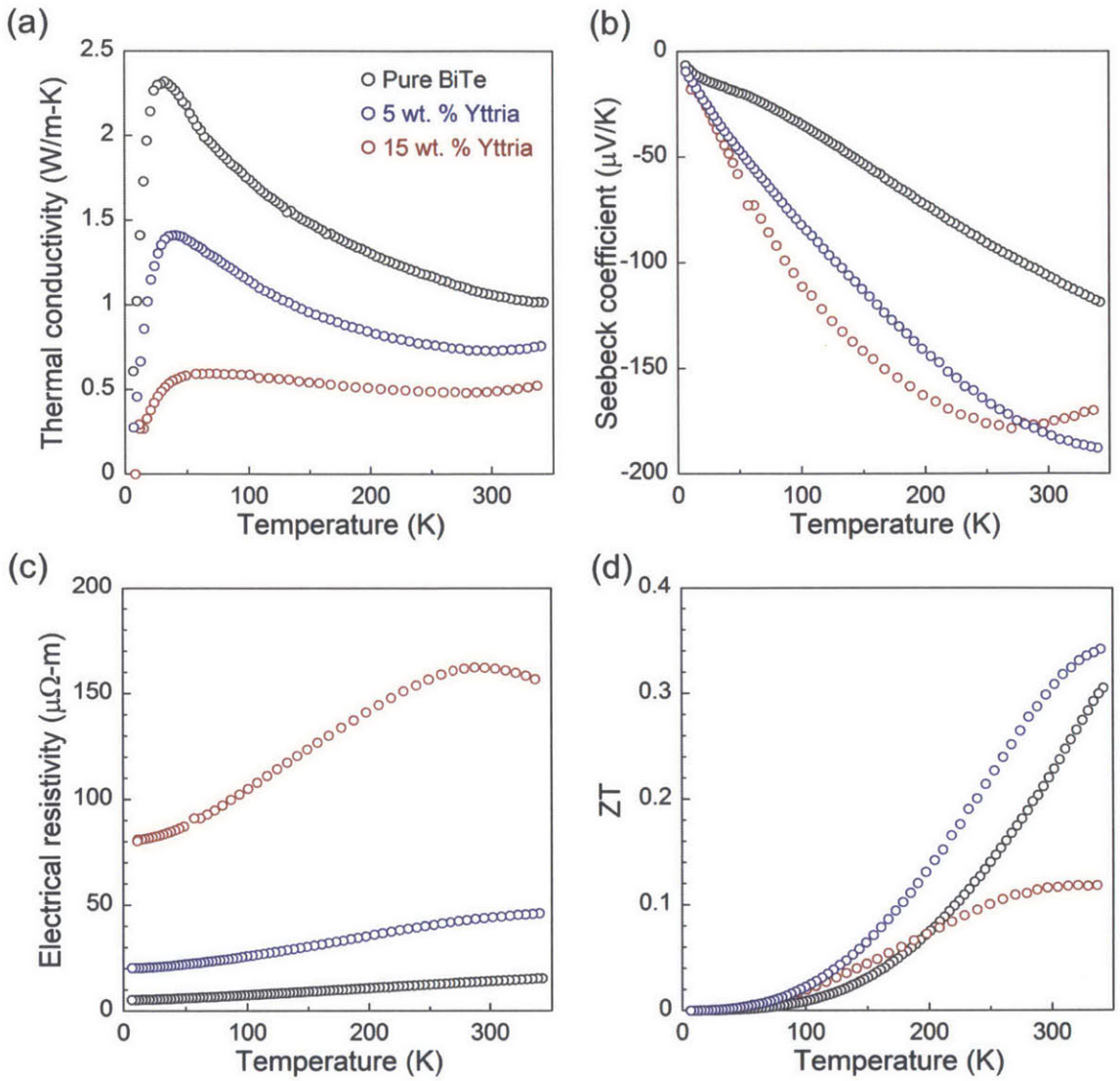

Fig. 6.14 Temperature dependence of: (a) thermal conductivity; (b) seebeck coefficient; (c) electrical resistivity; and (d) ZT of the pure compound as compared with the 5 and 15 wt. % composites

6.5.3 Alternative route to nanoparticle synthesis

Although the Y_2O_3 particles used in this study may provide enhanced properties, they are expensive to manufacture. Typically, synthesis requires many complicated and time intensive steps. For example, the sol-gel method involves: (i) mixing of chemical precursors, typically metal salts; (ii) precipitation to form a gel; (iii) rinsing gel to remove salts (iv) drying to obtain powders; (v) calcination of powders and; (vi) grinding or some other process operations [219]. These steps are prohibitively costly on an industrial scale, and commercial production of oxide dispersions in mechanically alloyed materials – such as Ni, Fe, and Al alloys – is typical achieved via in-situ oxidation [19].

To validate the concept of efficient production of oxide particles on an industrial scale, $Bi_2Te_3 - Y_2O_3$ composites were made via in-situ internal oxidation. Fig. 6.12 shows the structural evolution during this procedure for a 15Y sample. Firstly, the intermetallic Bi_2Te_3 was made by milling Bi + Te powders for 4 hours. Next, Y powders were added to the mixture, forming a composite of $Bi_2Te_{(1-x)}$ and YTe_2 after a further 4 hours of milling. Finally, a small amount of water was added to the vial, which results in the formation of Y_2O_3 particles in-situ, and a return to stoichiometry in the Bi_2Te_3 phase.

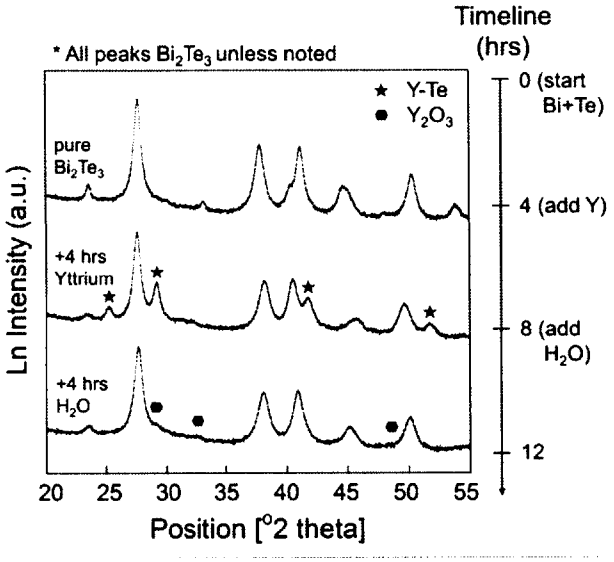

Fig. 6.15 The structural evolution during the formation of Yttria particles in-situ. After formation of the compound Bi_2Te_3 (4 hours) Yttrium metal is added which eventually forms the Y_2Te compound (8 hours). H_2O is then added, leading to the formation of Y_2O_3 particles (12 hours).

The stability of the 15Y powders is compared in Fig. 6.16 to material made via the in-situ particle formation technique at the same nominal chemistry. The grain size, microstrain and lattice c/a ratio is reported in the upper, middle and lower panels. The grain size of the in-situ material shows improved thermal stability as displayed by a grain size of 56 nm when annealed at 530 °C, compared to 115 nm for the conventional 15Y powders. However the lattice is highly distorted in the as-milled condition – as seen from the very low c/a ratio – which is likely due to remaining O and Y impurity atoms in the lattice. Upon annealing the lattice parameters return to the literature value of pure Bi_2Te_3.

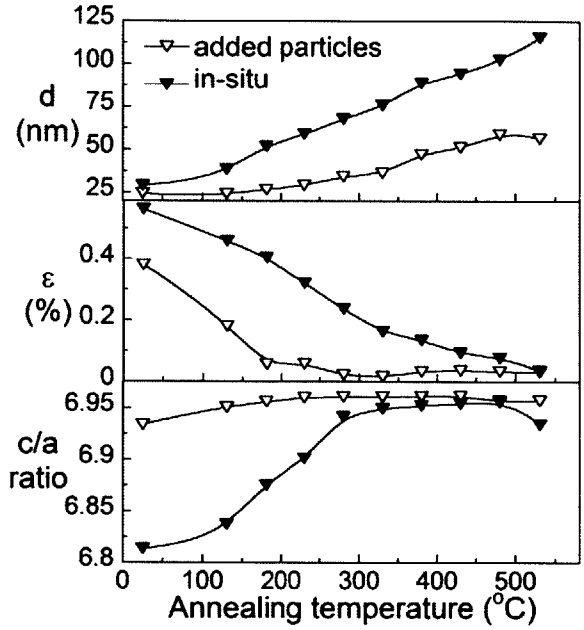

Fig. 6.16 The stability of in-situ oxidised composite is compared to the stability of the conventional composite, for a nominal Y_2O_3 content of 15 wt. %. The grain size (upper panel) microstrain (middle panel) and c/a ratio (lower panel) are shown.

The improved thermal stability of the in-situ alloy is probably due to the smaller particle size that results. The estimated mean grain size from XRD analysis was 3 nm, in comparison to 20 nm in the commercial nanoparticles. As discussed above, a smaller average particle size results in a larger Zener pinning force and thus a smaller equilibrium grain size for a given volume fraction and annealing treatment. This synthesis technique therefore offers a promising route for the fabrication of oxide dispersed nanocrystalline thermoelectric materials.

6.6 Conclusions

In this chapter the effect of a dispersion of Y_2O_3 particles on the microstructural stability of Bi_2Te_3 was investigated. The effect of particles compared to the pure compound was shown to transition from acceleration of grain growth, to inhibition of grain growth as the annealing temperature increased.

The enlarged grain size at low temperatures is explained on the basis of particle-stimulated nucleation of recrystallization occurring around the largest second phase particles. By considering the competing driving forces for boundary migration in the case of the pure compound and composite materials, the transition from particle-accelerated growth to particle-inhibited growth could be predicted, and as a result, the effect of various microstructural parameters on the transition grain size were examined.

As well as inhibiting grain growth, the particles also imparted higher compact densities and enhanced transport properties. While the induced porosity decreased monotonically with increasing particle volume fraction, ZT was enhanced at small volume fractions, but when the concentration was too high ZT was degraded due to the poor electrical conductivity of Y_2O_3. Thus ZT is envisaged to peak at some intermediate composition. Finally, in-situ formation was shown to be a viable route towards for preparation of Y_2O_3 nanoparticles, and could also impart improved thermal stability.

The findings of this work are promising from an engineering perspective; the enhanced stability and thermoelectric performance of the composite materials suggests that optimisation of the material system could be an advantageous route towards materials with higher ZT.

Chapter 7. Overview and future work

Thermoelectric materials are endowed with improved performance when processed into a nanocrystalline state. However nanomaterial instability presents intrinsic difficulties in both processing fine nanocrystalline structures and retaining them during device operation. This challenge has been addressed by studying the structural evolution during mechanical alloying and consolidation of a front-running low temperature thermoelectric material, Bismuth Telluride. During mechanical alloying, anomalous experimental trends were discovered due to the unique thermal and thermodynamic properties of the compound, offering new insights into processing science, and engineering guidance for microstructural optimization. During heat treatment, grain growth and porosity evolution were quantified, resulting in a thermal budget for the nanocrystalline compound. Based on this improved understanding in processing and stability, a strategy is developed for processing materials with enhanced thermal stability and transport properties using inert second phase particles.

7.1 Particle-wise combustion

In chapter 2, the mechanism of intermetallic formation from the elemental constituents was studied. The reaction was shown to occur more than an order of magnitude faster than conventional material systems, which was quantified on the scale of individual impacts as well as the entire powder charge. Based on these observations a new mechanochemical mechanism of mixing is proposed, which is based on a particle-wise combustion reaction that is ignited by via local melting of Bi. The mechanistic discovery in the Bi-Te system more broadly offers conclusive evidence of the operation of thermal effects during mechanical alloying, and gives greater insight to the mixing process, in which the common understanding is that mixing can only occur by diffusive means or via combustion on a global scale.

Future work: The new mechanistic insights developed here offer further opportunities to study the specifics of the mixing process, but also other mechanochemical processes. In the Bi-Te system, it is not at present clear what controls the quantity of intermetallic formation during a collision, and by extension whether there is a critical amount of deformation below which formation is prevented. Further study in these areas could give insight into this unique reaction. Furthermore, in other systems undergoing mechanochemical processes it would be interesting to understand what other elements could undergo local melting. A wider study of similarly volatile functional compounds based on Pb, Sn, Se, and Cd could offer further clarification on the role of molten phases during MA. Furthermore, the technique developed for the observation of critically loaded regions could be extended to other

material systems with experimentally accessible rate constants. For example, Co undergoes a mechanically induced HCP to FCC phase transformation.

7.2 Anomalous grain refinement trends

Grain refinement of the intermetallic during further mechanical treatment was studied in chapter 3. The process variable space was systematically explored, with respect to variations in the final grain size and other structural disorder. An unusual positive trend between the milling energy and the final grain size was found, which can be explained by the unusual properties of Bi_2Te_3. By considering the balance between recovery and refinement during milling, the anomalous impact energy dependence is explained on the basis of the adiabatic heat produced during a collision remaining localized in the region of deformation, promoting localized defect loss through annealing. This work provides engineering guidelines for optimizing the processing of these materials to achieve the finest grain sizes, which are attractive from the device-efficiency point of view.

Future work: Despite the advancements processing-structure understanding, the relationship between deformation rates and recovery is not an area that well understood; current steady-state grain size models assume that the overall strain rate is limited by material properties but the result of this study questions this assumption. Inclusion of such variability, which will come from a mechanistic understanding of the rate limiting processes, may lead to improved models for the nanostructure that evolves upon milling. Such models will also rely on high-quality data; systematic mechanical-milling studies of some more common low-melting point materials are needed.

7.3 Grain growth kinetics

In chapter 4, the grain growth kinetics of a fine-grained alloy was studied via a combination of experimental techniques. Two regimes of grain growth emerged: a low temperature regime where growth is dominated by recovery of defects and grain boundary relaxation, followed by a high temperature regime where growth is governed by conventional long range diffusive mechanisms. Using the quantified grain growth constants, a nanocrystalline thermal budget was developed in order to guide consolidation and device operation for these materials.

Future work: The abnormally high grain growth exponent that was measured is characteristic of studies on other nanocrystalline materials. This either indicates a non-linear relationship between the driving force and the rate of grain size increase, or some variability of driving force. At present, the rate of boundary migration in Bi_2Te_3 is poorly understood; a better understanding of the effect of driving force on the rate of migration in these materials is therefore needed.

7.4 Solid state foaming

In chapter 5, a further mechanism of nanocrystalline evolution is uncovered in Bi_2Te_3 – these materials are shown to undergo a spontaneous solid state foaming reaction, which is driven by compound phase separation. By studying the kinetics of porosity evolution, the primary driving force for porosity evolution is revealed. This mechanism is expected to account for many anomalously high reports of porosity evolution in other functional chalcogenide compounds, but until now has not been studied in detail. The understanding developed sets the time-temperature guidelines for use of these materials in high temperature environments, while the mechanistic understanding offers unique insight towards engineering materials more resistant to foaming.

Future work: Pore evolution seems to be common to many metal-chalcogenide functional compounds when processed far from equilibrium, therefore a systematic study across a range of these materials could be beneficial. Such a study could benefit not only the thermoelectric community but also researchers using these compounds for their ferroelectric, superconductive, and phase-change properties. Better insight to the mechanisms driving foaming could provide engineering guidelines for these materials, and strategies for its prevention.

7.5 Inert phase fillers

Based on the understanding developed in the previous sections, chapter 6 investigated a new strategy for enhanced thermal stability of nanocrystalline thermoelectric materials – by use of second phase particles. These additions are shown to impart improved resistance to both grain growth and foaming. The recovery and grain growth process is studied in detail at each stage of the annealing process. As a result, several recommendations can be made for the use of inert phase fillers in thermoelectric compounds.

Future work: Materials with inert phase fillers have demonstrated improved stability; however the system was not optimized with respect to volume fraction of second phase particles. Such an optimization is the current materials system would be a good starting point. Secondly, by incorporating second phase particles into ternary systems such as $(Bi\text{-}Sb)_2Te_3$ – with enhanced processing techniques such as Spark-Plasma-Sintering – it is possible that an impressive ZT could be demonstrated.

Appendix A: Chemical information on powders

Chemical analysis given by the supplier is given here. Starting powders of Tellurium and Bismuth were sourced from Alpha Aesar. The following information was provided in the certificate of analysis:

Tellurium powder, -200 mesh, 99.5% (metals basis)
Product No 10605
Lot No E21Y021

Se	68
Bi	19
Cu	18
Na	10
Pb	9.4
Ni	4.7
S	4
Fe	2.3
As	1.6
Si	<1
Al	0.5
Mg	<0.1

(all values in ppm)

Bismuth powder, -325 mesh, 99.5% (metals basis)
Product No 10111
Lot No B13Y041

Bi	99.99+ %
Ag	>10 ppm
Apparent density	3.53 g/cm^3

Sieve analysis:

+200 mesh	Trace
-200+325 mesh	1 %
-325 mesh	99%

Appendix B: Terminology and impact energy evaluation

Here we develop the methodology for evaluating the energy consumption of milling under different conditions. This allows comparative investigation in different milling devices. Under the assumption that each collision is purely inelastic, we define the impact energy (E) specific milling intensity (I_m) and specific milling dose (D_m) by:

$$E(J) = \frac{1}{2} m_b v_r^2 \qquad [B.1]$$

$$I_m(W/g) = NE/m_p = \frac{1}{2} N C_R v_r^2 \qquad [B.2]$$

$$D_m(J/g) = NEt/m_p = \frac{1}{2} N t C_R v_r^2 \qquad [B.3]$$

Where m_b is the ball mass, and v_r is the media velocity and can be obtained experimentally using the time lag method [30] or through the amount of heat released using the calorimetric method [130] under the assumption that most plastic work is dissipated as heat [174]. N is the number of hits per second, t is the milling time, m_p is the mass of the powder, and C_R is the charge ratio, i.e., ratio of total powder mass to total ball mass.

In the calorimetric method, the collision energy can be determined accurately from the temperature rise of the vial, so long as the vial is well insulated, and the milling time is small compared to the mean lifetime of temperature loss. This procedure was employed to calculate the energy consumption of the SPEX 8000 mill under a variety of milling frequencies. Although the dynamics of this mill have been measured quantitatively using a single milling ball by Delogu et al. [30], we used multiple milling balls in the present experiments. While this reduces processing time, it also necessitates independent verification of the energy consumption.

The rate of energy dissipation plotted as a function of milling frequency is plotted in Fig. B.1, where the corresponding rate of temperature rise shown in the upper left-hand corner of the figure. Total energy dissipation is calculated by estimating the vial heat capacity to be 419 J/K. This is then normalized per unit mass of milling media, to allow comparison between this study (approximately 50 g of balls) to the results of velocity measurements made on a single 12 g ball [30]. Good agreement is found between the two techniques, suggesting that collisions under many ball conditions are mainly inelastic. We note that in both cases the energy evolved per collision is linearly related to the square of the milling frequency. The result is that we can express the impact energy as:

$$E = D_0 N^2 m_p \qquad [B.4]$$

Where D_0 is a constant found to be 50 ± 2 μJ-s^2-g^{-1} under the conditions used. This allows the milling dose to be expressed in terms of the experimentally varied parameters:

$$D_m(J/g) = D_0 N^3 t \qquad [B.5]$$

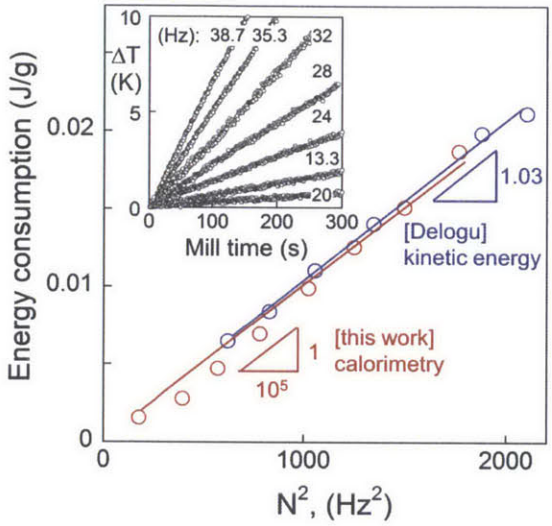

Fig. B.1 – Calibration of milling apparatus using the calorimetric method. The inset shows the temperature rise during a calorimetric run at various milling frequencies, from which the slope of the line gives the energy consumption. These values are plotted in the main figure as a function of milling frequency squared, and compared to Delogu et al. [220].

Appendix C: Comparison of grain size measurement techniques

We now compare the grain size estimations from x-ray diffraction (XRD) measurements with those from stereological transmission electron microscopy (TEM). For determination of grain size via XRD, a pseudo-Voight profile function was used, from which the crystallite size is estimated as

$$d = \left(\frac{180}{\pi}\right)\frac{\lambda}{(W_i - W_{std})^{0.5}} \qquad [C.1]$$

where λ is the wavelength of incident radiation, W_i is the order independent broadening parameter for the sample being measured, and W_{std} is the corresponding broadening of an instrumental standard with large grain size. For all samples in this study a NIST LaB_6 sample was used. The variance of the grain size measurement – which is a measure of the mean error – can be estimate from:

$$\sigma^2(d) = \left\{\left(\frac{180\lambda}{\pi}\right)^2 / 4(W_i - W_{std})^3\right\}[\sigma^2(W_i) + \sigma^2(W_{std})] \qquad [C.2]$$

where $\sigma^2(W_i)$ and $\sigma^2(W_{std})$ are the variance of the sample and instrumental standard respectively. At small grain sizes (d<100 nm) the sample broadening, W_i, is very large in comparison to W_{std}, and $\sigma^2(W_i)$ is small, therefore $\sigma^2(d)$ can be neglected. However as the grain size increases, $\sigma^2(d)$ becomes non-negligible for two reasons. Firstly W_i, becomes comparable to W_{std}, and secondly $\sigma^2(W_i)$ becomes large.

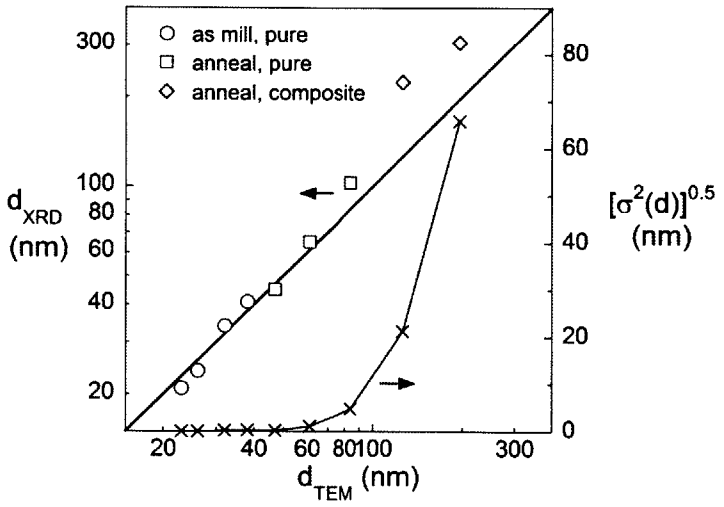

Fig. C.1 – Comparison of grain size measurements as measured via XRD and TEM. Good agreement is shown between the two techniques at small grain size, however above 100 nm XRD tends to underestimate grain size.

Fig. C.1 plots the grain size as determined by TEM, d_{TEM}, on the x-axis vs the grain size as determined via XRD, d_{XRD}, of the primary y-axis, for all samples in this study. The line $d_{TEM}=d_{XRD}$ is drawn for comparison. On the secondary y-axis, the square root of the variance is plotted, which is a measure of the mean error in d – as calculated using Eq. C.2. The plot reveals good agreement between XRD and TEM for samples below d=100 nm. However above this, XRD tends to overestimate d. This trend is mirrored by the monotonically increasing variance with increasing grain size, which increases from negligibly small values at the smallest grain sizes to approximately 65 nm at the largest grain size.

References

[1] Rowe DM, editor. Thermoelectrics and Its Energy Harvesting. Boca Raton, FL: CRC Press; 2012.

[2] Vining CB. Nat Mater 2009;8:83.

[3] Rowe D. General Principles and Basic Considerations, in: Rowe D (Ed.). Thermoelectr. Handb. CRC Press; 2005.

[4] Goldsmid HJ, Penn AW. Phys Lett A 1968;27:523.

[5] Meyers MA, Mishra A, Benson DJ. Prog Mater Sci 2006;51:427.

[6] Medlin DL, Snyder GJ. Curr Opin Colloid Interface Sci 2009;14:226.

[7] Joshi G, Lee H, Lan Y, Wang X, Zhu G, Wang D, Gould RW, Cuff DC, Tang MY, Dresselhaus MS, Chen G, Ren Z. Nano Lett 2008;8:4670.

[8] Li H, Tang X, Zhang Q, Uher C. Appl Phys Lett 2008;93:252109.

[9] Poudel B, Hao Q, Ma Y, Lan Y, Minnich A, Yu B, Yan X, Wang D, Muto A, Vashaee D, Chen X, Liu J, Dresselhaus MS, Chen G, Ren Z. Science 2008;320:634.

[10] Offergeld g, van Cakenberghe J. Nature 1959;184:185.

[11] Hashibon A, Elsässer C. Phys Rev B 2011;84:144117.

[12] Brebrick RF. J Phys Chem Solids 1969;30:719.

[13] Mallinson RB, Rayne JA, Ure RW. Phys Rev 1968;175:1049.

[14] Drabble JR, Goodman CHL. J Phys Chem Solids 1958;5:142.

[15] Jenkins JO, Rayne JA, Ure RW. Phys Rev B 1972;5:3171.

[16] Scherrer, Scherrer. Thermoelectric Properties of BismuthAntimony Telluride Solid Solutions, in: Rowe D (Ed.). Thermoelectr. Handb. CRC Press; 2005.

[17] Gleiter H. Prog Mater Sci 1989;33:223.

[18] Suryanarayana C. Prog Mater Sci 2001;46:1.

[19] Suryanarayana C. Mechanical Alloying and Milling. CRC Press; 2004.

[20] Benjamin JS. Metall Trans 1970;1:2943.

[21] Goldsmid HJ. Thermoelectric Refrigeration. New York: Plenum Press; 1964.

[22] Lund AC, Schuh CA. Phys Rev Lett 2003;91:235505.

[23] Bellon P, Averback RS. Phys Rev Lett 1995;74:1819.

[24] Koch CC. Mater Sci Forum 1992;88-90:243.

[25] Benjamin JS. Mater Sci Forum 1992;88-90:1.

[26] Takacs L. Prog Mater Sci 2002;47:355.

[27] Delogu F, Cocco G. Mater Sci Eng A 2005;402:208.

[28] Maurice DR, Courtney TH. Metall Trans A 1990;21:289.

[29] Delogu F. Scr Mater 2008;58:126.

[30] Delogu F, Schiffini L, Cocco G. Philos Mag A 2001;81:1917.

[31] Atzmon M. Phys Rev Lett 1990;64:487.

[32] Liu ZG, Guo JT, Ye LL, Li GS, Hu ZQ. Appl Phys Lett 1994;65:2666.

[33] Tschakarov CG, Gospodinov GG, Bontschev Z. J Solid State Chem 1982;41:244.

[34] Ma Y, Hao Q, Poudel B, Lan Y, Yu B, Wang D, Chen G, Ren Z. Nano Lett 2008;8:2580.

[35] Pierrat P, Dauscher A, Lenoir B, MARTIN-Lopez R, Scherrer H. J Mater Sci 1997;32:3653.

[36] Hasezaki K, Nishimura M, Umata M, Tsukuda H, Araoka M. Mechanical alloying of bite and bisbte thermoelectric-materials,

[37] Kim HC, Oh TS, Hyun D-B. J Phys Chem Solids 2000;61:743.

[38] Li Y, Jiang J, Xu G, Li W, Zhou L, Li Y, Cui P. J Alloys Compd 2009;480:954.

[39] Yu F, Zhang J, Yu D, He J, Liu Z, Xu B, Tian Y. J Appl Phys 2009;105:094303.

[40] Martin-Lopez R, Lenoir B, Dauscher A, Scherrer H, Scherrer S. Solid State Commun 1998;108:285.

[41] Medlin DL, Snyder GJ. JOM 2013;65:390.

[42] Medlin DL, Ramasse QM, Spataru CD, Yang NYC. J Appl Phys 2010;108:043517.

[43] Schultz JM, McHugh JP, Tiller WA. J Appl Phys 1962;33:2443.

[44] Hyun D-B, Hwang J-S, Shim J-D, Oh TS. J Mater Sci 2001;36:1285.

[45] Koch CC, Whittenberger JD. Intermetallics 1996;4:339.

[46] Lü L, Lai MO. Mechanical Alloying. Boston: Kluwer Academic Publishers; 1998.

[47] Zhang DL. Prog Mater Sci 2004;49:537.

[48] Murty BS, Ranganathan S. Int Mater Rev 1998;43:101.

[49] Oleszak D, Shingu PH. J Appl Phys 1996;79:2975.

[50] Fecht H, Hellstern E, Fu Z, Johnson W. Metall Mater Trans A 1990;21:2333.

[51] Mohamed FA. Acta Mater 2003;51:4107.

[52] Mohamed FA, Xun Y. Mater Sci Eng A 2003;354:133.

[53] Eckert J, Holzer JC, Krill CE, Johnson WL. J Mater Res 1992;7:1751.

[54] Hirth JP. Chapter 20 - Dislocations, in: Cahn RW, Haasen P (Eds.). Phys. Metall. Fourth Ed. Oxford: North-Holland; 1996.

[55] Hellstern E, Fecht HJ, Fu Z, Johnson WL. J Mater Res 1989;4:1292.

[56] Hong LB, Bansal C, Fultz B. Nanostructured Mater 1994;4:949.

[57] Yamada K, Koch CC. J Mater Res 1993;8:1317.

[58] Goodrich DM, Atzmon M. Mater Sci Forum 1996;225-227:223.

[59] Pochet P, Tominez E, Chaffron L, Martin G. Phys Rev B 1995;52:4006.

[60] Shen TD, Koch CC. Mater Sci Forum 1995;179-181:17.

[61] Xu J, He JH, Ma E. Metall Mater Trans A 1997;28:1569.

[62] Bonetti E, Campari EG, Pasquini L, Sampaolesi E, Valdrè G. Mater Sci Forum 1998;269-272:1005.

[63] Chan TE, Venkatasubramanian R, LeBeau JM, Thomas P, Stuart J, Koch CC. MRS Online Proc Libr 2013;1456:null.

[64] Witkin DB, Lavernia EJ. Prog Mater Sci 2006;51:1.

[65] Tian HH, Atzmon M. Acta Mater 1999;47:1255.

[66] (Sam)Froes FH, Suryanarayana C, Russell K, Li C-G. Mater Sci Eng A 1995;192-193:612.

[67] Delogu F, Cocco G. J Mater Sci 2007;42:4356.

[68] Delogu F, Cocco G. Mater Sci Eng A 2006;422:198.

[69] BÖRNER I, ECKERT J. Mater Sci Eng Struct Mater Prop Microstruct Process n.d.;226-28:541.

[70] Lan Y, Poudel B, Ma Y, Wang D, Dresselhaus MS, Chen G, Ren Z. Nano Lett 2009;9:1419.

[71] Ni JE, Case ED, Stewart R, Wu C-I, Hogan TP, Kanatzidis MG. J Electron Mater 2012;41:1153.

[72] Ni JE, Case ED, Schmidt RD, Wu C-I, Hogan TP, Trejo RM, Kirkham MJ, Lara-Curzio E, Kanatzidis MG. J Mater Sci 2013;48:6233.

[73] Lan Y, Minnich AJ, Chen G, Ren Z. Adv Funct Mater 2010;20:357.

[74] Bux SK, Fleurial J-P, Kaner RB. Chem Commun 2010;46:8311.

[75] Koch CC. J Mater Sci 2007;42:1403.

[76] Beck J, Alvarado M, Nemir D, Nowell M, Murr L, Prasad N. J Electron Mater 2012;41:1595.

[77] Humphreys FJ, Hatherly M. Recrystallization and Related Annealing Phenomena. Elsevier; 2004.

[78] Suryanarayana C. Int Mater Rev 1995;40:41.

[79] Murty BS, Datta MK, Pabi SK. Sadhana 2003;28:23.

[80] Andrievski RA. J Mater Sci 2014;49:1449.

[81] Birringer R. Mater Sci Eng A 1989;117:33.

[82] Chauhan M, Mohamed FA. Mater Sci Eng A 2006;427:7.

[83] G. Chojnowski RP. J Phys Chem C 2007;111:5599.

[84] Xiaoyan Song JZ. J Mater Res 2005;20:3054.

[85] J. Joardar SKP. Philos Mag Lett 2002;82:469.

[86] Zuo B, Sritharan T. Acta Mater 2005;53:1233.

[87] Kazuo Isonishi KO. 1992;28:3829.

[88] K. W Liu FM. Mater Sci Eng -Struct Mater Prop Microstruct Process - Mater Sci Eng -Struct Mater 2002;329:112.

[89] Natter H, Schmelzer M, Loffler M-S, Krill CE, Fitch A, Hempelmann R. J Phys Chem B 2000;104:2467.

[90] Estrin Y, Gottstein G, Shvindlerman L. Scr Mater 1999;41:385.

[91] Czubayko U, Sursaeva VG, Gottstein G, Shvindlerman LS. Acta Mater 1998;46:5863.

[92] Krill CE, Helfen L, Michels D, Natter H, Fitch A, Masson O, Birringer R. Phys Rev Lett 2001;86:842.

[93] Moelle CH, Fecht HJ. Nanostructured Mater 1995;6:421.

[94] Révész Á, Ungár T, Borbély A, Lendvai J. Nanostructured Mater 1996;7:779.

[95] Malow TR, Koch CC. Acta Mater 1997;45:2177.

[96] Ebrahimi F, Li H. Scr Mater 2006;55:263.

[97] Jang D, Atzmon M. J Appl Phys 2006;99:083504.

[98] Detor AJ, Schuh CA. J Mater Res 2007;22:3233.

[99] Hibbard GD, Erb U, Aust KT, Klement U, Palumbo G. Mater Sci Forum 2002;386-388:387.

[100] Tschope A, Birringer R, Gleiter H. J Appl Phys 1992;71:5391.

[101] Baker I. Intermetallics 2000;8:1183.

[102] Cahn R w., Takeyama M, Horton J a., Liu C t. J Mater Res 1991;6:57.

[103] Lee J-H, Grossman JC. Appl Phys Lett 2009;95:013106.

[104] Gibson LJ, Ashby MF. Cellular Solids: Structure and Properties. Cambridge University Press; 1999.

[105] Takashi Hamachiyo MA. J Electron Mater n.d.;38.

[106] Li J, Tan Q, Li J-F. J Alloys Compd 2013;551:143.

[107] Kumpeerapun T, Scherrer H, Khedari J, Hirunlabh J, Weber S, Dauscher A, Lenoir B, Zighmati B, M'Jahed H, Kosalathip V. Performance of Low-Cost Thermoelectric Modules Fabricated from Hot Pressing and Cold Pressing Materials, in: 25th Int. Conf. Thermoelectr. 2006 ICT 06. 2006.

[108] Takashiri M, Tanaka S, Hagino H, Miyazaki K. J Appl Phys 2012;112:084315.

[109] Takashiri M, Tanaka S, Miyazaki K. J Electron Mater n.d.:1.

[110] Lee H, Vashaee D, Wang DZ, Dresselhaus MS, Ren ZF, Chen G. J Appl Phys 2010;107:094308.

[111] Porter DA, Easterling KE. Phase Transformations in Metals and Alloys. CRC Press; 1992.

[112] Wynblatt P, Chatain D. Metall Mater Trans A 2006;37:2595.

[113] Weissmüller J. Nanostructured Mater 1993;3:261.

[114] Kirchheim R. Acta Mater 2002;50:413.

[115] Trelewicz J, Schuh C. Phys Rev B 2009;79.

[116] Bansal C, Gao ZQ, Fultz B. Nanostructured Mater 1995;5:327.

[117] Svechnikova TE, Konstantinov PP, Alekseeva GT. Inorg Mater 2000;36:556.

[118] Murdoch HA, Schuh CA. Acta Mater 2013;61:2121.

[119] Strudel J-L. Chapter 25 - Mechanical Properties of Multiphase Alloys, in: Cahn RW, Haasen P (Eds.). Phys. Metall. Fourth Ed. Oxford: North-Holland; 1996.

[120] Smith CS. Trans Met Soc AIME Vol 175 P 15-51 1948 1948;175:15.

[121] Gladman T. Proc R Soc Math Phys Eng Sci 1966;294:298.

[122] Trivedi PB, Patankar SN, Froes FH (Sam), Baburaj EG, Genç A, Ovecoglu L. Metall Mater Trans A 2002;33:2729.

[123] D Morris Mm. Mater Sci Eng -Struct Mater Prop Microstruct Process - Mater Sci Eng -Struct Mater 1991;134:1418.

[124] Yamasaki T, Zheng YJ, Ogino Y, Terasawa M, Mitamura T, Fukami T. Mater Sci Eng A 2003;350:168.

[125] S. Kamrani ZRH. Adv Compos Mater - Adv Compos Mater 2011;20:13.

[126] U. Martin MH. Adv Eng Mater 2004;6:515.

[127] Martin Heilmaier HS. Mater Sci Eng -Struct Mater Prop Microstruct Process - Mater Sci Eng -Struct Mater 2002;329:106.

[128] Ito M, Tada T, Hara S. J Alloys Compd 2006;408-412:363.

[129] Humphry-Baker SA, Schuh CA. Scr Mater 2011;65:516.

[130] Streletskii, A. N. Mech Alloy Struct Appl 2nd Int Conf Struct Appl Mech Alloy Mech Alloy Struct Appl 51-58 n.d.

[131] Cocco G, Delogu F, Schiffini L. J Mater Synth Process 2000;8:167.

[132] Wertheim GK, Butler MA, West KW, Buchanan DNE. Rev Sci Instrum 1974;45:1369.

[133] Nakajima S. J Phys Chem Solids 1963;24:479.

[134] Delogu F. Acta Mater 2008;56:2344.

[135] Oh TS, Choi JS, Hyun D-B. Scr Metall Mater 1995;32:595.

[136] Monagheddu M, Doppiu S, Deidda C, Cocco G. J Phys Appl Phys 2003;36:1917.

[137] Bakhshai A, Pragani R, Takacs L. Metall Mater Trans A 2002;33:3521.

[138] Fan GJ, Quan MX, Hu ZQ, Eckert J, Schultz L. Scr Mater 1999;41:1147.

[139] Ma E, Pagán J, Cranford G, Atzmon M. J Mater Res 1993;8:1836.

[140] Morgant G, Feutelais Y, Legendre B, Castanet R, Coulet A. Z Fuer Met Res Adv Tech 1990;81:44.

[141] Misra S, Bever MB. J Phys Chem Solids 1964;25:1233.

[142] Martin-Lopez R, Lenoir B, Dauscher A, Devaux X, Dümmler W, Scherrer H, Zandona M, Remy JF. Scr Mater 1997;37:219.

[143] Munir ZA, Anselmi-Tamburini U. Mater Sci Rep 1989;3:277.

[144] Joardar J, Pabi SK, Murty BS. Scr Mater 2004;50:1199.

[145] Lewandowski JJ, Greer AL. Nat Mater 2006;5:15.

[146] Delogu F, Deidda C, Mulas G, Schiffini L, Cocco G. J Mater Sci 2004;39:5121.

[147] Bhattacharya A., Arzt E. Scr Metall Mater 1992;27:749.

[148] Schwarz RB, Koch CC. Appl Phys Lett 1986;49:146.

[149] Shackelford JF, Alexander W. CRC Materials Science and Engineering Handbook. Boca Raton, FL: CRC Press; 2001.

[150] Humphry-Baker SA, Schuh CA. Acta Mater 2014.

[151] Hellstern E, Fecht HJ, Fu Z, Johnson WL. J Appl Phys 1989;65:305.

[152] Fecht H-J. Nanostructured Mater 1995;6:33.

[153] Brebrick RF. J Appl Crystallogr 1968;1:241.

[154] Magri P, Boulanger C, Lecuire J-M. J Mater Chem 1996;6:773.

[155] Navrátil J, Starý Z, Plecháček T. Mater Res Bull 1996;31:1559.

[156] Ionescu R, Jaklovszky J, Nistor N, Chiculita A. Phys Status Solidi A 1975;27:27.

[157] Nieh TG, Wadsworth J. Scr Metall Mater 1991;25:955.

[158] Koch CC, Youssef KM, Scattergood RO. Mater Sci Forum 2008;579:15.

[159] Estrin Y, Tóth LS, Molinari A, Bréchet Y. Acta Mater 1998;46:5509.

[160] Starink MJ, Qiao XG, Zhang J, Gao N. Acta Mater 2009;57:5796.

[161] Tóth LS, Estrin Y, Lapovok R, Gu C. Acta Mater 2010;58:1782.

[162] Petryk H, Stupkiewicz S. Mater Sci Eng A 2007;444:214.

[163] Bouaziz O, Estrin Y, Bréchet Y, Embury JD. Scr Mater 2010;63:477.

[164] Brown AM, Ashby MF. Acta Metall 1980;28:1085.

[165] Kuhrt, Schröpf H, Schultz L, Arzt E. Mech Alloy Struct Appl 2nd Int Conf Struct Appl Mech Alloy Mech Alloy Struct Appl 269-273 1993.

[166] Löffler J, Weissmüller J. Phys Rev B 1995;52:7076.

[167] Dabhade VV, Rama Mohan TR, Ramakrishnan P. Mater Sci Eng A 2007;452-453:386.

[168] Rupert TJ, Trelewicz JR, Schuh CA. J Mater Res 2012;27:1285.

[169] Koch CC. Nanostructured Mater 1993;2:109.

[170] Delogu F, Cocco G. J Alloys Compd 2006;420:246.

[171] Boytsov O, Ustinov AI, Gaffet E, Bernard F. J Alloys Compd 2007;432:103.

[172] Vives S, Gaffet E, Meunier C. Mater Sci Eng A 2004;366:229.

[173] Hellstern E, Fecht HJ, Garland C, Johnson WL, Keck WM. MRS Online Proc Libr 1988;132:null.

[174] Taylor GI, Quinney H. Proc R Soc Lond Ser Contain Pap Math Phys Character 1934;143:307.

[175] Eckert J. Nanostructured Mater 1995;6:413.

[176] Carslaw HS. Conduction of Heat in Solids, 2nd ed. Oxford [Oxfordshire] : New York: Clarendon Press ; Oxford University Press; 1986.

[177] Terada Y, Ohkubo K, Nakagawa K, Mohri T, Suzuki T. Intermetallics 1995;3:347.

[178] Desai PD, Payne JE, Gilp BF, Dudley RD, editors. Properties of Intermetallic Alloys. West Lafayette, Ind: Metals Information Analysis Center, Center for Information and Numerical Data Analysis and Synthesis, Purdue University; 1994.

[179] Maex K, Rossum M van, Engineers I of E. Properties of Metal Silicides. INSPEC; 1995.

[180] Westbrook JH, Fleischer RL, editors. Magnetic, Electrical and Optical Properties, and Applications of Intermetallic Compounds. Chichester, England ; New York: Wiley; 2000.

[181] Asm, 0871703815, 978-0871703811. ASM Handbook: Volume 3: Alloy Phase Diagrams (Asm Handbook) (Asm Handbook), 10 edition. ASM International; 1992.

[182] Pierson HO. 1 - Introduction, in: Pierson HO (Ed.). Handb. Refract. Carbides Nitrides. Westwood, NJ: William Andrew Publishing; 1996.

[183] Patnaik P. Handbook of Inorganic Chemicals. New York: McGraw-Hill; 2003.

[184] Weissmüller J. Thermodynamics of Nanocrystalline Solids, in: Knauth P, Schoonman J (Eds.). Nanocrystalline Met. Oxides. Springer US; 2002.

[185] Chen LC, Spaepen F. J Appl Phys 1991;69:679.

[186] Gleiter H. Phys Status Solidi B 1992;172:41.

[187] McElroy RJ, Szkopiak ZC. Int Metall Rev 1972;17:175.

[188] Guan Z-P, Dunand DC. Mater Sci Eng A 2013;565:321.

[189] Peranio N, Eibl O. Phys Status Solidi A 2009;206:42.

[190] Zhou F, Lee J, Lavernia EJ. Scr Mater 2001;44:2013.

[191] Valiev RZ, Kozlov EV, Ivanov YF, Lian J, Nazarov AA, Baudelet B. Acta Metall Mater 1994;42:2467.

[192] Tellkamp VL, Dallek S, Cheng D, Lavernia EJ. J Mater Res 2001;16:938.

[193] Dutt MB, Sharma BL. 3 Diffusion in Compound Semiconductors - References, in: Beke DL (Ed.). Diffus. Semicond. Springer Berlin Heidelberg; 1998.

[194] Burke J, Turnbull D. Prog Met Phys 1952;3:220.

[195] Riga AT, Neag CM. Materials Characterization by Thermomechanical Analysis. ASTM International; 1991.

[196] Barnes JO, Rayne JA, Ure Jr RW. Phys Lett A 1974;46:317.

[197] Satterthwaite CB, Ure RW. Phys Rev 1957;108:1164.

[198] Kim SS, Yamamoto S, Aizawa T. J Alloys Compd 2004;375:107.

[199] Hwang C-W, Hyun D-B, Ha H-P, Oh TS. J Mater Sci 2001;36:3291.

[200] Chizhevskaya S, Shelimova L, Zemskov V, Kosyakov V, Malakhov D. Inorg Mater 1994;30:1.

[201] Thermodynamic Properties of Elements, S7 to Ti, in: Pure Subst. Part 1 Elem. Compd. AgBr Ba3N2. Springer Berlin Heidelberg; 1999.

[202] 1972 -June 1. American Institute of Physics Handbook, Third Edition. New York: Mcgraw-Hill; 1972.

[203] Brebrick RF. J Phys Chem 1968;72:1032.

[204] Olsen DA, Moravec RW, Osteraas AJ. J Phys Chem 1967;71:4464.

[205] Nguyen Thanh Nghi ALU. Cryst Res Technol - Cryst Res Tech 1986;21:367.

[206] Butt H-J, Graf K, Kappl M. Liquid Surfaces, in: Phys. Chem. Interfaces. Wiley-VCH Verlag GmbH & Co. KGaA; 2003.

[207] Ashby MF, Evans AG, Fleck NA, Gibson LJ, Hutchinson JW, Wadley HNG. Chapter 2 - Making Metal Foams, in: Ashby MF, Evans AG, Fleck NA, Gibson LJ, Hutchinson JW, Wadley HNG (Eds.). Met. Foams. Burlington: Butterworth-Heinemann; 2000.

[208] VanLeeuwen BK, Darling KA, Koch CC, Scattergood RO. Mater Sci Eng A 2011;528:2192.

[209] Argon AS. Chapter 22 - Mechanical Properties of Single-Phase Crystalline Media: Deformation in the Presence of Diffusion, in: Cahn RW, Haasen P (Eds.). Phys. Metall. Fourth Ed. Oxford: North-Holland; 1996.

[210] Zhen-Hua Ge B-PZ. J Mater Res 2011;26:2711.

[211] Manohar P, Ferry M, Chandra T. ISIJ Int 1998:913.

[212] Hillert M. Acta Metall 1988;36:3177.

[213] Gore MJ, Grujicic M, Olson GB, Cohen M. Acta Metall 1989;37:2849.

[214] M ASHBY RG. Acta Metall 1968;16:1081.

[215] Hillert M. Acta Metall 1965;13:227.

[216] Humphreys FJ. Acta Metall 1977;25:1323.

[217] Humphreys FJ. Met Sci 1979;13:136.

[218] Nes E. Acta Metall 1976;24:391.

[219] Livage J, Henry M, Sanchez C. Prog Solid State Chem 1988;18:259.

[220] Delogu F, Mulas G, Schiffini L, Cocco G. Mater Sci Eng A 2004;382:280.